Vol. 14 • No. 1 • April 2020

ISSN: 0976 - 1330

Journal of GEOMATICS

INDIAN SOCIETY OF GEOMATICS

Journal of Geomatics

(A publication of the Indian Society of Geomatics)

Editorial Board

Advisory Board

Indian Society of Geomatics
Executive Council 2020-2023

Secretary: (address for correspondence)
6202, Space Applications Centre, ISRO, Bopal Campus, Ahmedabad-380058, India
Email: secretary@isgindia.org; sasharma@sac.isro.gov.in

Journal of Geomatics
(A Publication of the Indian Society of Geomatics)
Vol. 14. No. 1 Research articles April 2020

Journal of Geomatics Vol. 14, No. 1, April 2020

Performance of CORS techniques (VRS and FKP) method in Istanbul Metropolitan City

Atınç Pırtı and Ramazan Gürsel HOŞBAŞ
Yildiz Technical University, Department of Surveying Engineering, Davutpasa, 34220 Esenler, Istanbul, Turkey
Email: atinc@yildiz.edu.tr

(Received: July 27, 2019; in final form: Nov 20, 2019)

Abstract: Continuously Operating Reference Stations (CORS) surveys have been utilized for a variety of different surveying applications. A case study was performed to investigate the use of the CORS surveys. Surveys were conducted in the city of İstanbul (Yıldız Technical University Davutpaşa Campus), Turkey on 30 April and 1, 2, 3 May 2011. One hundred and eight points were selected in the project area. The analyses were made in fifth steps. In fifth steps, the CORS (Virtual Reference Station (VRS) – Flächen- Korrektur-Parameter Spatial Correction Parameter (FKP)) results gained on different days were compared with each other. The results showed differences from 0 to ±0.20 metres between the coordinates obtained from the VRS-FKP techniques in the project area. The results from all the tests have proved that this modern technique is very suitable for data acquisition and is efficient and economical. It concludes that the CORS technique competes well with the traditional surveys techniques in terms of accuracy in project area.

Keywords: CORS, Accuracy, Virtual Reference Station, Spatial Correction Parameter

1. Introduction

Relative positioning provides a higher accuracy than that of autonomous positioning. Depending on whether the pseudo range or carrier-phase measurements are used in relative positioning, an accuracy level of a few meters to millimetres, respectively, can be obtained. This is mainly because the measurements of two (or more) receivers simultaneously tracking a particular satellite contain more or less the same errors and biases. Therefore, if we take the difference between the measurements of the two receivers, common errors will be removed and those that are spatially correlated will be reduced depending on the distance between the reference receiver and the rover (Baseline). In surveying tasks where the high accuracy is required, a relative kinematic solution using GPS/GLONASS phase observations can be used to quickly obtain the data. In relative surveys, the accuracy of the position degrades as the rover moves away from the base station (Lachapelle et al., 2001; Vollath et al., 2002; Wolf and Ghilani, 2008; Bock et al., 2002; Landau et al., 2003; Vollath et al., 2000; Vollath, et al., 2001; Wübbena et al., 2001; Talbot et al., 2002; Dai et al., 2003; Bae et al., 2015; Bisnath et al, 2013; Hoffmann et al, 2008; Alves et al., 2011; Ma et al., 2011; Berber and Arslan, 2013).

This paper investigates the accuracy capabilities and performance of the CORS (VRS/FKP) for the Istanbul Metropolitan area. In this article, the feasibility and reproducibility of the CORS for different satellite configurations were investigated in the applications. The results obtained by CORS on three different days were compared with each other.

2. Materials and Methods

2.1. Virtual Reference Station (VRS)

VRS is a Trimble developed system to support high accuracy RTK GNSS positioning. The VRS algorithms simulate the existence of a reference station located at the rover's approximate location. This approach requires: (i) the availability of multiple Reference Stations in the rover's neighbourhood; (ii) to know the approximate location of each rover throughout the entire operation; and (iii) to know the exact coordinates of the Reference Station locations. As a result, the VRS approach requires the establishment of a bi-directional data link between the VRS module and each client rover. It is through this connection that the rover conveys its whereabouts and the system communicates the customized pseudo range corrections. These customized correction messages are generated as if by a reference station located at the rover's approximate location. Thus, the position-dependent errors are better modelled than when using a distant reference station. Through a two-way communication, the central processing server will get the rovers navigation solution in the NMEA format (National Marine Electronics Association). Once it receives this location, it selects the nearest three reference stations to calculate the corrections for the rover. It creates a VRS in close proximity to the rover. Thus in the end the rover will receive a single baseline solution with a much shorter baseline length. Nowadays, this is the most widely used method for CORS positioning because there is no need to upgrade the user equipment software. But this method does have the drawback that there is no information about the quality of the interpolation process and thus on the quality of the VRS reference observations. VRS locates a virtual reference station as close as the rover receiver which requests correction calculated with integer ambiguity fixed by using all the CORS stations data in the network. Then the corrections are sent via the VRS to the user. When the rover moves too far away from the calculated VRS, the rover is forced to reinitialize its position fix and a new VRS needs to be calculated, therefore the efficiency of this approach is reduced (Landau et al., 2003; Vollath et al., 2000; Dai et al., 2003; Edwards et al., 2010; Ma et al., 2011; Berber and Arslan, 2013).

2.2. Spatial Correction Parameter (FKP)

The Flächen- Korrektur-Parameter (FKP) technique is another way that delivers the information from a base station network to the rover. No precise knowledge of the rover's position is required for providing the correct

information. The corrections are deployed as gradients to be used for interpolating to the rover's actual position. FKP is the preferred method of Geo++ for disseminating network RTK information. In principle, any format capable of transporting base station raw observations can be used together with a message to transport the FKP coefficients. Geo++ combines the FKP information with RTCM version 2.3, RTCM2021 messages which has been adopted as the standard for SAPOS. For the FKP information, no standard has been adopted yet but some users and providers argue that there is a standard because the information is being transmitted in an RTCM59 message. The layout of the message is described in RTCM Message Type 59-FKP for transmission of FKP. The FKP approach involves simply a one-way communication from the server to the rover. FKP was introduced in Germany as its standard technique to provide network information to an RTK rover. FKP increases the RTK performance by using area correction parameters information from reference station networks. FKP supplies information about the distant dependent error components. The parameters are given in the RTCM 2.3 message 59 (Landau et al., 2003; Bock et al., 2002; Edwards et al., 2010; Ma et al., 2011; Berber and Arslan, 2013).

3. Results

To test the performance of the CORS, two different test configurations (VRS/FKP technique) were considered within the boundaries of the Istanbul City (Davutpasa Campus of Yildiz Technical University). The stations of the ISKI CORS (ISKI is short for İstanbul Metropolitan City Irrigation and Drainage Administration, CORS) were used in this study, which is depicted in figure 1 (Gumus, 2016). This network consists of eight stations distributed in Istanbul city boundary. The network can also provide VRS, FKP and Master Auxiliary Concept (MAC) corrections. These corrections are calculated by Topcon Geo+ Software. First of all ISKI-CORS (VRS-FKP) measurements were performed on consecutive days and at different times of the day (VRS1 (30 April 2011, 9:00 – 11:20 h local time (LT)), FKP1 (30 April 2011, 12:00 – 14:20 h local time (LT))), (VRS (1 May 2011, 10:00 – 12:20 h local time (LT)), FKP2 (1 May 2011, 13:00 – 15:20 h local time (LT))), (VRS3 (2 May 2011, 11:00 – 13:20 h local time (LT)), FKP3 (3 May 2011, 14:00 – 16:20 h local time (LT))) with changed satellite configurations to ensure the independence of the results. ISKI-CORS solution for this study used in surveying is 5s at each point with 1s registration interval with a cut-off elevation mask angle of 10 degrees.

In all cases, all CORS measurements are made using Topcon HiperPro dual frequency GNSS receivers (Horizontal Accuracy: 10mm+1.0ppm; Vertical Accuracy: 15mm+1.0ppm) with standard hardware and software and observations from 6-12 (GPS / GLONASS) satellites and observations of 1.2-4.8 PDOP values during all sessions (Figure 2). Thus, all these 108 object points are positioned with VRS-FKP techniques in ITRF 2000 datum (ITRF (International Terrestrial Reference Frame) which is a physical realization of ITRS (International Terrestrial Reference System)).

To evaluate the ISKI-CORS repeatability in Istanbul, six independent CORS surveys ((VRS1 (30 April 2011, 9:00 – 11:20 h local time (LT)), FKP1 (30 April 2011, 12:00 – 14:20 h local time (LT))), (VRS (1 May 2011, 10:00 – 12:20 h local time (LT)), FKP2 (1 May 2011, 13:00 – 15:20 h local time (LT))), (VRS3 (2 May 2011, 11:00 – 13:20 h local time (LT)), FKP3 (3 May 2011, 14:00 – 16:20 h local time (LT))) solutions) by using ISKI CORS reference points were conducted. A total of 648 point observations for the 108 test points were obtained. In the first analysis step, the differences of the coordinates of the 108 test points obtained from VRS1, VRS2 and VRS3 were calculated, such as VRS1 - VRS2, VRS1 - VRS3 and VRS2 - VRS3, respectively. Figure 3 shows the coordinate differences, mean and standard deviation values for 108 points. The standard deviation values between ±0.03 and ±0.05 m; the mean values (abs (ΔX), abs (ΔY), and abs (ΔH)) between 0.03 m and 0.04 m are obtained for the X and Y coordinate components: The coordinate differences in the H direction are about 0.02-0.03 m; the standard deviation value is ±0.028 m and the mean value is 0.021 m. The VRS results show that the horizontal coordinate differences are between ±0.01 m and ±0.15 m. The differences in height coordinates at some points are about ±0.18 metres (Figure 3).

3.1 Horizontal and Vertical Accuracy of FKP Technique

In the second phase, the coordinate differences of 108 points obtained from FKP1 (30 April 2011, 12:00 – 14:20 h local time (LT)), FKP2 (1 May 2011, 13:00 – 15:20 h local time (LT)) and FKP3 (3 May 2011, 14:00 – 16:20 h local time (LT)), such as FKP1 - FKP2, FKP1 - FKP3 and FKP2 - FKP3 were calculated respectively. In this study, CORS surveys are affected by an obstacle (i.e. the nearby building north-south of the rover antenna, approximately obstructed 50% of the sky, see figure 2). Figure 4 presents the differences and their mean and standard deviation values for the 108 points. When the coordinate differences in Fig. 4 are examined, it is seen that the standard deviation values are between ±0.03 m and ±0.05 m, the mean values are between ±0.03 m and ±0.10 m for the X and Y coordinate components. The mean difference values in vertical (H) direction are between ±0.02 and ±0.03 m, the standard deviation values are between ±0.02 and ±0.03 m. Analysis of the FKP results show that the horizontal coordinate differences are between ±0.01 m and ±0.20 m. The maximum differences in height coordinates are about ±0.15 metres (Figure 4). Analysis of the first, second and third days of FKP measurements in the project area shows that the differences in horizontal and vertical coordinates are generally approximately between ±0.02 m and ±0.20 m (Figure 4).

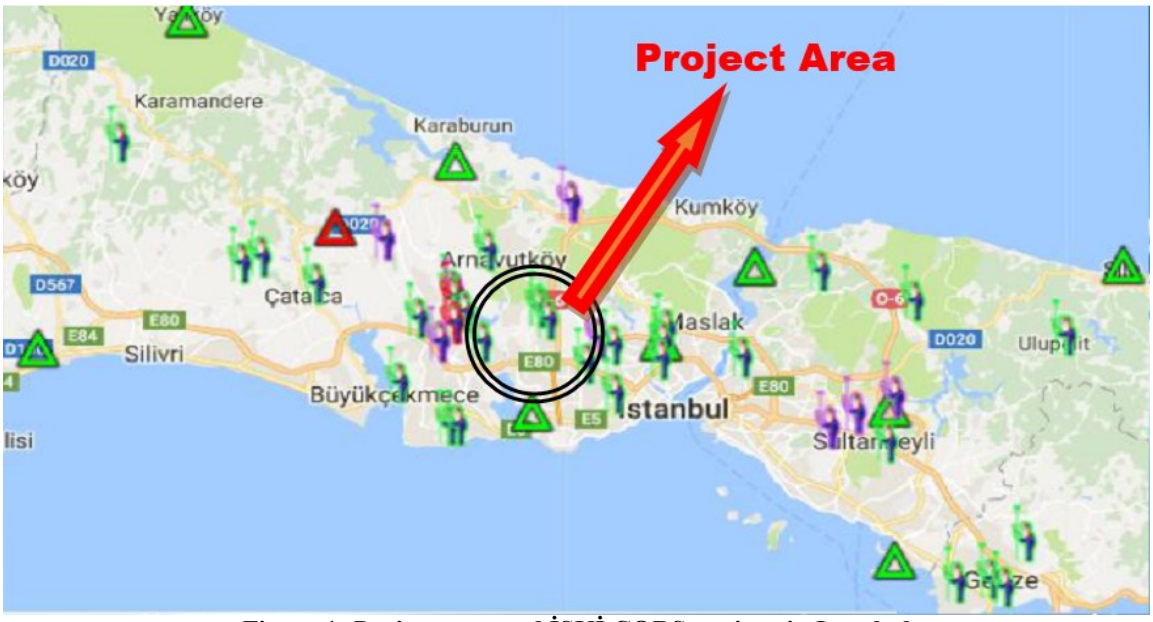

Figure 1: Project area and İSKİ CORS stations in Istanbul

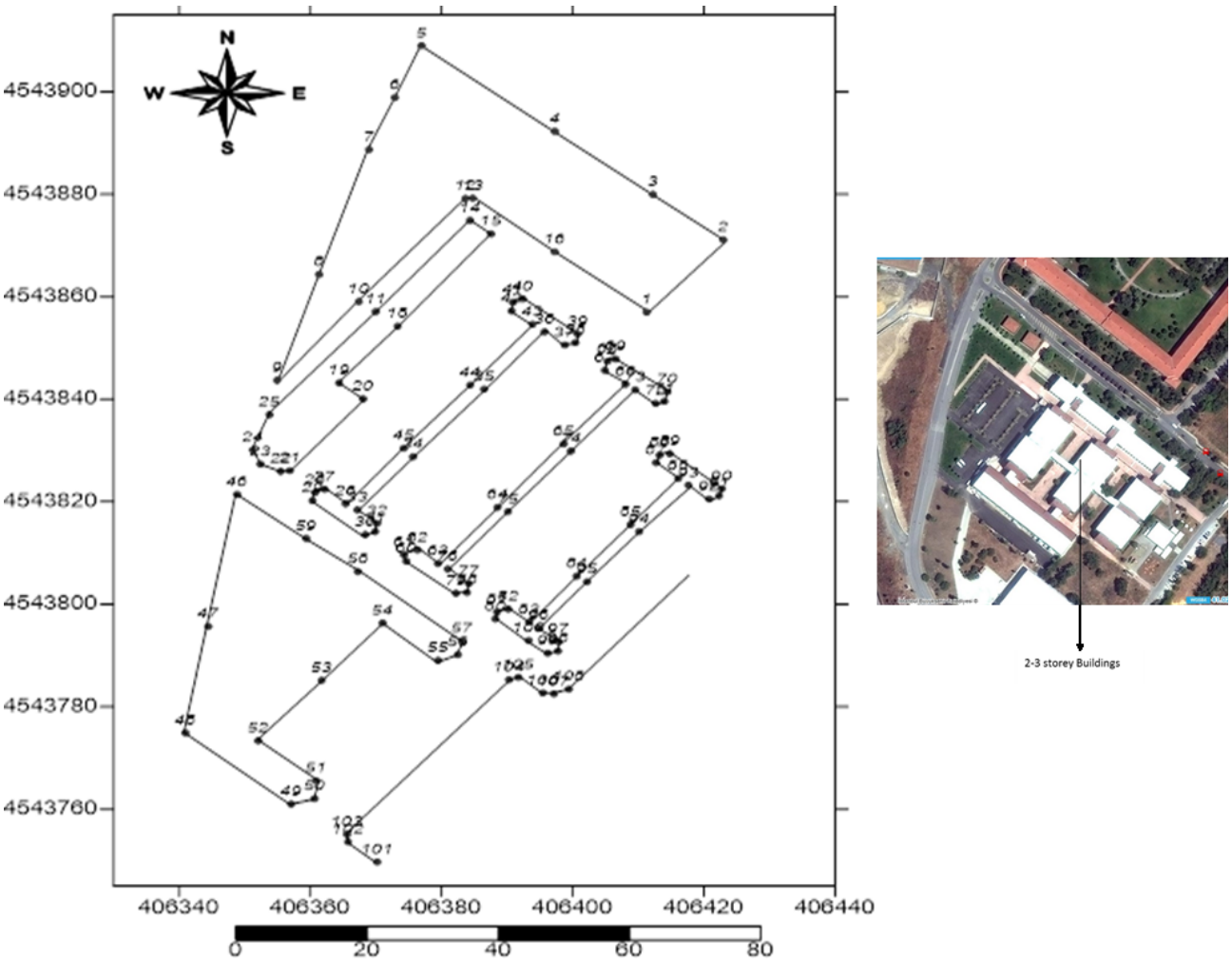

Figure 2: Distribution of test points in the project area

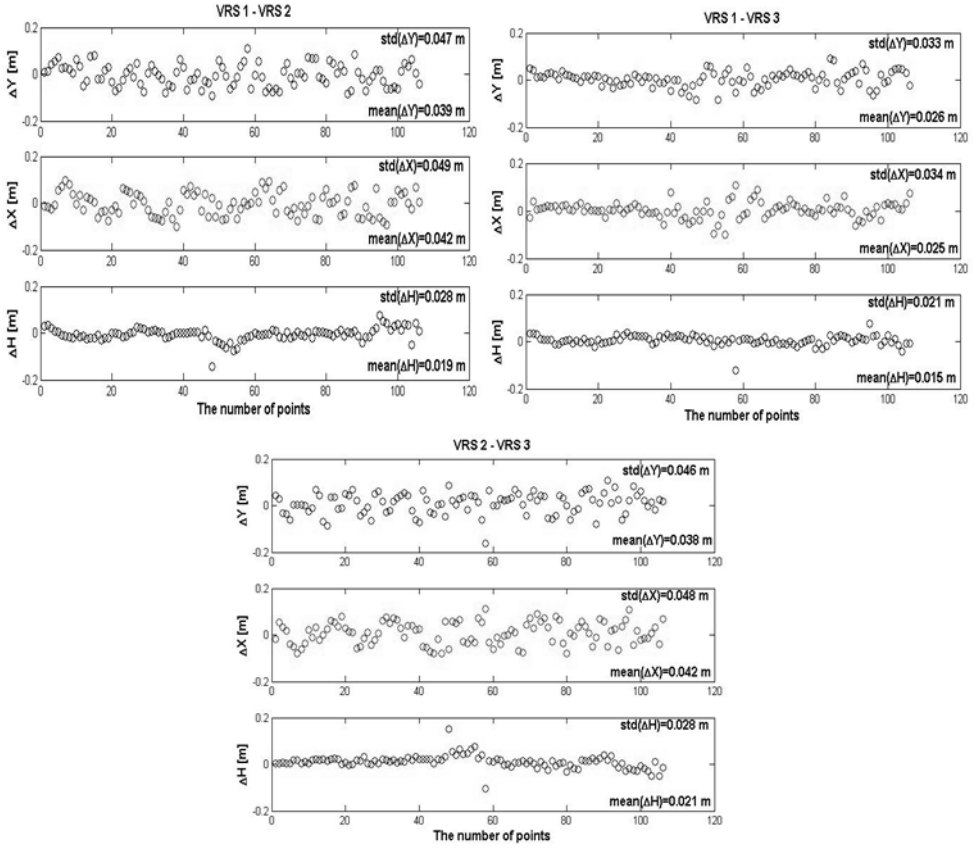

Figure 3: The comparison of the coordinates of the test points using VRS1, VRS2 and VRS3

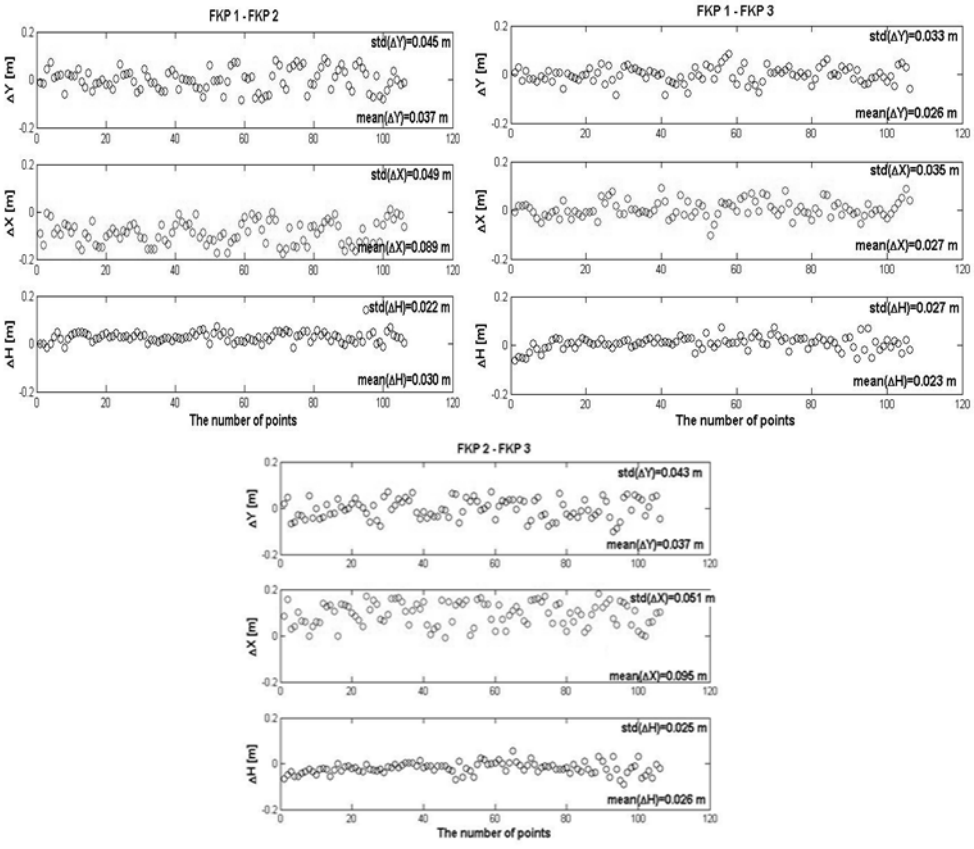

Figure 4: The Comparison of the coordinates of the test points using FKP1, FKP2 and FKP3

The X component was less consistent for FKP 2, and sometimes differed up to ±0.20 m at the same point between the FKP tests (Figure 4). Considering the dynamics involved in this test, and changing geometry of satellites near the building environment, in particular, were harmful to positioning, as they frequently blocked the signals of the low satellites. This is often subject to shadowing, diffraction and scattering of the satellite signal by building environments. Even though several satellites were shaded/blocked by the buildings, they can still be tracked by the receiver. Six-seven satellites (GPS+GLONASS) were visible at this period (FKP2). The PDOP value was between 3.1 and 4.8 at this period. The differences of X components for the CORS (FKP2) measurements are greater than the other two FKP surveys (FKP 1, FKP3).

3.2 Horizontal and Vertical Accuracy between VRS and FKP Techniques

In the third step of analysis, the coordinate differences of 108 points obtained from VRS1, FKP1, FKP2 and FKP3, such as VRS1 - FKP1, VRS1 - FKP2 and VRS1 - FKP3, respectively, were calculated. Figure 5 illustrates the differences and their mean values and standard deviations for 108 points. Examination of the differences in Figure 5 reveals that the standard deviation values are between 0.02 m and 0.05 m, the mean values are between 0.02 m and 0.09 m for the X and Y coordinate components.

However, the standard deviation values in the H direction are between ±0.02 m and ±0.03 m, the mean values are close to ±0.02 m. Analysis of the CORS results show that thee horizontal coordinate differences are between ±0.01 m and ±0.20 m. The differences in height coordinates are about ±0.10 metres (Figure 5). The analysis of the first, second and third days in the project area (VRS1, FKP1, FKP2 and FKP3) clearly shows that the horizontal and vertical coordinate differences are generally approximately ±0.02 m, see Figure 5. The differences of X components for the CORS (between VRS1 and FKP2) surveys are greater than VRS1-FKP1 and VRS1-FKP3 surveys because of the previously mentioned reasons.

In the fourth analysis step, the coordinate differences of 108 test points obtained from VRS2, FKP1, FKP2 and FKP3, such as VRS2 - FKP1, VRS2 - FKP2 and VRS2 - FKP3, respectively, were calculated. Figure 6 illustrates the differences and their means and standard deviations for the 108 points. When the differences in figure 6 are examined, the standard deviation values are between ±0.03 m and ±0.05 m, the mean values are between ±0.03 m and ±0.09 m for the X and Y coordinate components are obtained. However, the mean values in the direction of H are about ±0.02-0.03 m, standard deviation values are approximately ±0.02-0.03 m. Analysis of the techniques of the CORS results show that the horizontal coordinate differences and the height coordinate differences are between a few and ±0.20 m (Figure 6). Analysis of the first, second and third days in the project area (VRS2, FKP1, FKP2 and FKP3) shows that the differences in horizontal and vertical coordinates are generally between 2 cm and 10 cm.

In the fifth analysis step, the coordinate differences of 108 test points are gained from VRS3, FKP1, FKP2 and FKP3 were computed, such as VRS3 – FKP1, VRS3 – FKP2 and VRS3 - FKP3, respectively. Figure 7 indicates the coordinate differences and their mean values and standard deviations for the 108 points. In the examination of the coordinate differences in Fig. 7, the standard deviation values are between ±0.03 m and ±0.05 m, the mean values are between ±0.03 m and ±0.10 m are obtained for the X and Y coordinate components. However, the standard deviation values in the H direction are between ±0.02 m and ±0.03 m, the mean values are about 0.02 m. Analysis of the techniques of the CORS results show that the horizontal coordinate differences are between ±0.01 m and ±0.20 m. The height coordinate differences are between ±0.01 m and ±0.15 metres (Figure 7). Analysis of the first, second and third days in the project area (VRS3, FKP1, FKP2 and FKP3) shows that the differences in horizontal and vertical coordinates are generally between ±0.02 m and ±0.04 m.

In order to compare all of the results obtained from the VRS techniques, Figure 8a is prepared for the minimum and maximum differences in each coordinate component and the mean and standard deviation values calculated from these coordinate differences. To compare all of the results obtained from the FKP techniques, Figure 8b is prepared for the mean and standard deviation values calculated from these coordinate differences with minimum and maximum differences of each coordinate component. In order to compare the results obtained from both techniques (VRS and FKP), figure 9 is prepared for the minimum and maximum differences in each coordinate component and the mean and standard deviation values calculated from these coordinate differences. Thus the accuracy of the CORS results is presented as derived from the estimation process. Figure 9 shows the average standard deviations for all tests, in the Y, X, and H coordinate directions. The horizontal coordinates of all the points were good in general with standard deviation less than ±0.05 m on the average. Considering the dynamics involved in this test, and the changing geometry of satellites, the results clearly show that the CORS technique is a stable system, and the cm level of accuracy is generally obtainable (Figures 8 and 9), (Lachapelle et al., 2001; Landau et al., 2003; Vollath et al., 2000; Vollath et al., 2001; Vollath et al., 2002; Wübbena et al., 2001; Pirti, 2007; Pirti, 2008; Pirti et al., 2009).

The obtained results in this study are consistent with those of many other groups that made similar tests (Berber and Arslan, 2013; Gumus, 2016; Ma et al., 2011; Volker, 2009; Edwards et al., 2010). The accuracy values quoted by other authors for this situations are 1-2 cm in horizontal coordinates and 1.5-3.5 cm in height.

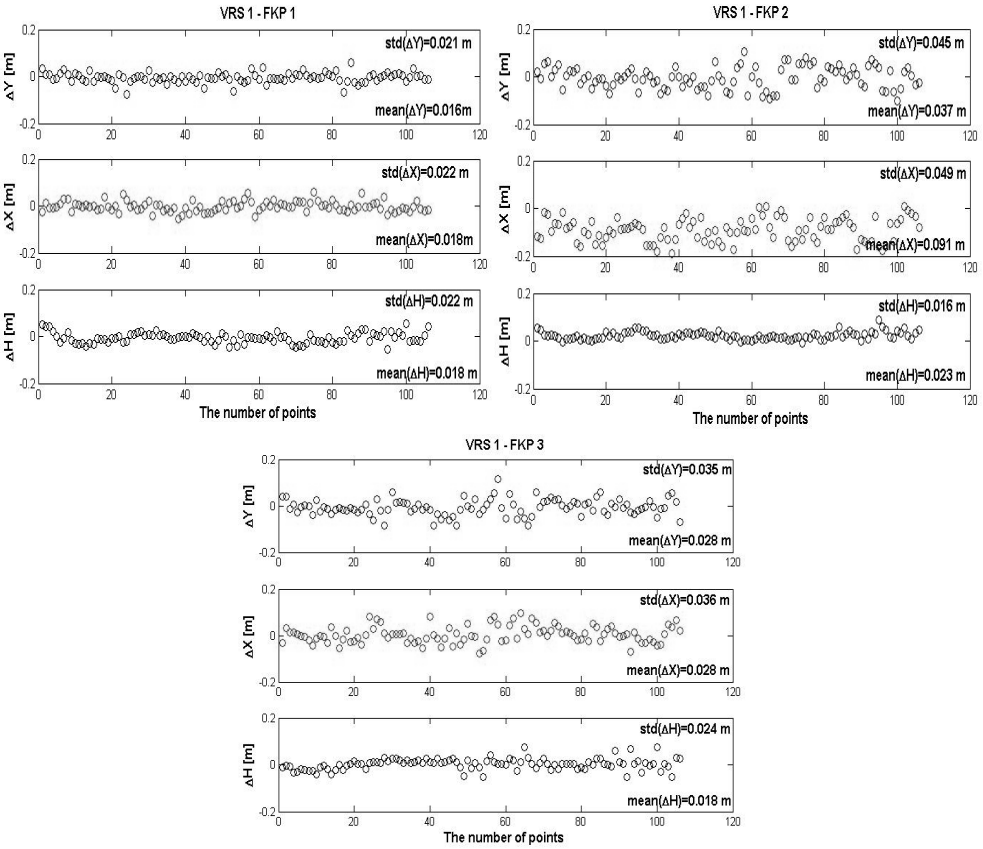

Figure 5: Comparison of the obtained coordinates of the test points by using VRS1 and FKP techniques

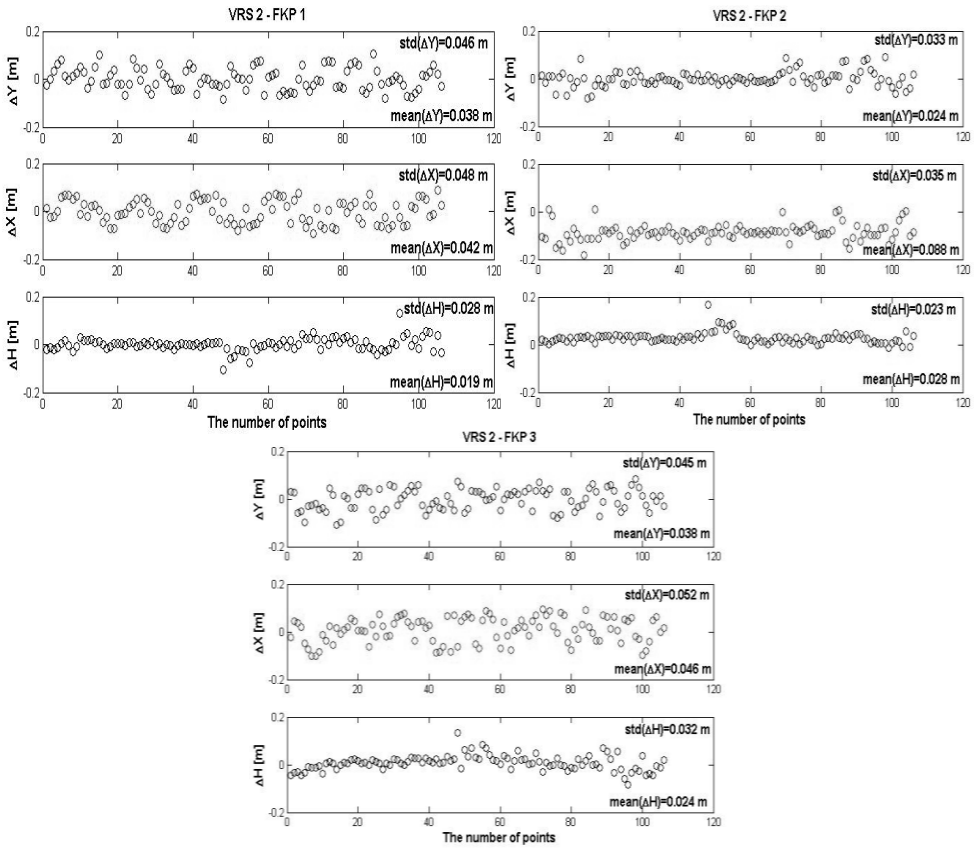

Figure 6: The comparison of the obtained coordinates of the test points using VRS2 and FKP

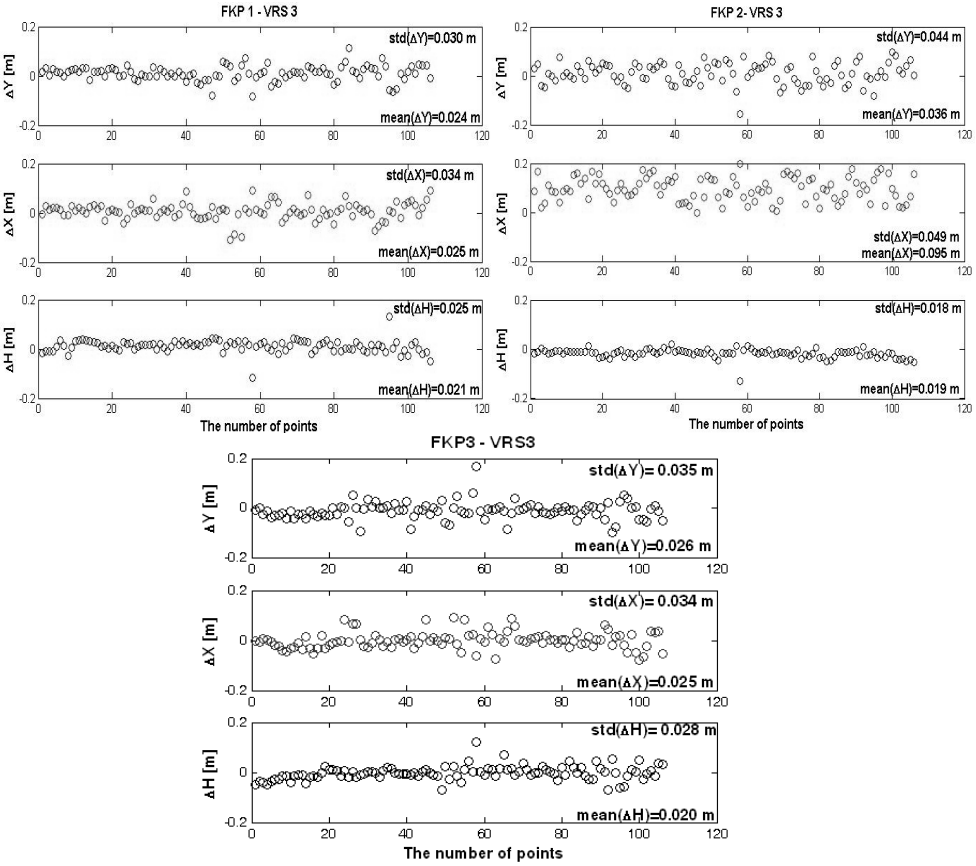

Figure 7: Comparison of the coordinates of the test points using VRS3 and FKP

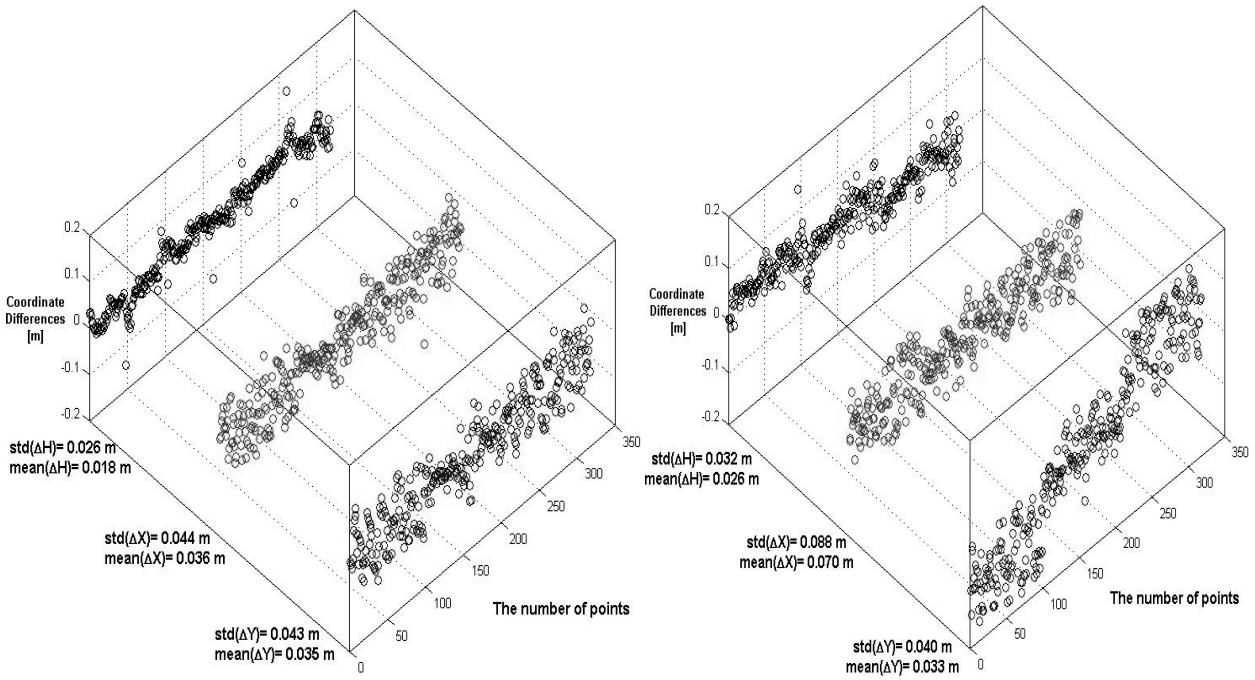

Figure 8: Comparison of the obtained coordinates of the test points by using VRS and FKP

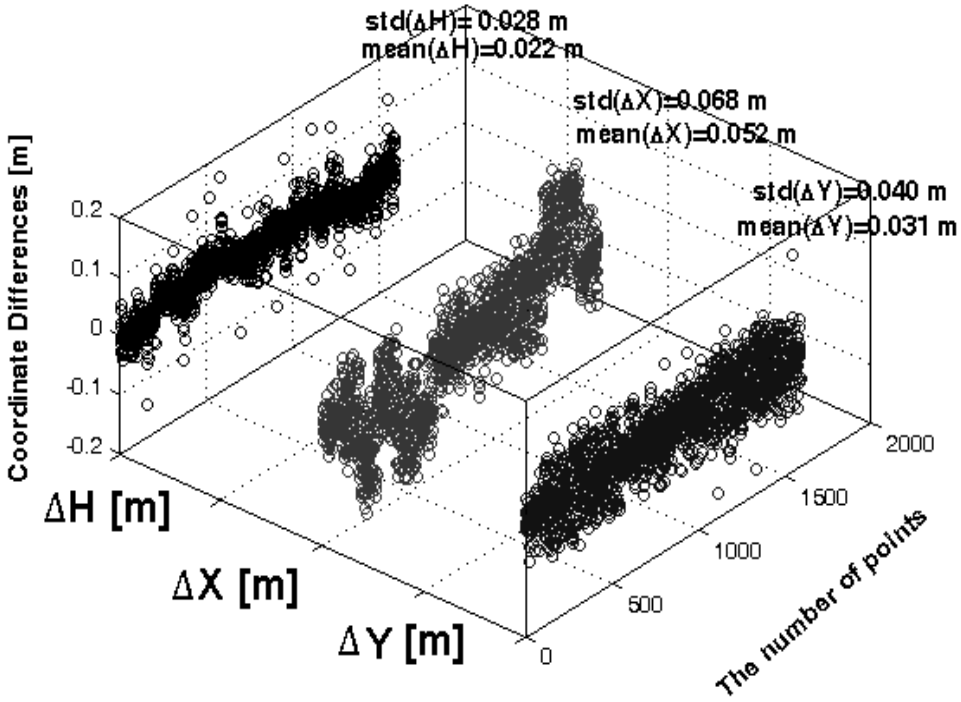

Figure 9: Comparison of the obtained coordinates of the points by using VRS-FKP in three days

4. Conclusions

Advances in communication technology have enabled the development and implementation of precise CORS. Although there are many considerations when implementing CORS, the achievable survey-grade accuracies provide new possibilities to data collection and applications. When comparing the CORS results of all the tests the horizontal and vertical coordinates of the test points as separately determined by these standard deviations and mean values seem generally very consistent, with changes ranging between ±0.01 m and ±0.20 m. It is shown in Figure 9, which gives the mean and the standard deviation values for all the points. In all the tests carried out in this study, reached an achievable and repeatable accuracy of approximately generally between ±0.03 m and ±0.07 m. The results in this study indicate that CORS positioning solutions from both VRS and FKP can achieve between 2 cm and 7 cm accuracy, which is required by the majority of topographic-geodetic applications.

References

Alves, D.B.M., L.F.A. Dalbelo, J.F.G. Monico and M.H. Shimabukuro (2011). First Brazilian real time network DGPS through the Internet: Development, Application and Availability Analyses, Journal of Geodetic Science, 2(1), 1-7.

Bae, T.S., D. Grejner Brzezinska, G. Mader and M. Dennis (2015). Robust analysis of network-based real time kinematic for GNSS derived heights, Sensors (15), 27215–27229,
DOI: http://dx.doi.org/10.3390/s151027215

Berber, M. and N. Arslan (2013). CORS. A case study in Florida, Measurement. (46), 2798–2806. DOI: http://dx.doi.org/10.1016/j.measurement.2013.04.078

Bisnath, S., A. Saeidi, J.G. Wang, and G. Seepersad (2013). Evaluation of CORS performance and elements of certification – a Southern Ontario Case study. Geomatica, (67), 243–251. DOI: http://dx.doi.org/10.5623/cig2013-050

Bock, Y., H. Cecil and M. Ida (2002). The California CORS Program, CORS Users Forum, National Geodetic Survey, NOAA/NOS, Silver Spring, Maryland.

Dai L., S. Han, J. Wang and C. Rizos (2003). Comparison of interpolation algorithms in network-based GPS techniques. Navigation, (50), 277–293. DOI: 10. 1002/j.2161-4296,2003.tb00335.x.

Edwards, S.J., P.J. Clarke, N.T. Penna and S. Goebell (2010). An examination of network RTK GPS services in Great Britain. Survey Review, 42(316): 107–121. DOI: https://doi.org/10.1179/003962610X12572516251529

Gumus, K. (2016). A research on the effect of different measuring configurations in CORS applications. Measurement (78), 334–343. DOI: http://dx.doi.org/10.1016/j.measurement.2015.10.022

Hoffmann-Wellenhof B., H. Lichtenegger and E. Wasle (2008). GNSS-GPS, GLONASS, Galileo and more: Springer, Wien & NewYork.

Lachapelle, G., L.P. Fortes, M.E. Cannon, P. Alves and B. Townsend (2001). RTK Accuracy Enhancements with a Reference Network−Based Approach, the Third International Symposium on Mobile Mapping Technology. January 3-5, Cairo, Egypt.

Landau H., U. Vollath and X. Chen X (2003). Virtual Reference Stations versus Broadcast Solutions in CORS – Advantages and Limitations. Proceedings of GNSS 2003–The European Navigation Conference, April 22-25, 2003, Graz, Austria.

Ma, S.G., G. Elena, C. Ma and J. Antonio (2011). Testing precise positioning using RTK and NRTK corrections provided by MAC and VRS approaches in SE Spain. Journal of Spatial Science, 56(2), 169-184. DOI: 10.1080/14498596.2011.623341

Pirti A. (2007). Performance analysis of the Real Time Kinematic GPS (RTK GPS) technique in a highway project (Stake-Out), Survey Review, 39(303), 43-53. DOI: 10.1179/003962607X164989

Pirti, A. (2008). Evaluating the usage of RTK GPS technique in the control of highway geometry, Geodetski List, 62(4), 237-248. DOI: http://hrcak.srce.hr/32767

Pirti, A., N. Arslan, B. Deveci, O. Aydin, H. Erkaya and R.G. Hosbas (2009). Real time kinematic GPS for cadastral surveying, Survey Review, 41(314), 339-354. DOI**:** 10.1179/003962609X451582

Talbot N., G. Lu, T. Allison and U. Vollath (2002). Broadcast CORS-transmission standards and results; Proceedings of the 15th International Technical Meeting of the Satellite Division of the Institute of Navigation. (ION GPS 2002), 24–27 September, Portland, OR, USA.

Volker, J. (2009). A comparison of the VRS and MAC principles for network RTK, International Global Navigation Satellite Systems Society IGNSS Symposium, 1-3 December 2009, Surfers Paradise, Australia.

Vollath, U., A. Deking, H. Landau and C. Pagels (2001). Long range RTK positioning using virtual reference stations, Proceedings of the International Symposium on Kinematic Systems in Geodesy, Geomatics and Navigation, June, Banff, Canada.

Vollath U., A. Deking, H. Landau, C. Pagels, and B. Wagner, (2000). Multi-Base RTK positioning using virtual reference stations, Proceedings of the 13th International Technical Meeting of the Satellite Division of the Institute of Navigation, Salt Lake City, Utah, USA, September.

Vollath U., H. Landau and X. Chen (2002). CORS versus single base RTK – Understanding the error characteristics, Proceedings of the 15th International Technical Meeting of the Satellite Division of the Institute of Navigation, September, Portland, Oregon, USA.

Wolf P.R. and C.D. Ghilani (2008). Elementary Surveying, an Introduction to Geomatics. 12th Edition, Prentice Hall Upper Saddle River, New Jersey, 960 p.

Wübbena, G., A. Bagge and M. Schmitz (2001). Network Based Techniques for RTK Applications. GPS JIN 2001, GPS Society, Japan Institute of Navigation, Tokyo, Japan, November 14-16, 53-65.

Journal of Geomatics Vol. 14, No. 1, April 2020

Dynamic simulation of land use change in Bashang desertification region of Hebei Province using CA-Markov Model

PENG Bo[1], WEN Zhehua[2], FAN Huitao[1], NIU Qinghua[1], GUO Yujia[1] and GU Jiancai[1*]
[1]College of Forestry, Hebei Agricultural University, Baoding, Hebei Province - 071000, China
[2]Hebei Forestry and Grassland Administration, Shijiazhuang, Hebei Province - 050081, China
*Email: 530898056@qq.com

(Received: Apr 18, 2019; in final form: May 15, 2020)

Abstract: Study of regional land use is important for planning of urban construction and ecological restoration. We report the dynamic characteristics of land use and modeled direction of land use transformation using the ARCGIS and IDRISI software in the desertification region in Hebei Province. Analysis is based on the interpretation data of remote sensing images of 2004, 2009 and 2014. The CA-Markov model was employed to simulate and predict the land use trend in the study area in 2019. It was found that (1) The land use changed significantly between 2004 and 2014. The area of cultivated land continued to increase, the area of forestland and grassland decreased continuously, the construction land increased rapidly, and the water area changed little. (2) There was obviously directional movement of cultivated land, forestland, grassland and construction land from 2004 to 2014. Grassland cultivated land and construction land had a trend of convergence, while forestland and other types of land were scattered (3) Compared with the period from 2004 to 2014, the areas of cultivated land, forestland and construction land increased, and the area of grassland continued to decrease from 2014 to 2019. The increasing speed of cultivated land significantly slowed down and the construction land increased sharply. The approach demonstrated in this study can be utilised to guide the coordinated development of land use and ecological protection in desertification areas.

Keywords: Desertification area, Land use, CA-Markov, Dynamic simulation

1. Introduction

The change of land use is the succession of the interference of human activities to land. As an important procedure of global and regional environmental change, land use affects the ecological environment (Wang and Zang, 2006; Yu and Yang, 2002; Xu et al., 2017) and brings the changes in many ecological processes of ecosystems on different scales, such as soil erosion, surface runoff and non-point source pollution (Guo et al., 1999; Yu et al., 2004). Land use is closely related to land desertification resulted by climate and unreasonable utilization of resources (Chen, 1996; Xu et al., 2009; Xu, 2007). Unreasonable land use will lead to a sharp decline in land productivity, continuous decreases in land resources and biodiversity (Wang and Wu, 1999; Bai and Li, 2013). Study on the characteristics and its dynamic changes and prediction on the future status of regional land use on different spatial and temporal scales helps to understand the process and mechanism of ecological environment change under the influence of human activities, which is of great significance for ecological protection and sustainable development.

Presently different types of dynamic simulation model are used for studying land use change analysis viz., System Dynamic (SD) (Xie et al., 2008), Cellular Automata (CA) (Zhou and Li, 2012), Markov (Markov) (Guan and Weijun, 2008; Zhou et al., 2010) and Logistic, etc. CA-Markov, also known as spatial-temporal Markov chain (STMC), is a widely used coupling model (Mondal et al., 2016; Halmy et al., 2015), which combines the advantages of long-term prediction of Markov model and the ability of CA on simulating the spatial change of complex system. It improves the prediction accuracy of the transformation and effectively simulate the spatial change of land use type (Liu et al., 2010; Wu et al., 2017).

Bashang desertification area, located in the north-west of Hebei Province, is an ecologically fragile area. Deteriorating ecological condition of this region is due to grassland degradation and reduction of biodiversity due to the long-term human disturbance, such as excessive grazing, felling, and reclamation. In this study, Bashang desertification area was chosen as the research area. The data of land use in 2004, 2009 and 2014 are collected and used as input parameters in the MEC model, Markov model, land use focus conversion model and single dynamic of land use. Based on the IDRISI Andes 17.0 software, the CA-Markov model was employed to predict and analyse the spatial pattern of land use in the study area for 2019. It reveals the trend of land use, which is of vital importance to the ecological environment protection and sustainable development of the Bashang Desertification Area.

2. Methodology

2.1 Research area and data

The Bashang desertification area located in the north-western part of Hebei Province, which is between 114°50′38′′ and 116°04′09′′ E, 41°14′33′′ and 41°56′55′′N with temperate continental grassland environment. The annual average temperature of the region is 1.6°C. The annual average precipitation is 426 mm. The frost-free period is 117 days, and the rainy season of the region is mainly in June, July, and August, with 53% of the annual precipitation.

The Landsat TM images of 2004, 2009 and 2014 were collected as the main data with resolution of 30 m. According to the land use classification criteria

documented in the Land Administration Law of the People's Republic of China (National People's Congress Standing Committee, 1998), the land uses in the study area are classified into five main categories: arable land, forestland, grassland, water, and construction land.

2.2 Markov Model

Markov model is a stochastic model with a finite time series: $t_1 < t_2 < t_3 \ldots t_n$. In the Markov process, the state a_n at time t_n is only related to the state a_{n-1} at time t_{n-1}. This simulation is mainly used in the study of the change in land use. The area or ratio of land use types converted to each other constitutes the state conversion probability. The future status of land use is predicted by the conversion matrix. The formula is as follow (Gao and Zhao, 2002):

$$S_{t+1} = P_{ij} \times S_t$$

Where, S_{t+1} and S_t are the states of the land use system at the time of t+1 and t, respectively.

P_{ij} is a state conversion matrix, which can be expressed by the following formula:

$$P_{ij} = \begin{vmatrix} P_{11} & \cdots & P_{1n} \\ \cdots & \cdots & \cdots \\ P_{n1} & \cdots & P_{nn} \end{vmatrix}$$

Where, $0 \le P_{ij} \le 1$ and $\sum_{j=1}^{n} P_{ij} = 1,\ (i, j = 1,2, \ldots, n)$.

2.3 MCE Model

The MCE model is applied to find out the optimal decision and set a series of evaluation criteria (Fang et al., 2014), formulate corresponding criteria for different objectives, and to assist decision-making through a comprehensive analysis of many factors affecting the objectives (integrating the information of two kinds of decision-making criteria: constraint conditions and suitable factors).

In this study, distance and land use are applied as constraints, while the binary values of five factors, town, water, road, slope and construction land, are standardized as Boolean images. The following six main standards are adopted:

1. Distance constraints: Considering the shortage of water source and water pollution, the value is 0 in the buffer range of 50m, and the values of others are 1.
2. Current land use constraints: According to the classification of this study, the suitability score of water area and construction land is set to 0, and those of other types are set to 1.
3. Distance factor of water area: For environmental protection, the buffer distance within 100m is not suitable for development, with a score of 0. The values of others are set to 1.
4. Distance from roads: Knowing the impact of road traffic on economic development is very strong. Within 500 meters from road traffic, the value is 1, and the values of others are 0.
5. Slope factor: According to China's "Work Regulations on Soil and Water Conservation", the lands with slope gradient above 25 degrees are no-tillage area. The suitability values for the areas with slope gradient above 25 degrees are set to 0 and other values are set to 1.
6. Distance factor of construction land: Construction land has a significant impact on the conversion of surrounding land, and the longer the distance, the smaller the attraction until no difference is achieved. Therefore, the value of distance less than 300 m from the construction land is set to 1, the values of others are set to 0.

2.4 Dynamic Degree of Land Use

The dynamic degree of land use refers to the quantitative change of a certain land use type in a certain time range in a certain research area. The dynamic degree indicates the stability of the land use type (Duan et al., 2005). This rate reflects the level of a dramatic change of the regional land use. The following formula indicates the method for calculating the dynamic degree of a type of land use:

$$K = \frac{U_b - U_a}{U_a} \times \frac{1}{T} \times 100\%$$

Where, U_a is the original state of the land type, U_b is the area of land use at the end of the period; T is the duration of the data collection in these years.

2.5 Focus conversion model of land use

The focus of land use is used to characterize the spatial position and change in the process of land development and utilization (Li et al., 2017).

The calculation method is as follows:

$$X_k = \frac{\sum_{i=1}^{n}(A_{ki} \times X_{ki})}{A_k}, Y_k = \frac{\sum_{i=1}^{n}(A_{ki} \times Y_{ki})}{A_k}$$

Where, X_k and Y_k are the coordinate barycentres of X and Y for land use types of k, A_{ki} is the area of i patches for land use type of k, X_{ki} and Y_{ki} are the geometric coordinate centres of X and Y for i patches of the land use type of k, and A_k denotes the total area of k land use types.

2.6 CA-Markov Model

Cellular automata (CA) is a dynamic model with discrete time, space and state, which can effectively simulate the spatial changes of the system. The CA model formula (Zhou et al. 2003) is:

$$S_{t+1} = f(S_t, N)$$

Where, S is a finite and discrete set of states, t, T + 1 are different times, N is the neighborhood of cells, and f is the rule of cell transformation in local space.

Using the IDRISI Andes 17.0 software and the data of Markov and CA, land use change prediction is carried out. The results of future land use are analyzed according to land use dynamic degree. CA-Markov Model releases the spatial relationships to ensure the land use is converted into the most recently stored land use type, rather than completely randomized (Liu and He, 2003).

The specific prediction process is as follows:

1. Calculating the conversion matrix of land use: The interpreted data of 2004 and 2009 are analyzed by superposition (Figure 1, area matrices of conversion probability and conversion are calculated by the Markov model in IDRISI).

2. Establishment of suitability atlas: The Collation Edit module of IDRISI software is used to produce conversion suitability Atlas of different types of land use by MCE model to integrate different criteria and predict the change of land use.

Setting relevant parameters: The current data of land use in 2009 was used as the basic data, and the year 2009 was set as the basic point of prediction time. The default 5*5 cellular filter was used to define neighbors and predict the distribution of land use in 2014. The kappa coefficient of 0.7593 was used to test the actual interpretation data in 2014. The higher simulation prediction accuracy makes the year 2014 suitable for being the base period data, and the spatial distribution of land use in the year of 2019 was then measured.

3. Results and Analysis

3.1 Dynamic Change Characteristics of Land Use

The area under cultivated land and construction land had increased steadily from 2004 to 2014 (Figure 1 and Table 1). Among them, the area of cultivated land increased by 133.49 km^2 and the area of construction land increased by 22.75 km^2. The area of forestland and grassland decreased by 77.23 km^2 and 79.53 km^2, respectively. Decrease in water area was less significant. For the structural change, the arable land area ratio has increased significantly, and the proportion of arable land area in the total study area exceeded 40% by 2014. The proportion of land area decreased from 28.44% to 26.06% and grassland from 29.04% to 26.60%. The proportion of construction land increased from 2.87% to 3.57% in 10 years. The water area changed very small, and the proportion of the water area is keeping nearly stable at 2.4% of the total area.

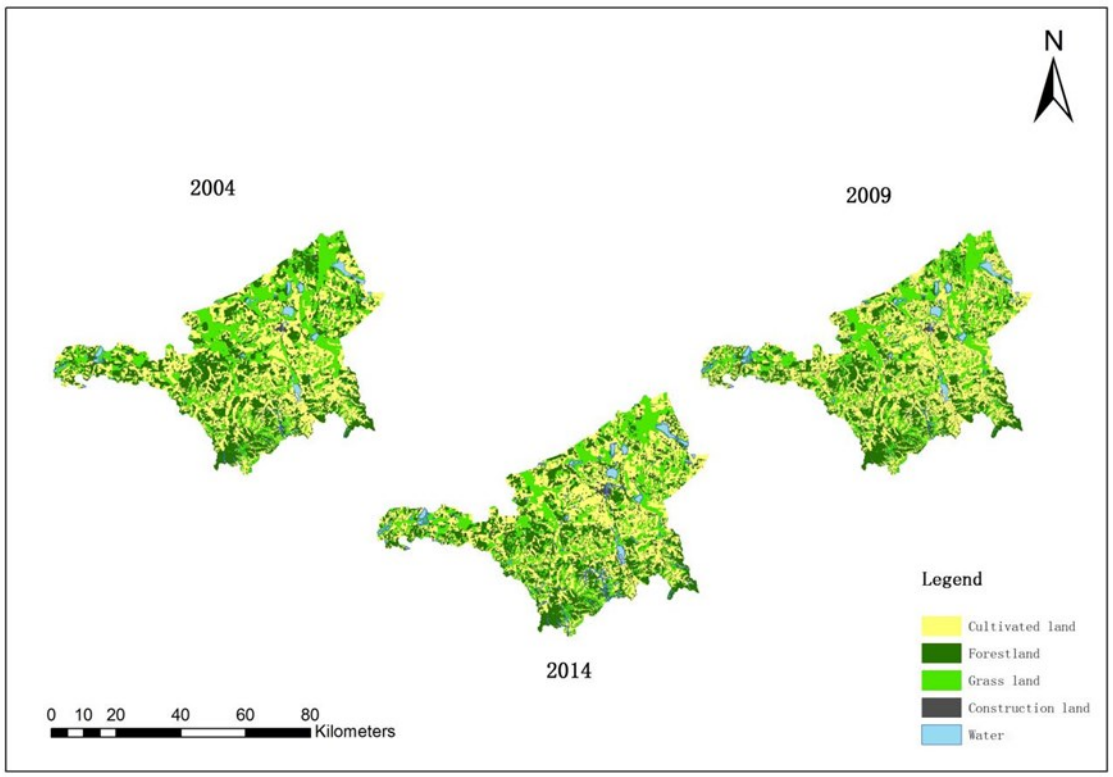

Figure 1: Interpretation of land use in the study area from 2004 to 2014

Table 1: Areas of different types of land use in different stages of desertification in Bashang

Land use types	2004		2009		2014	
	Area/ km^2	Proportion %	Area/ km^2	Proportion %	Area/ km^2	Proportion %
Cultivated land	1210.75	37.28	1297.78	39.96	1344.24	41.39
Forest land	923.61	28.44	859.53	26.46	846.38	26.06
Grass land	943.38	29.04	916.48	28.22	863.85	26.6
Construction land	93.29	2.87	97.85	3.01	116.05	3.57
Water	76.99	2.37	76.39	2.35	77.51	2.39

3.2 Spatial Direction Conversion of Land Benefit

The conversion matrix of land use can be obtained by the Markov module of IDRISI software from 2004 to 2014. Between 2004 and 2014, the land conversion in the study area is slightly larger and more complex. The area of converted cultivation land is the largest and mainly come from grassland and forestland. The intensity of grassland conversion is higher. The grassland was mainly converted to cultivated land and construction land by the areas of 287.05 km^2 and 5.93 km^2, respectively. Forestland conversion intensity mainly converted to grassland and cultivated land conversion area is 206.12 km^2 and 34.37 km^2 respectively. Construction land conversion is more obvious. The Construction land is mainly come from cultivated land by the area of 16.05 km^2. The change in the water area is very small, and the area is mainly from the conversion of cultivated land, grassland, and forestland (Table 2).

3.3 Simulated Prediction of Land Use Change

3.3.1 Change of land use focus

From 2004 to 2014, except water, the other four types of land use changed significantly. These four types of land use are important factors affecting socio-economic development and grain yield in the study area. Taking these four types of land as representatives, the change of the focus is analyzed, and the distribution of the focus of the study area in 2004-2014 and the forecast results are obtained by using (Geographic Information System) GIS spatial analysis tools (Figure 2), to predict the future change of land use.

From figure 2, it can be seen that the centre of gravity of cultivated land moved 1148 m eastward and 1622 m southward from 2004 to 2009, with the fastest moving speed. Grassland and construction land moved 568 m to the southwest and 1065 m to the northwest respectively. It shows that while the cultivated land and construction land expanded around, they tended to develop toward flattening areas in the study area. Between 2009 and 2014, the cultivated land moved 1145 m to the northwest, almost unchanged from 2004 to 2009. It moved 1484 m to the southeast and the moving speed slowed down. The grassland maintained its development direction and speed in the last period. The construction land moved 144 m to the northeast and the moving speed slowed down. From 2004 to 2014, the centre of gravity of cultivated land moved to the north, the forestland moved to the southeast, the grassland moved to the southwest, and the construction land moved to the northwest.

3.3.2 CA-Markov Model Simulation Accuracy Test

At present, the CA-Markov model does not have a model accuracy-test standard, therefore, this study uses the kappa coefficient as a criterion to determine the accuracy of the model. The area of each land use type in the simulation results is compared with the area of actual land use area (Figure 3). If the image of land use benefit in the two periods is completely consistent, Kappa equals 1; When $0 \leq$ Kappa ≤ 0.4, the results have a low consistency. If $0.4 \leq$ Kappa ≤ 0.75, which indicates that the consistency is general. When Kappa ≥ 0.75, the consistency is high. Through the Crosstab module, the accuracy of quantitative analysis of the Kappa coefficient is obtained by comparing the simulation results and interpretation results. The Kappa coefficient obtained in this study is 0.7593, which indicates the accuracy of simulation prediction is relatively high and the results have high credibility and applicability.

3.3.3 Analysis of simulation results of the CA-Markov model

According to the predicted results of land use in 2019 (Table 3), it can be seen that the area of cultivated land decreased during the period between 2014 and 2019 is even more than the total area of grassland decreased in the two periods, 2004-2009 and 2009-2014; the change in the land area shows a greater fluctuation. The area of forestland between 2004 and 2014 is in a decreasing stage, but the speed of reduction is continuously decreasing, and the area of forestland has an increase between 2014 and 2019. But from the number, the area of forestland in 2004-2019 is still decreasing. Construction land shows a strong growth trend during the study period, it increased by 4.56 km^2 in 2004-2009. According to the prediction results, the growth of construction land will reach 31.07 km^2 in 2014-2019. From the dynamic degree of land use type change, the growth rate of the cultivated land area is slowing down, and the dynamic degree is decreasing.

Table 2: Area of land transferred to desertification area in Bashang area from 2004 to 2014, unit in km^2

Land use types		2014				
		Cultivated land	Forestland	Grassland	Construction land	Water
2004	Cultivated land	1019.14	164.78	9.02	16.05	1.77
	Forestland	34.37	675.27	206.12	6.74	1.11
	Grass land	287.05	5.08	643.69	5.93	1.64
	Construction land	2.32	0.69	2.76	87.16	0.36
	Water	1.37	0.57	2.27	0.16	72.63

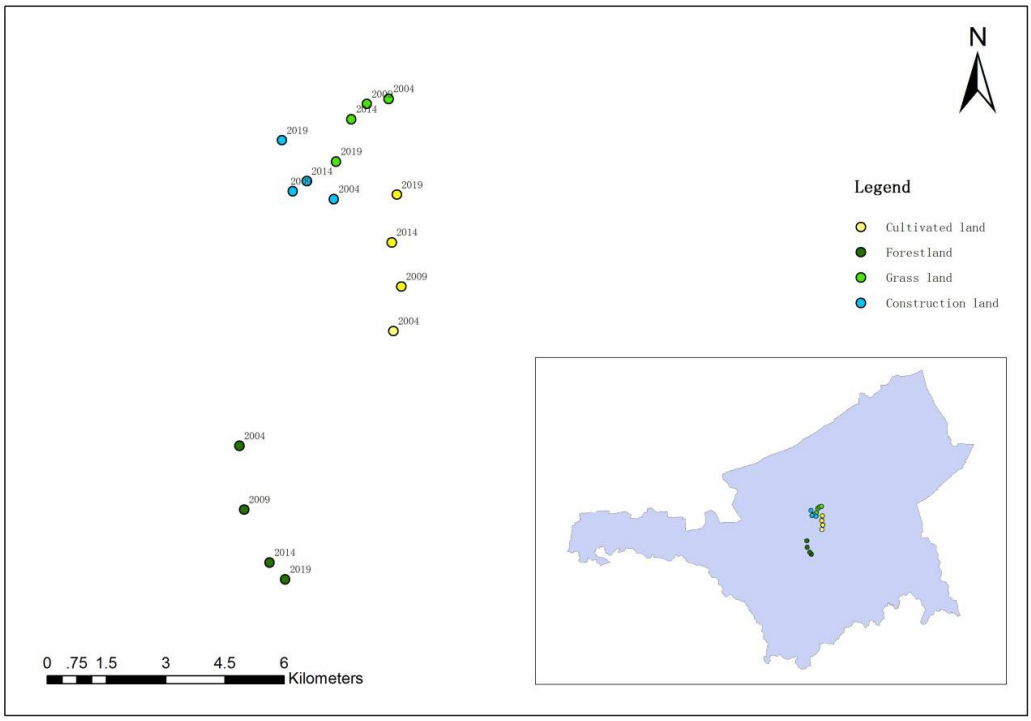

Figure 2: Spatial distribution of land use centre of gravity

Table 3: Changes in land use space in the study area from 2004 to 2019

Land use types	Predicted Area/km^2	From 2004 to 2009		From 2009 to 2014		From 2014 to 2019	
	2019	Area change (km^2)	Dynamic degree (%)	Area change (km^2)	Dynamic degree (%)	Area change (km^2)	Dynamic degree (%)
Cultivated land	1360.37	87.03	1.44	46.46	0.72	16.14	0.24
Forestland	884.74	-64.08	-1.39	-13.15	-0.31	38.34	0.91
Grass land	779.44	-26.90	-0.57	-52.63	-1.15	-84.42	-1.95
Construction land	147.12	4.56	0.98	18.19	3.72	31.07	5.36
Water	76.37	-0.61	-0.16	1.13	0.29	-1.14	-0.29

The dynamic degree of 2004-2009 is 1.44, the dynamic degree of 2009-2014 and 2014-2019 is 0.72 and 0.24 respectively; the forest area is increasing, and the dynamic degree is changing from negative to positive; the grassland is decreasing rapidly, and the dynamic degree from 2009 to 2014 and from 2014 to 2019 are negative 1.15 and negative 1.95. The area of construction land increases rapidly, and the dynamic degree reached 3.72 and 5.36 in 2009-2014 and 2014-2019, respectively.

As can be seen from figure 4, the cultivated land and construction land in the study area are mainly distributed in the flat terrain, low altitude area, mostly around grassland, and construction land is expanding outward. With the acceleration of urbanization, the increase of construction land area is an inevitable result, and the increase of population will intensify reclamation, resulting in the transformation of other land use types, especially grassland to cultivated land and construction land. Urbanization and population growth are bound to require social and economic support, which requires forestland to provide services for them, resulting in the conversion of part of the forestland into arable land. After forestland and grassland degenerated and reclaimed as arable land, the soil lost the protection of vegetation in the idle season. This resulted in soil loosening, which led to land desertification, accelerated the expansion of sandy land and the activities of desert marginal dunes, coupled with technical and socio-economic constraints, which made the land lose nutrients, and then continued to expand the area of arable land, forming a vicious circle.

4. Discussion

Numerous studies have shown that there are some differences in the impact of land use types on desertification (Ge et al., 2010; Wang et al., 2010; Lv et al., 2007; Zhang et al., 2009). Over the past 10 years, the area of cultivated land has been increasing, the forestland and grassland have been decreasing, and the expansion of construction land must occupy a large amount of cultivated land and grassland, which undoubtedly changes the land use pattern of the desertified area. In order to increase grain production and further increase economic benefits, local people continue to reclaim the

flat forestland and grassland around cultivated land, and the over-reclamation has resulted in the increase of cultivated land and the degradation of grassland. It makes the soil loose and leads to desertification. After the forestland and grassland are reclaimed as cultivated land, the soil loses the protection of vegetation in the fallow season, thus accelerating the expansion of desertified land and the activities of sand dunes on the edge of the desert. Together with technical and socio-economic constraints, the land loses nutrients, and consequently expands the area of cultivated land and forms a vicious circle. The forest land resources in the study area are relatively abundant, distributed in areas with a high elevation and complex topography. The proportion of water area is small, and the ecology is relatively fragile, so it is difficult to recover after damage. Due to the limitation of landform, cultivated land and grassland are greatly affected by human activities. According to the simulation results, the land use change in desertification area is very active, and the desertification control is still a tough job. Therefore, controlling sufficient arable land per capita, reducing fertilization intensity, improving farmers' technical level and land use level, retaining enough ecological land in desertification areas and saving intensive use of construction land are important measures to slow down land desertification.

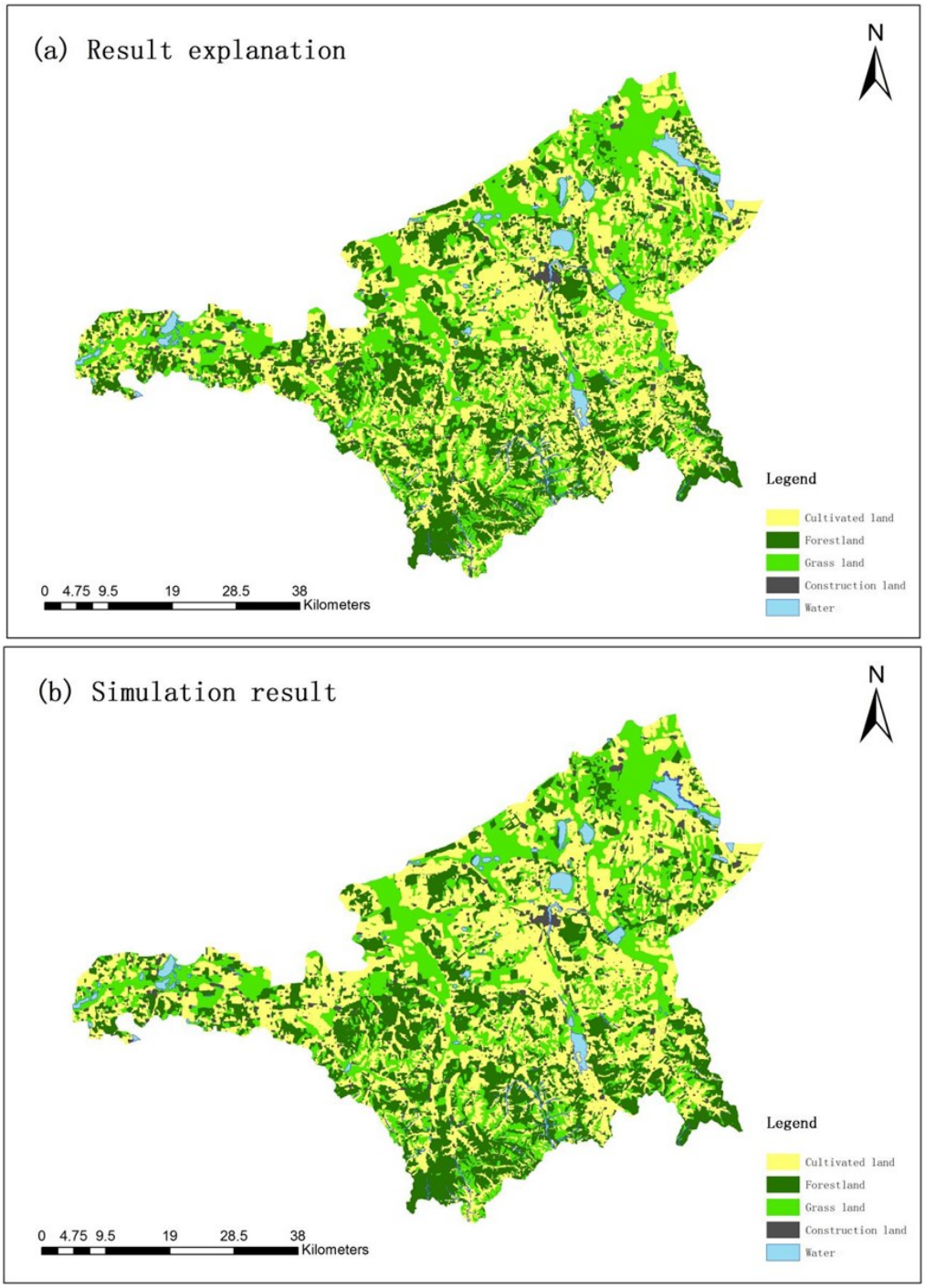

Figure 3: Verification of land use type prediction accuracy in the study area: (a) Result explanation; (b) Simulation result

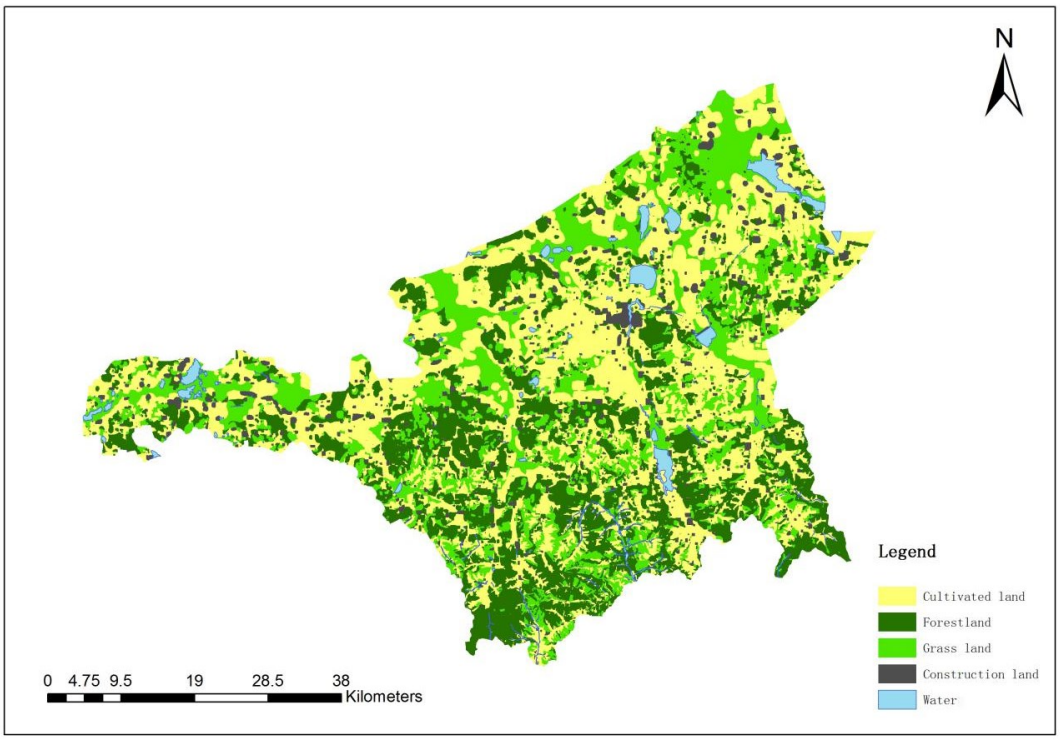

Figure 4: Predicted land use types in the study area using CA-Markov model

Table 4: Changes in land use space in the study area from 2004 to 2019

Land use types	Predicted Area/km²	From 2004 to 2009		From 2009 to 2014		From 2014 to 2019	
	2019	Area change (km²)	Dynamic degree (%)	Area change (km²)	Dynamic degree (%)	Area change (km²)	Dynamic degree (%)
Cultivated land	1360.37	87.03	1.44	46.46	0.72	16.14	0.24
Forestland	884.74	-64.08	-1.39	-13.15	-0.31	38.34	0.91
Grass land	779.44	-26.90	-0.57	-52.63	-1.15	-84.42	-1.95
Construction land	147.12	4.56	0.98	18.19	3.72	31.07	5.36
Water	76.37	-0.61	-0.16	1.13	0.29	-1.14	-0.29

Land use simulation is a complex process, which is affected by many factors. These factors are often difficult to quantify. In addition, the spatial resolution and interpretation accuracy of TM remote sensing images limit the accuracy of model simulation results to some extent. In the future, we should further identify key drivers, especially human factors, taking into account the scale effect. The simulation results are more realistic and reasonable to guide the coordinated development of land use and ecological protection in desertification areas.

5. Conclusion

Based on the Markov model and GIS and remote sensing technology, we analyzed the spatial-temporal characteristics and trends of land use types in desertification areas from 2004 to 2014. Six influencing factors of distance and land use area were selected to participate in the formulation of conversion rules. IDRISI software is used to simulate and forecast land use in Desertification Area in 2019. MCE method is used to simulate the change of land use spatial pattern in 2014 with GIS. The actual interpretation results in 2014 are compared and validated. The Kappa coefficient of the simulation results is 0.7593, with high accuracy and reliability, which can be used for future land use simulation and prediction. The formulation of conversion rules can improve the accuracy of prediction results, so as to provide a scientific basis for the protection of land resources and decision-making of regional land use planning.

The main characteristics of land use conversion are as follows: from 2004 to 2014, the cultivated land area increased continuously, mainly from grassland and forestland, and the center of gravity of cultivated land moved steadily to the northward; because of the continuous degradation of forestland and the conversion from forestland to grassland, the area of forestland continued to decrease and its center of gravity of forestland moved southeast; grassland was the main utilization type of human beings, and the area of grassland was mainly converted to cultivated land and construction land. As a result, the grassland area

continued to decrease, and the grassland gravity center accelerated to move to the southwest; the transfer of cultivated land, and the construction land gravity center moving to the northwest bring the continuous expansion of construction land; the water area changed very little, and the figure of the change was not obvious.

From 2014 to 2019, the area of cultivated land continued to increase, but the increase rate decreased, which is about one-third of the area of cultivated land increased in 2009-2014 and one-fifth of the area of cultivated land increased in 2004-2009. With the continuous increase of cultivated land, it is bound to occupy the land area of other land use types. Forest land showed a trend of decreasing first and then increasing and forest land in 2004-2014. The speed of the land area has slowed down, and the average annual reduction rate has changed from 1.39% in 2004-2009 to 0.31% in 2009-2014. This is mainly due to the implementation of the local policy of returning farmland to forestry. The area of forest land has begun to reverse in 2014-2019, and the area of forest land has increased. However, from the quantitative point of view, the area of forest land in 2004-2019 is still decreasing. Grassland area showed a drastic decreasing trend, the area of grassland reduction in 2014-2019 even exceeded the total area of grassland reduction in 2004-2009 and 2009-2014, and the dynamic degree of land in 2014-2019 was -1.95. Construction land showed a strong growth trend, the dynamic degree of construction land in 2014-2019 reached 5.36, which shows the change of construction land was very active. The change in water area is not obvious.

References

Bai J. and S. Li (2013). Land use and sandy desertification in Northern China. West China Development 2013-02-08(8).

Chen L. (1996). Combating of land desertification in China. Journal of Natural Disasters, 5(1), 105-111.

Duan Z., F. Zhang and X. Kong X (2005). Method for information mining of land-use change and its application, Transactions of the CSAE 2005(12), 60-66.

Fang F., X. Liang and C. Li (2014). Review of spatial multi-criteria decision making. Science of Surveying and Mapping 39(07), 9-12.

Gao Z. and X. Zhao (2002). Prediction of land use variation change based on GIS, Journal of Capital Normal University (Natural Science Edition) 2002(02), 75-80.

Ge X., X. Ming and Q. Ye (2010). Land use and sandy desertification around surface water in Horqin sandy land: A case study in Naiman Banner, Journal of Desert Research 30(05), 1012-1018.

Guan D. and Weijun (2008). Land use change of Kitakyushu based on landscape ecology and Markov model, Acta Geographica Sinica 18(4), 455-468.

Guo X., L. Chen and B. Fu (1999). Effects of land use/land cover changes on regional ecological environment, Advances in Env Ironmenta l Science 7(6), 66-75.

Halmy M., P. Gessler and J. Hicke (2015). Land use/land cover change detection and prediction in the north-western coastal desert of Egypt using Markov-CA. Applied Geography, 63.

Li Z., G. Song and S. Lu (2017). Change and prediction of the land use in Harbin City based on CA-Markov Model, Chinese Journal of Agricultural Resources and Regional Planning 38(12), 41-48.

Liu G. and X. He (2003). Geographic Information System Practice Course [M], Tsinghua University Press.

Liu S., X. Yu and Q. Li (2010). Land use change in loess hilly region based on CA-Markov model. Transactions of the CSAE 26(11), 297-303.

Lv X., Y. Wang and Y. Zhang (2007). Analysis of land use change and its desertification response in the central Ningxia Hui Autonomous Region: A case study of Yanchi County. Geographical Research 2007(06), 1156-1164.

Mondal M., N. Sharma and P. Garg (2016). Statistical independence test and validation of CA Markov land use land cover (LULC) prediction results, The Egyptian Journal of Remote Sensing and Space Sciences 19(2).

National People's Congress Standing Committee (1998). Land administration law of the People's Republic of China.1998-08-29.https://www.cecc.gov/resources/legal-provisions/land-administration-law-of-the-peoples-republic-of-china-0.

Wang B. and L. Zang (2006). Recent progress of studies on land use and land cover change in China, Areal Research and Development 25(2), 86-91.

Wang L., X. Zhang and S. Zhang (2010). Response of sandy desertification to land use change in the west of Songnen Plain: A case study in Tailai County. Geographical Research 29(03), 449-459.

Wang T. and W. Wu (1999). Landuse and sandy desertification in Northern China, Journal of Natural Resources 14(4), 355-358.

Wu J., Y. Tian and W. Xu (2017). Scenario analysis of land use change in the lower reaches of Wujiang river based on CA-Markov Model, Research of Soil and Water Conservation 24(04), 133-139.

Xie Z., X. Xu and Q. Sun (2008). Prediction of land cover change based on the patch-dynamics model: A case study of Beijing, Acta Scientiarum Naturalium Universitatis Pekinensis, 2008(03), 452-458.

Xu D., X. Kang and Z. Liu (2009). Climate change and human activities in the ordos area desertification a study of the relative roles in the process. Science in China Press, 39(4), 516-528.

Xu J. (2007). Desertification is a human nightmare. Forestry of China 2007(13)33.

Xu X., H. Liu and Z. Lin (2017). The Advances and problems of land use and land cover change research in China, Research of Soil and Water Conservation 24(1), 213-218.

Yu X. and G. Yang (2002). The advances and problems of land use and land cover change research in China. Progress In Geography 21(1), 51-57.

Yu X., G. Yang and Y. Wang (2004). Advances in researches on environmental effects of land use/cover change, Scientia Geographica Sinica 24(5), 627-633.

Zhang J., Chang X. and Cai M. (2009). Effects of Land Use on Desertification in Typical Regions in the Horqin Sandy Land. Arid Zone Research 26(01). pp. 39-44.

Zhou C. and H. Li (2012). The research summary of land use with the model of cellular automata, Geomatics World, 10(05), 6-10.

Zhou C., Z. Sun and Y. Xie (2003). Research on Geographic Cellular Automata. Science Press.

Zhou Q., S. Wei-Ci and S. Chen (2010). LUCC analysis of Tong Liang county based on the landscape pattern indices and the Markov Model, Resources & Environment in the Yangtze Basin 19(7), 770-775.

Journal of Geomatics Vol. 14, No. 1, April 2020

Assessment of seasonal variation of ground water quality in the northern arcuate of Mizoram, India using geo-spatial technology

F. Lalbiakmawia[1]*, V.K. Bharati[2] and Shiva Kumar[3]
[1]Department of Geology, Mizoram University/ Assistant Hydrogeologist, PHE Department, Mizoram 796001, India
[3]Department of Geology, Mizoram University, Mizoram 796004, India
[2]Department of Chemistry, Govt. Kolasib College, Mizoram 796081, India
* Email: fbm.geo@gmail.com

(Received: June 28, 2019; in final form: May 15, 2020)

Abstract: Water is one of the most important natural resources, which is extremely vital for our daily life. Ground water is the main source of water for irrigation, industrial and also for domestic purposes in India. Therefore, the quality of ground water is as important as its availability. Inconsistent ground water quality during different seasons may hamper agricultural and industrial products and also the wellbeing of the people. The northern part of Mizoram has become an important commercial hub resulting in rapid urbanization and growth of human and livestock population. The present study utilizes geo-spatial technology to map the spatial variability of ground water quality in various seasons. Ground water samples were collected from 50 point sources in season-wise i.e. pre-monsoon, monsoon and post monsoon seasons for three consecutive years i.e., 2016, 2017 and 2018 from the northern arcuate of Mizoram. All the samples were analyzed in the laboratory based on important ground water quality parameters. The major water quality parameters namely pH, Total Dissolved Solids (TDS), Electrical Conductivity (EC), Iron, Total hardness, Alkalinity and Nitrate have been estimated and the averaged seasonal values of three years were taken for all the sampling locations. Interpolation technique called Inverse Distance Weighted (IWD) method was utilized for generating spatial variation maps of ground water quality parameters for different seasons. These seasonal and spatial variation maps of ground water quality within the study area can be utilized to give a guideline for the suitability of ground water uses and database for further developmental activities in water sector.

Keywords: GIS, Ground water, Water quality, Mizoram.

1. Introduction

Rapid urbanization, growth of population and extensive uses in domestic and agricultural sectors increase the demand for good quality of water supply (Choudhary et al., 1996; Majumder and Sivaramakrishnan, 2014; Goyal, 2013). Ground water is one of the most important natural resources and the major accessible source of fresh water (Neelakantan and Yuvaraj, 2012; Kumar, 2013; Nag and Das, 2014). However, urbanization and the unregulated growth of the population have altered the local topography and drainage system which affect both quality and quantity of the ground water (Vasanthavigar et al., 2010). Therefore, finding the potential areas, monitoring and conserving ground water have become highly crucial at the present moment (Rokade et al., 2004; Kumar and Kumar, 2011).

The geology of Mizoram comprises N-S trending ridges with high degree of slopes and narrow intervening synclinal valleys. Faulting in many locations has produced steep fault scarps (GSI, 2011). Therefore, majority of the rain water is lost as surface runoff even though the state received high amount of rainfall. Springs are the major sources of water in the area. Hence, the quality of water from such sources needs to be carefully analyzed and represented in a GIS environment (CGWB, 2007). Few efforts were made in studying the water quality within the state of Mizoram. These include seasonal variation in water quality of Tuirial river in vicinity of the hydel project (Lalparmawii and Mishra, 2012), Physico-chemical characteristics of Tamdil lake (Mishra and Chenkual, 2014) and Ground water quality mapping of Aizawl district (Lalbiakmawia and Vanthangliana, 2015).

The arrival of geospatial technology allows fast and cost effective survey and management for natural resources (Ramakrishna et al., 2013). Geographical Information System (GIS), Global Positioning System (GPS) and remote sensing are the main tools in this recently introduced technology. Hence, this technique has wide-range applications in geo-scientific researches including ground water quality mapping (Ganesh Babu and Sashi kumar, 2013). Therefore, many researchers have utilized these techniques successfully in ground water studies, both for prospecting and quality mapping (Krishnamurthy and Srinivas, 1995; Krishnamurthy et al., 2000, Dey, 2014). These techniques have proved to be of immense value not only in the field of hydrogeology but also for the development of surface water resource as well (Sharma and Kujur, 2012; Saraf and Choudhury, 1998).

2. Study area

2.1 Location and extent

The study area (Figure 1) lies in the northern arcuate of the state between 92° 31' 39.80"E to 92° 53' 45"E and the 24° 08' 38.00"N to 24° 31' 16.00" N, which is situated in northern part of Kolasib district and falls under Survey of India topographical map No. 83D/11, 83D/12, 83D/14 and 83D/15 covering 395 sq km. The area is bounded in the west by Mamit district, in the north by Hailakandi district and Cachar district of Assam and in the eastern side, it is bounded by Aizawl district of Mizoram. It falls under N. Thingdawl rural development block and there is one notified town i.e. Vairengte and about 20 other habitation.

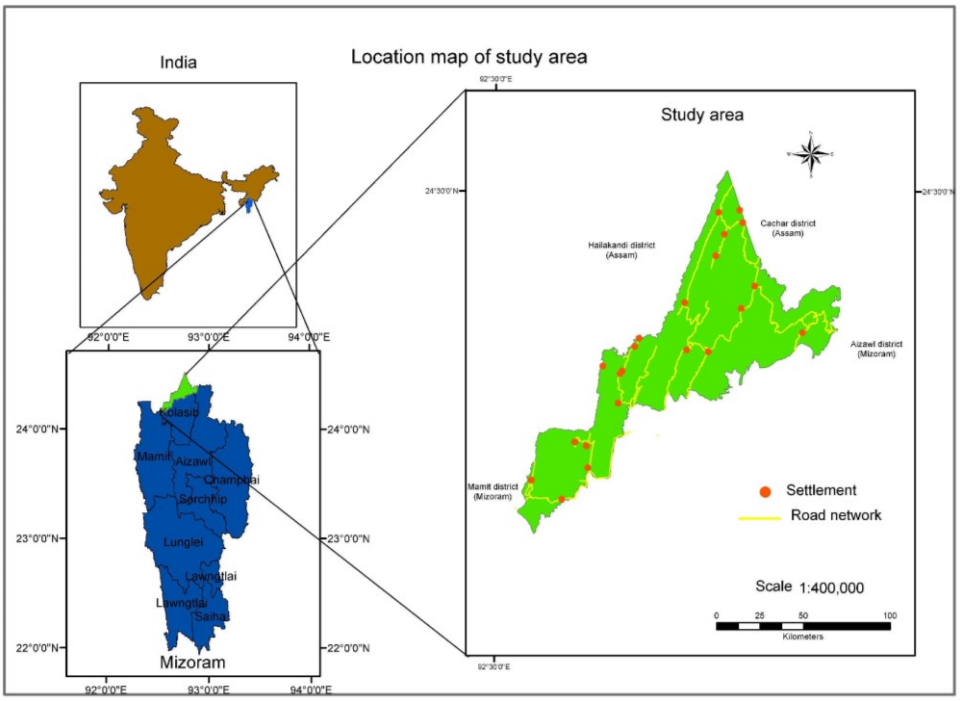

Figure 1: Location map of the study area

The area is bounded in the west by Mamit district, in the north by Hailakandi district and Cachar district of Assam and in the eastern side, it is bounded by Aizawl district of Mizoram. It falls under N. Thingdawl rural development block and there is one notified town i.e. Vairengte and about 20 other habitations.

2.2 Climatic condition

The climate of the study area ranges from moist tropical to moist sub-tropical. The entire area is under the direct influence of south west monsoon, with average annual rainfall of 2287.10 mm (Lalzarliana, 2018). Figure 2 shows the average annual rainfall and table 1 provides annual rainfall of the study area during 2008-2017.

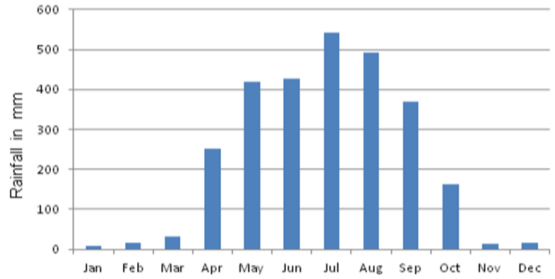

Figure 2: Average annual rainfall of the study area

Table 1: Annual rainfall of the study area during 2008-2017

Bilkhawthlir, Kolasib district Rainfall (in mm) 2008-2017												
Year	Jan	Feb	March	April	May	June	July	Aug	Sept	Oct	Nov	Dec
2008	19	12	0	32	87	294	297	500	122	194	0	0
2009	0	18	52	142	200.8	325	313	383	196	0	14	0
2010	0	0	104	459	624	730	1111	1033	783	162	0	142
2011	0	0	78	83	657	726	1139	742	379	317	0	0
2012	50	18	0	867	369	558	282	480.4	373	315	8.2	0
2013	0	0	7	107	1085	330.6	698.8	319.9	292.3	119.9	0	0
2014	0	6.4	21.9	55.5	161.6	210	380.5	165.4	289.6	165.4	3.1	0
2015	10.6	19.2	11	397.7	390.3	356.8	468.4	361.2	242.4	361.2	22.5	11.4
2016	0	48	55.8	181	318	304.1	221.5	262.8	320.5	87.9	66.4	0
2017	0	1.9	166.6	358.9	263.5	411.4	385.6	525.5	256.7	243.2	0	103.1
Average	7.96	12.4	49.6	268	416	425	530	477	325	197	11.4	25.7

2.3 Geology

The earliest recorded work on geology of Mizoram reported that the area comprises great flysch facies of rocks made up of monotonous sequences of shale and sandstone (La Touche THD, 1891). The study area lies over rocks of Middle Bhuban, Upper Bhuban and Bokabil formations of Surma Group of Tertiary age. Middle Bhuban and Bokabil formations consist mainly of argillaceous rocks while Upper Bhuban formation comprises mainly of arenaceous rocks (GSI, 2011). It was also observed that the rocks exposed within the study area were traversed by several faults and fractures of varying magnitude and length (MIRSAC, 2007).

2.4 Geomorphology

The study area is characterized mainly by ridgelines and intervening valleys and less prominent ridges. Structural hills are the main geomorphic units which are classified as High, Moderate and Low Structural Hills based on their elevation. As the name implies, structural hills are of structural origin, associated with folding, faulting and other tectonic processes. Other geomorphic units like Valley Fill and Flood Plain are characterized by unconsolidated sediments, and occur along streams and major rivers respectively (Lalbiakmawia, 2015).

Geology, geomorphology and demographic profile can be utilized for analyzing the spatial variability in the water quality constituents. Nutrients from domestic waste or from agricultural pesticides add to the complexity of the research.

3 Materials

3.1 Data

Base map of the study area comprising roads, settlement and boundary were extracted from Natural Resources

Atlas of Mizoram prepared by MIRSAC. Satellite data, SOI topographical maps and various ancillary data were also referred in the study. Records of ground water quality prepared by State Referral Institute (SRI), Aizawl were imported and plotted in a GIS environment.

3.2 Software

GIS software ArcInfo 10.1 version and handheld GPS device were used for analysis, mapping, locating sample points and for ground truth verification.

4 Methodology

The base map was geo-referenced and digitized using ArcInfo 10.1 GIS software for spatial analysis. The water samples were collected from fifty locations which area within or near the settlement and covered the entire area uniformly (Figure 3). Hence, all the samples were collected from Built-Up areas in terms of Land use/land cover. Majority of the samples were collected from dug wells and springs, few tube wells were also included. Water samples were collected in a wide mouth bottle (Tarsons bottle), washed with distilled water and again rinsed with representative water samples. These are then transported to the laboratory at least within 24 hours for analysis. Pre-monsoon, monsoon and Post monsoon data were collected each year from 2016-2018. Pre-monsoon samples were taken during the month of March and April, monsoon data during July and August and post monsoon samples during October and November. The samples were tested for their physico-chemical parameters in State Referral Institute (SRI), Aizawl. Digital instruments made by Eutech instruments were used to test pH, Electrical Total Dissolved Solids (TDS), Conductivity (EC), Iron, Alkalinity, Total hardness and Nitrate were measured using the water testing kit made by Transchem Agritech Limited (Blick, 2018). The characteristics of the water were subsequently evaluated using the Indian Drinking Water Standards as per BIS Guideline (RGNDWM, 2011).

Interpolation technique through Inverse Distance Weighted (IDW) approach has been used in the present study for generating element-wise seasonal and spatial distribution of the ground water quality. This technique is one of the most commonly used techniques for interpolation of scatter points and has been used extensively in ground water quality mapping. The method is based on the assumption that the interpolating surface should be influenced most by the nearby points and less by the more distant points. (Ambica et al., 2017; Khadri and Pande, 2015; Mahalingam et al, 2014; Boominathan et al., 2015; Shyamala and Jeyanthi, 2017; Lalbiakmawia, 2015). Variation maps were utilized for comparing the ground water quality parameters through space and time.

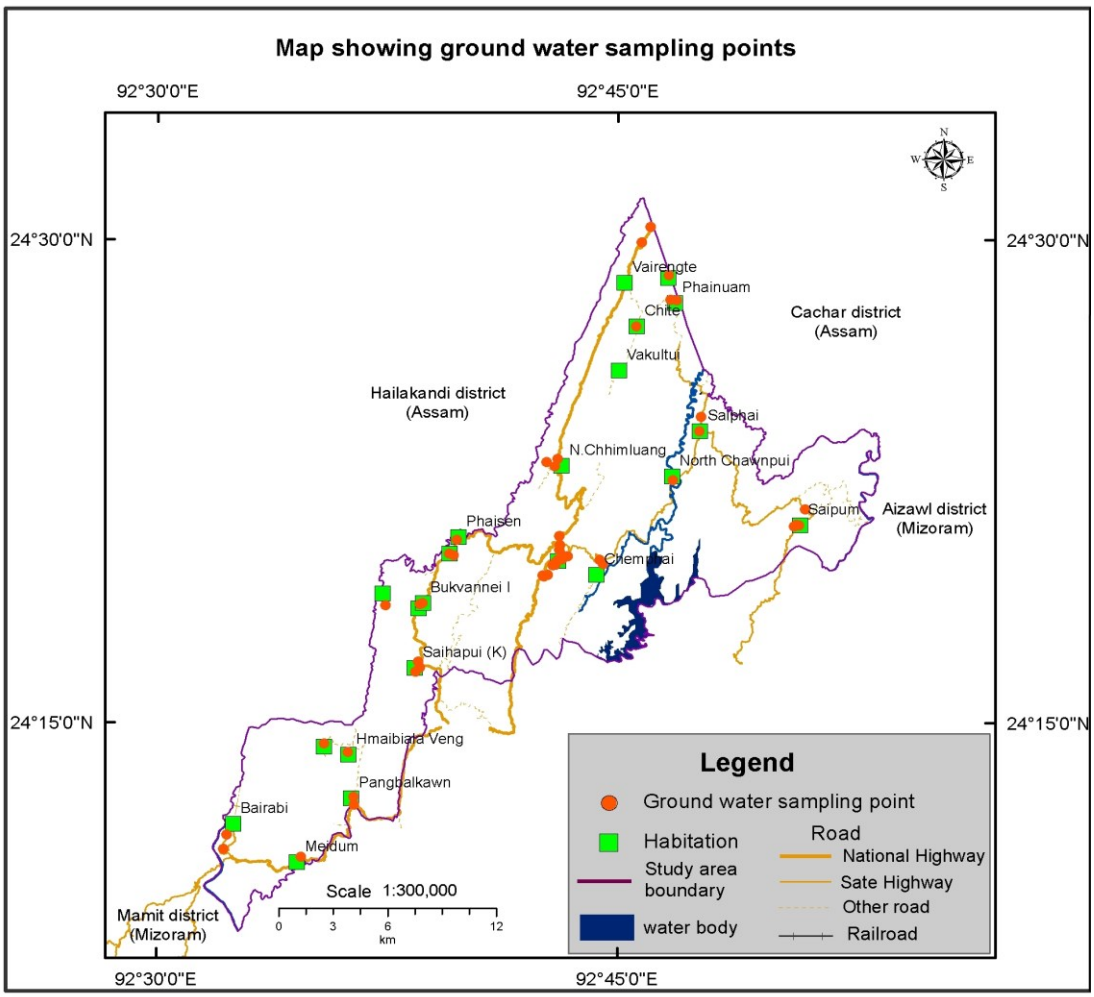

Figure 3: Map showing ground water sampling points

5 Results and Discussion

Seasonal and spatial ground water quality are integrated and presented in the form of maps. Results and discussion for the major parameters are as follows:

5.1 pH

pH is one of the important parameters of water which determines the acidic and alkaline nature of water. The pH value of water ranged between 6 and 8.5. The permissible range according to BIS is 6.5 to 8.5, hence, samples in some areas are acidic. Table 2 shows the average pH values and the spatial variation maps for pH are presented in the figure 4.

It was observed that the value of pH is lower during the monsoon period than the pre monsoon and post monsoon seasons especially in the eastern part of the study area. Since, jhum system of cultivation is still prevalent within and surroundings of the study area, burning of jhums right before the monsoon period may release huge volume of carbon dioxide into the atmosphere (Laldintluanga et al., 2016). When the monsoon starts, the carbon dioxide in the air may get dissolved within the rain and forms carbonic acid. When this precipitation reaches the ground surface, it act as a source of water to the spring.

Rainfall during the monsoon period also dissolve certain minerals in the sedimentary rocks like sandstone and shale which may cause lower pH value of water.

Table 2: Average pH value

Average pH Value			
Year	Pre-monsoon	Monsoon	Post monsoon
2016	6.90	6.87	7.27
2017	6.966	6.67	6.709
2018	7.14	6.66	7.46
Average	**7**	**6.74**	**7.15**

5.2 Total Dissolved Solids (TDS)

The Total Dissolved Solids (TDS) of water is classified in to three ranges (0-500 mg/l, 500-2000 mg/l and >2000 mg/l) by BIS guideline. Table 3 shows average TDS values and the spatial variation maps for TDS are presented in the figure 5. Total Dissolved Solids (TDS) usually refers to the mineral content of water. The most common source of dissolved solids in water is from the weathering of rocks which occurs more or less at the same rate within the study area. The concentration of TDS is controlled by the composition of the rocks and geomorphological condition of the area. It was also observed that the value of TDS is lower during the monsoon season than the pre monsoon and post that during monsoon periods. This may be due to increases of the solvent mainly rainwater during the monsoon. Accordingly, TDS value is much higher during pre-monsoon season due to decreasing amount of water during the dry period.

Table 3: Average TDS

Average TDS			
Year	Pre-monsoon	Monsoon	Post monsoon
2016	53.10	66.76	89.92
2017	61.74	74.20	59.20
2018	75.02	76.00	77.82
Average	**63**	**72.32**	**75.65**

5.3 Electrical Conductivity (EC)

The Electrical Conductivity (EC) of water was classified in to three ranges (0-2250 µmhos/cm, 2250-3000 µmhos/cm and >3000 µmhos/cm) by BIS guideline. Table 4 shows the average EC values and the spatial variation maps for Electrical Conductivity (EC) are presented in the figure 6. Electrical conductivity in ground water varies slightly in season-wise with the highest value during pre-monsoon especially in the eastern part and the lowest conductivity during monsoon period. Increase in the amount of aqueous solution during rainy season may have reduced the conductivity. The temperature of water while measuring the Electrical conductivity ranges from 25°-28°C.

Table 4: Average EC value

Average EC			
Year	Pre-monsoon	Monsoon	Post monsoon
2016	205.00	164.00	180.00
2017	220.00	170.00	185.00
2018	210.00	190.00	200.00
Average	212	174.67	188.33

5.4 Iron (Fe)

As per BIS guideline, in terms of Iron concentration, <0.3mg/l is Desirable limit, 0.3-1.0mg/l is Permissible limit and >1.0mg/l is in Non-potable class. Fe content in ground water depends on the chemical composition of the aquifers and may largely due to the hand pump components in a bore well. Table 5 shows average Fe concentration values and the spatial variation maps for Iron are presented in the figure 7. Season-wise, iron content is lowest during the monsoon period, while the pre-monsoon season has the highest iron concentration. Increasing amount of water during monsoon may have diluted the iron concentration while the amount of water is less during pre-monsoon causing higher concentration of iron.

Table 5: Average Fe concentration

Average Fe concentration			
Year	Pre-monsoon	Monsoon	Post monsoon
2016	0.41	0.34	0.28
2017	0.30	0.16	0.15
2018	0.23	0.13	0.18
Average	0.31	0.21	0.20

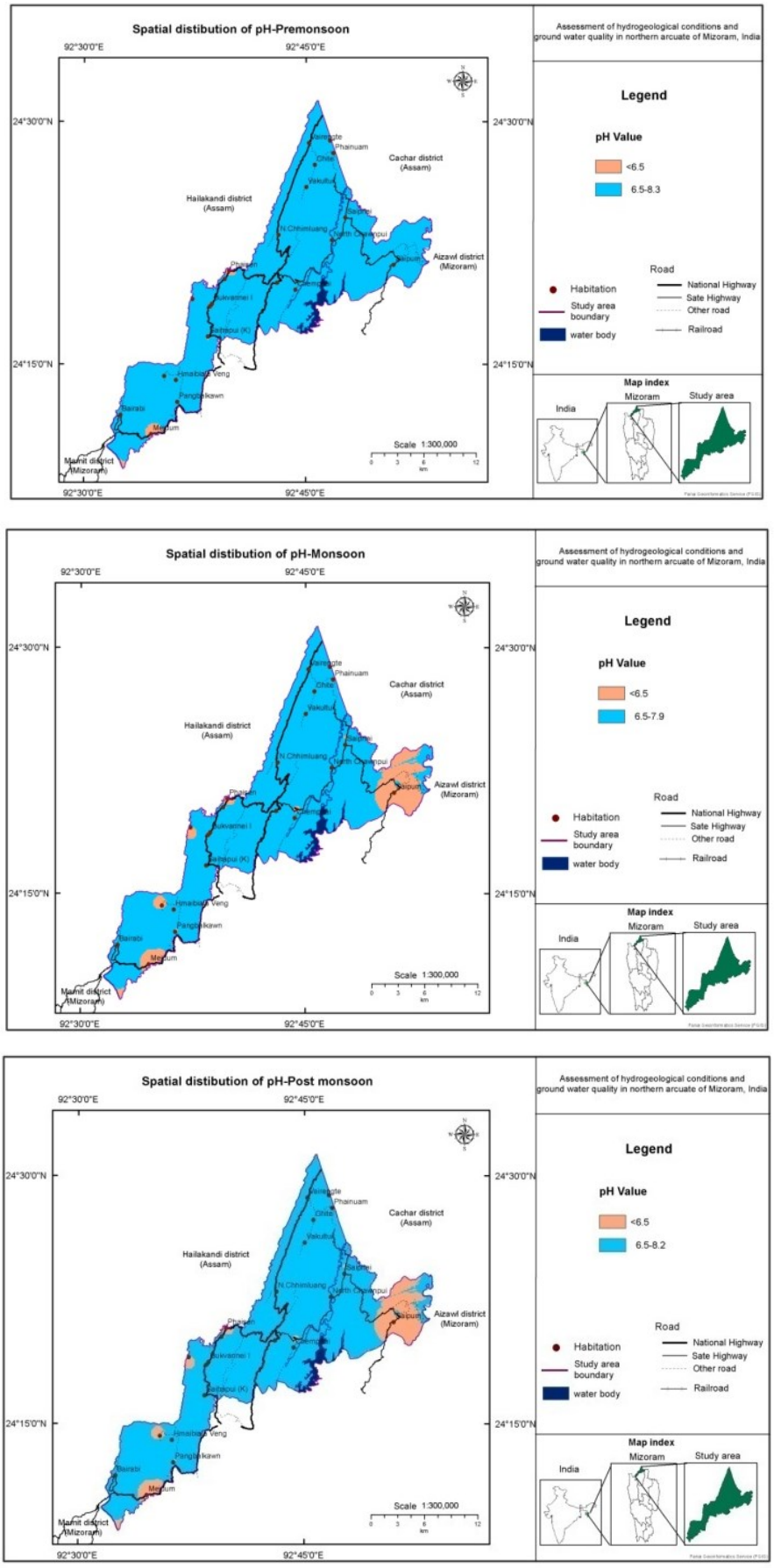

Figure 4: Spatial distribution of pH during pre-monsoon, monsoon and post monsoon season

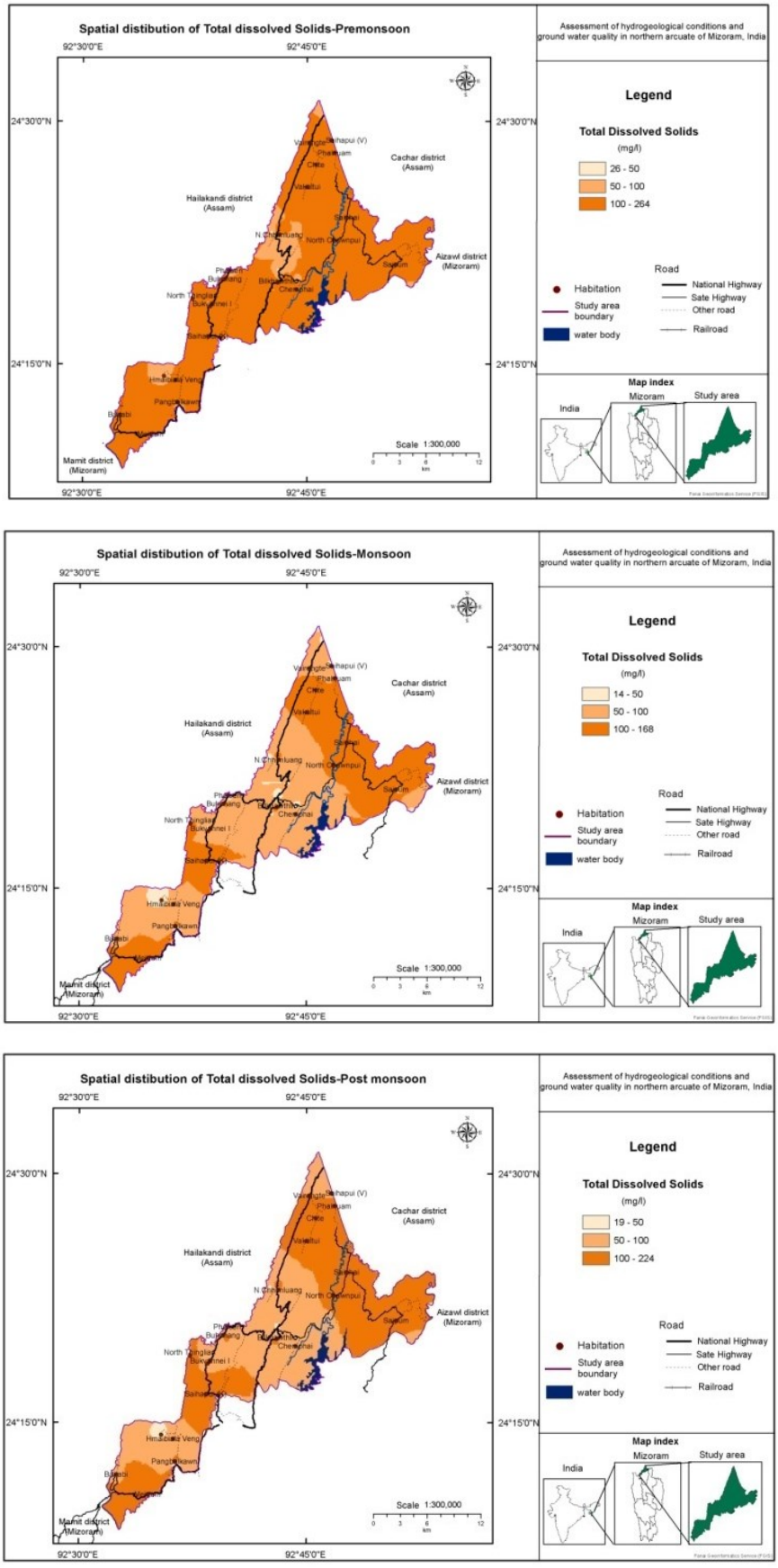

Figure 5: Spatial distribution of Total Dissolved Solids during pre-monsoon, monsoon and post monsoon season

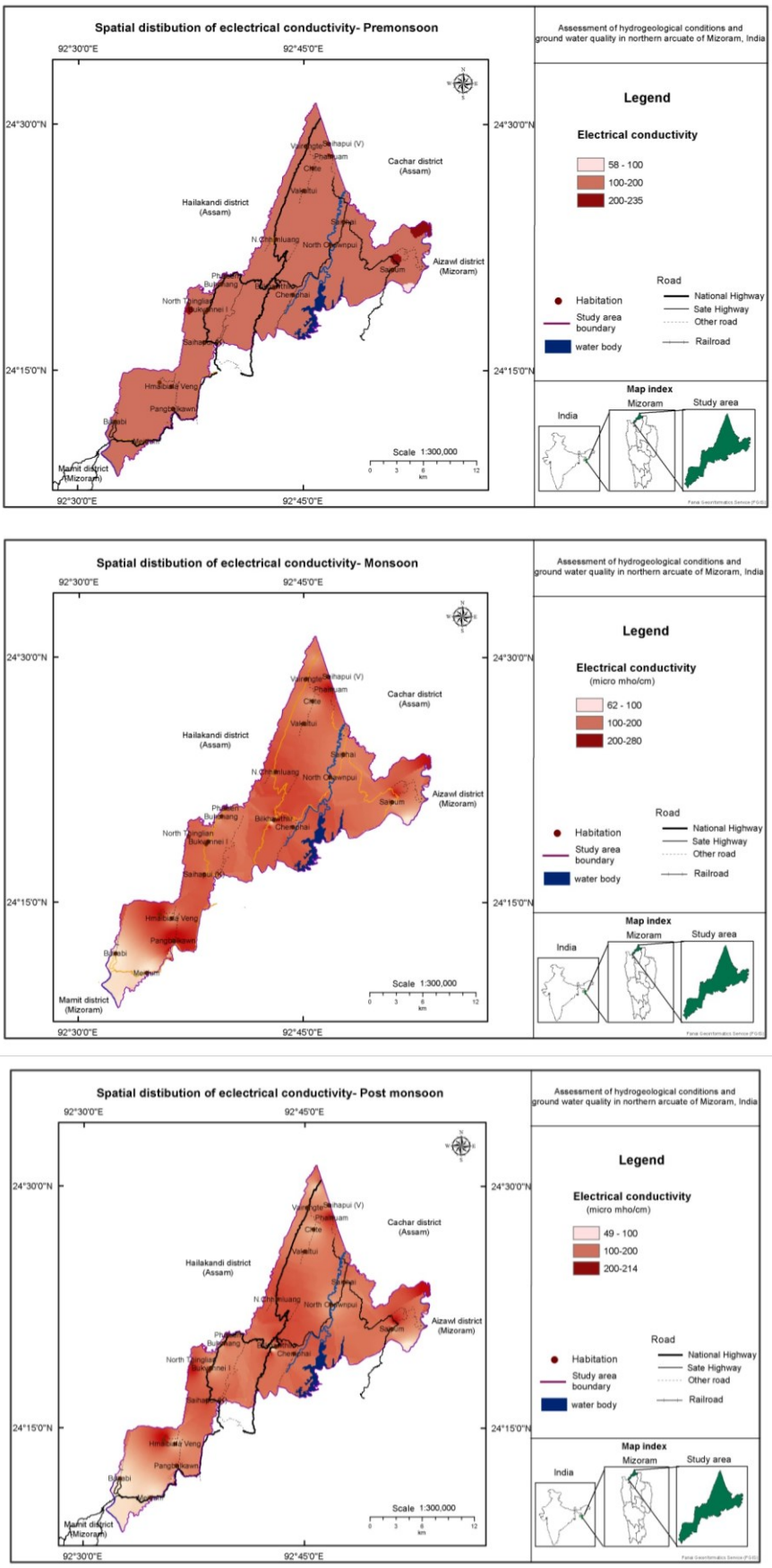

Figure 6: Spatial distribution of Electrical conductivity during pre-monsoon, monsoon and post monsoon season

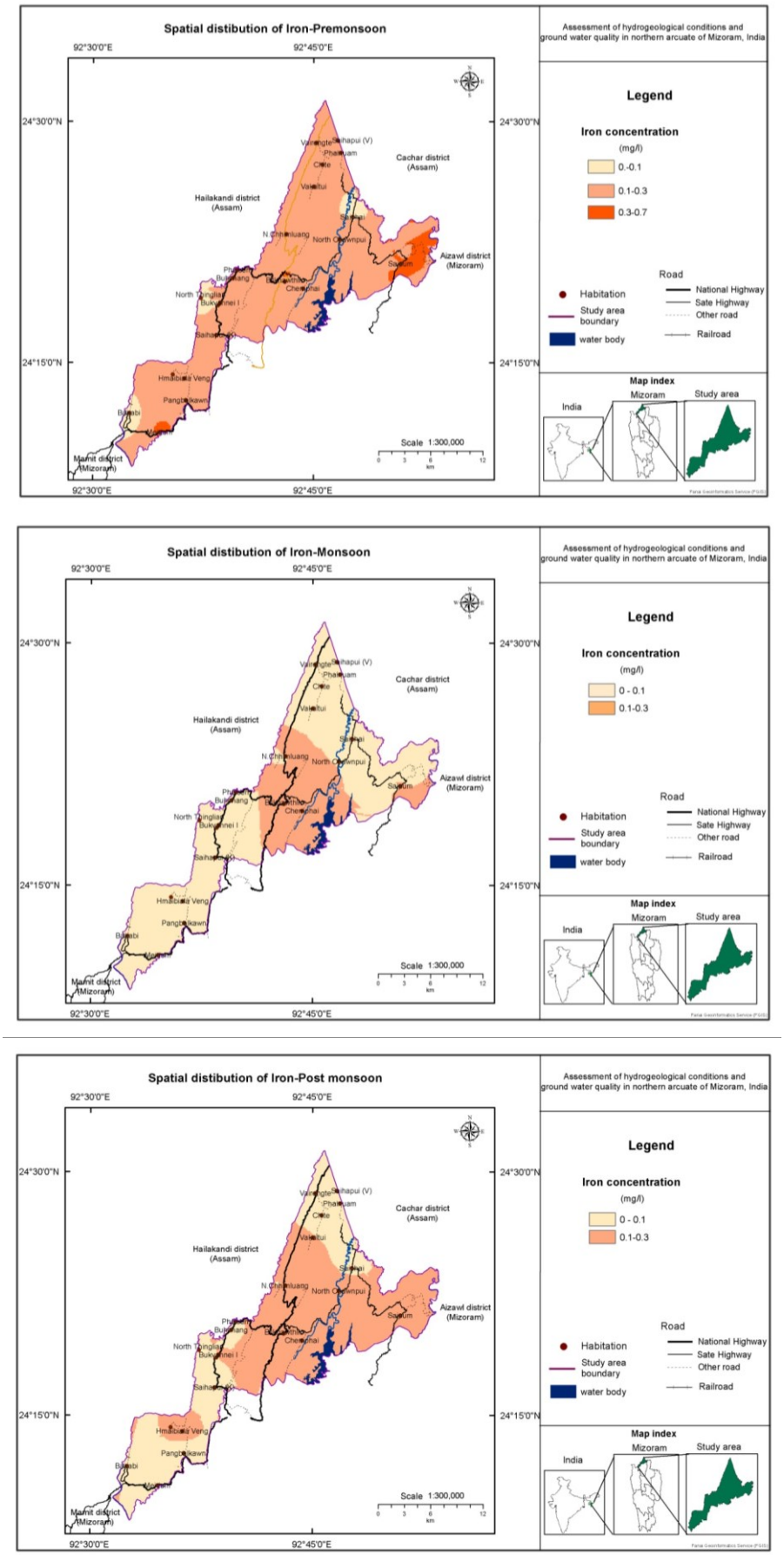

Figure 7: Spatial distribution of Iron during pre-monsoon, monsoon and post monsoon season

5.5 Total Alkalinity

The total alkalinity is categorized into three ranges (0-200 mg/l, 200-600 mg/l and >600 mg/l) by BIS guideline. Water with high alkalinity is said to be "hard." The most prevalent mineral compound causing alkalinity is calcium carbonate. Large amount of alkalinity imparts a bitter taste to water. However, in terms of Total alkalinity, all the samples from different sources within the study area are well within desirable limit. Table 6 shows average total alkalinity values and the spatial variation maps for Alkalinity are presented in the figure 8. The total alkalinity is lower during the monsoon season than the pre-monsoon and post monsoon periods. This may be due to the increase of amount of water and may also be due to slightly acidic nature of the rain water during the monsoon period.

Table 6: Average Alkalinity

Average Alkalinity			
Year	Pre-monsoon	Monsoon	Post monsoon
2016	68.30	64.85	70.70
2017	76.08	66.00	64.98
2018	78.00	68.00	72.00
Average	74.13	66.28	69.23

5.6 Total Hardness

The Total hardness is categorized in to three ranges (0-300 mg/l, 300-600 mg/l and >600 mg/l) as Desirable, Permissible and Non-potable classes by BIS guideline. The value of Total hardness in ground water may be controlled by the chemical composition of the aquifers. Hardness is the amount of dissolved calcium and magnesium in the water. Table 7 shows average total hardness values and the spatial variation maps for total hardness are presented in the figure 9. The highest total hardness value is 295mg/l. That means the quality of ground water in terms of total hardness within the study area is within Desirable class.

Total hardness is lower during the monsoon season than the pre-monsoon and post monsoon periods and slightly higher in Post monsoon and with the highest concentration during the Pre-monsoon period.

Table 7: Total Hardness

Average TH			
Year	Pre-monsoon	Monsoon	Post monsoon
2016	53.34	43.56	51.18
2017	70.66	60.58	61.42
2018	76.08	56.54	60.22
Average	66.69	53.56	57.61

5.7 Nitrates

Nitrates concentration was classified in to three ranges (<45 mg/l, 45-100 mg/l and >100 mg/l) by BIS guideline. Table 8 shows average nitrate concentration values and the spatial variation maps for nitrates are presented in the figure 10. Ground water from various locations of the study area is well within the Desirable class as per BIS classification.

The contamination of ground water by nitrates may also be due to anthropogenic activities like utilization of fertilizers, sewage from human habitations. Concentration of Nitrates in ground water may depend on the chemical composition of the rocks in which it occurs. Nitrate concentration is higher during the pre-monsoon season than the monsoon and post monsoon periods. This may be due to the increasing quantity of water during the rainy season where the element concentration got diluted. The monsoon period and post monsoon period have almost the same Nitrates concentration.

Table 8: Average Nitrate Concentration

Average Nitrates concentration			
Year	Pre-monsoon	Monsoon	Post monsoon
2016	53.34	43.56	51.18
2017	70.66	60.58	61.42
2018	76.08	56.54	60.22
Average	66.69	53.56	57.61

6. Conclusion

It can be concluded from the present study that the northern arcuate of Mizoram has no major problem in ground water quality in any of the seasons i.e. pre-monsoon, monsoon and post monsoon.

The eastern part of the area has lower pH value, higher concentration of Fe and higher EC as compared to the other parts. Value of Total Alkalinity is higher within the middle part of the area. Total Hardness and concentration of Nitrates are more or less equal within the study area. The difference in elements concentration may be due to geological variation within the study area.

There are seasonal variations in element-wise ground water quality of the area. The seasonal variation is mainly due to the amount of rainfall or absence of it. Undiluted rainwater seems to have a huge effect on the ground water quality.

The Ground water quality maps help us to know the existing ground water condition of the study area. Geo-spatial technology has been proven to be useful tools for mapping ground water quality. The ground water quality map prepared through this study will be useful for planning future ground water development and management.

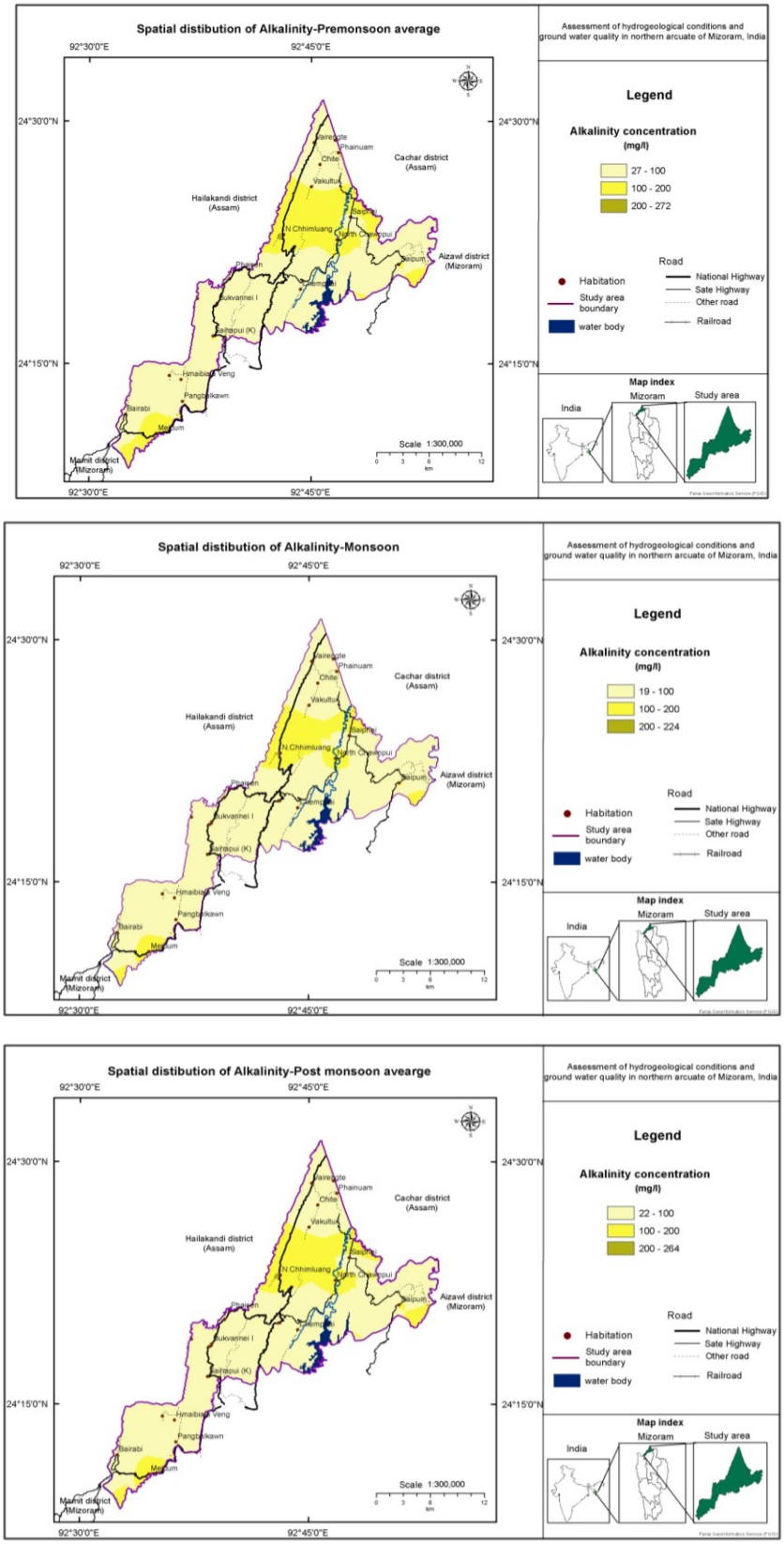

Figure 8: Spatial distribution of Alkalinity during pre-monsoon, monsoon and post monsoon season

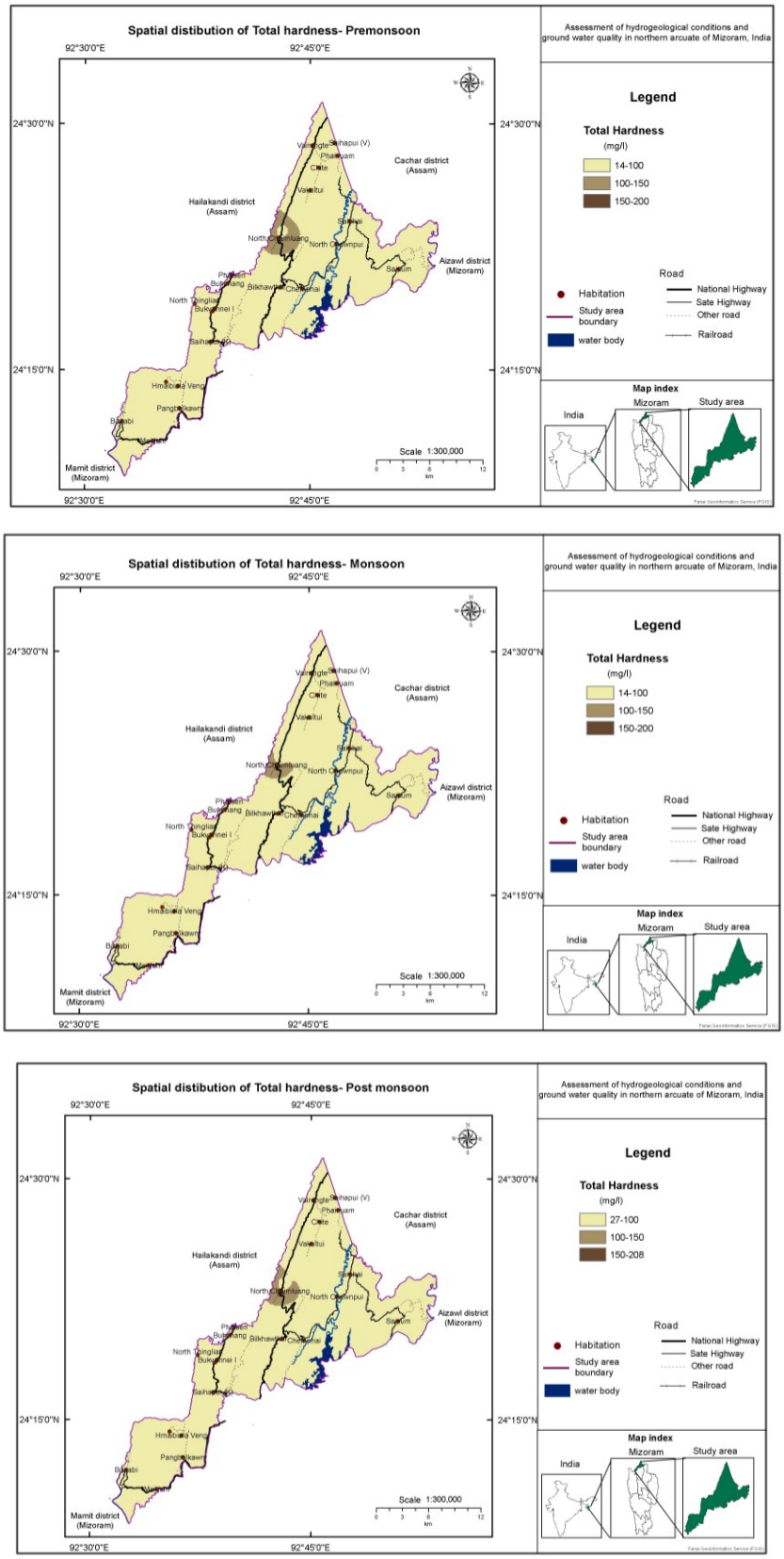

Figure 9: Spatial distribution of Total hardness during pre-monsoon, monsoon and post monsoon season

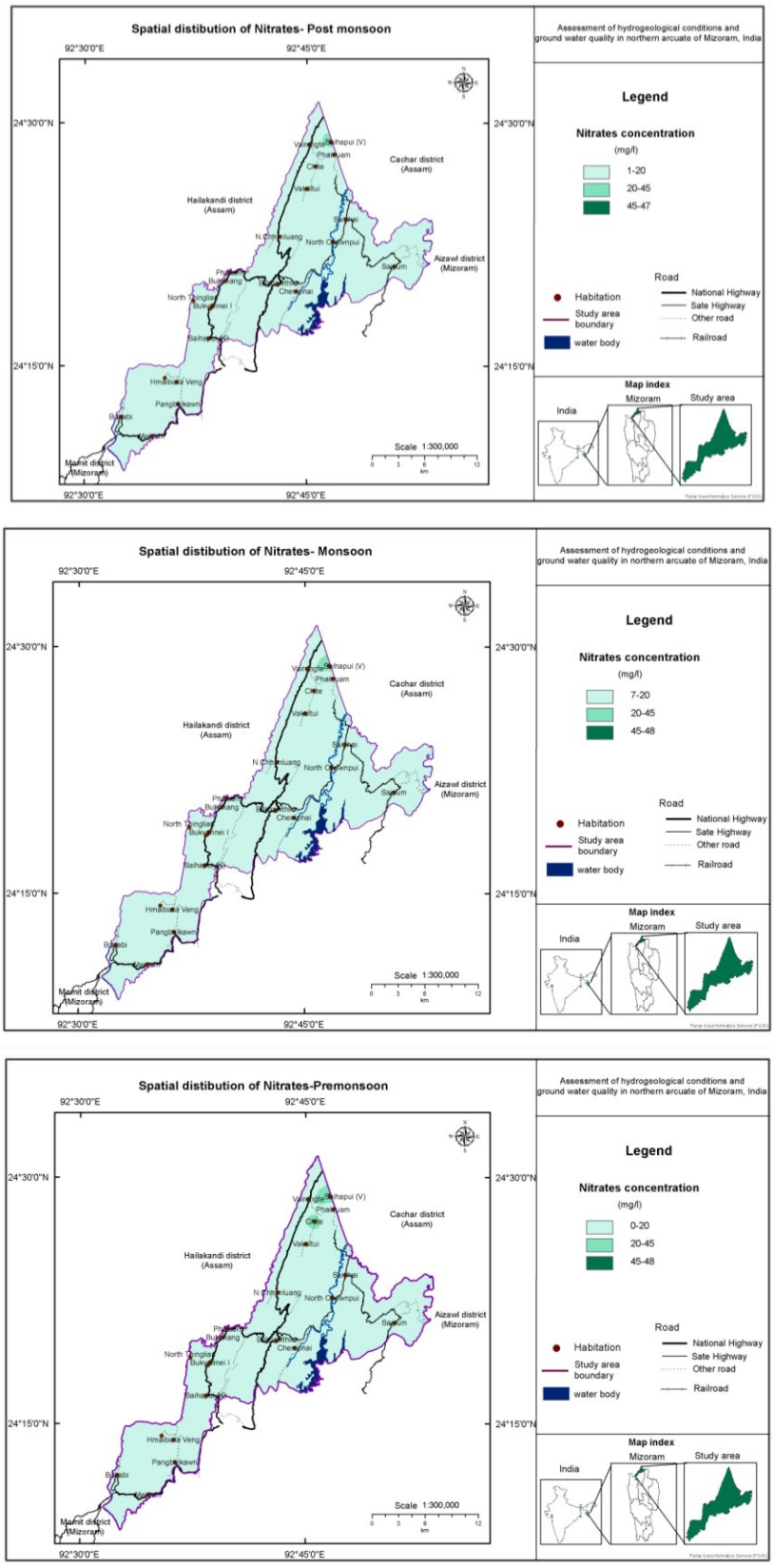

Figure 10: Spatial distribution of Nitrates during pre-monsoon, monsoon and post monsoon season

Acknowledgements

The author is thankful to Mr. R. Lalruatkima, Hydrogeologist, and E-in-C, PHE Department, Mizoram for his support.

References

Ambica, A., B. Sartiha, and R. Anbarasan (2017). Groundwater quality assessment using water quality index and GIS, Maduravoyal, Chennai, India. International Journal of Civil Engineering and Technology, 8(8), 1375–1381.

Blick, J. (2018). Assessment of drinking water quality in Kamalanagar, Lawngtlai district, Mizoram. Advances in Engineering Research, 178.

Boominathan, S.D., S. Palanisamy, S. Kanagaraj and G. Munusamy (2015). Mapping of ground water quality for Ramanathapuram Taluk of Tamil Nadu using Geographical Information System. International Journal of Advanced Remote Sensing and GIS, 4(1), 953-959.

CGWB (2007). Manual on Artificial Recharge of Ground Water. Central Ground Water Board, Ministry of Water Resources, 13.

Choudhary, B.S., Manoj Kumar, A.K. Roy and D.S. Ruhal (1996). Application of remote sensing and Geographic Information Systems in ground water investigations in Sohna block, Gurgaon district, Haryana (India). International Archive of Photogrammetry and remote Sensing, XXXI (B6), 21.

Ganesh Babu, O. and M.C. Sashi Kumar (2013). Application of GIS for ground water quality mapping of Tiruppur block, Tamil Nadu. International Journal of Remote Sensing & Geoscience, 2(5), 18-25.

Goyal, S.K. (2013). Temporal and seasonal changes in groundwater quality in an agriculture dominated area. International Journal of Advancement in Remote Sensing, GIS and Geography. 1(2), 39.

GSI (2011). Geology and Mineral resources of Manipur, Mizoram, Nagaland and Tripura. Geological Survey of India, Miscellaneous Publication No. 30 Part IV, 1(2), 36-39.

Khadri, S.F.R and C.B. Pande (2015). Ground water quality mapping for Mahesh river basin in Akola and Buldhana districts of Maharashtra, India using interpolation methods. International Journal on Recent and Innovation Trends in Computing and Communication. 3(2), 113 – 117.

Krishnamurthy, J., A. Mani, V. Jayaraman, and M. Manivel (2000). Ground water resources development in hard rock terrain – an approach using remote sensing and GIS techniques. International Journal of Applied Earth Observation and Geoinformation, 2(34), 204-215.

Krishnamurthy, J. and G. Srinivas (1995). Role of geological and geomorphological factors in ground water exploration: A study using IRS-LISS-II data. International Journal of Remote Sensing, 16, 2595-2618.

Kumar, B. and U. Kumar (2011). Ground water recharge zonation mapping and modeling using Geomatics techniques. International Journal of Environmental Sciences 1 (7), 1671.

Kumar, C.P. (2013). Assessment and strategies for development potential of deeper confined aquifers in India. Asian Academic Research Journal of Multidisciplinary, 1(8), 1.

La Touche T.H.D (1891). Records of the Geological Survey of India. Geological Survey of India, 24(2).

Lalbiakmawia, F. (2015). Application of geo-spatial technology for ground water quality mapping of Mamit district, Mizoram, India. International Journal of Engineering Sciences & Management Research, 2(6), 31-38.

Lalbiakmawia, F. and V. Vanthangliana (2015). Application of geo-spatial technologies for ground water quality mapping of Aizawl district, Mizoram, India. Science Vision, 15(3), 115-123.

Laldintluanga, H., F. Lalbiakmawia, and R. Lalbiaknungi (2016). Assessment of rural water quality in Aizawl, Mamit and Serchhip district of Mizoram, India. International Journal of Science Technology & Engineering, 3(6), 111-118.

Lalparmawii, S. and B.P. Mishra (2012). Seasonal variation in water quality of Tuirial River in vicinity of the hydel project in Mizoram, India. Sci Vis 12(4), 159-163.

Lalzarliana, C. (2018). Rainfall records of Mizoram. Directorate of Agriculture, Government of Mizoram, 1.

Mahalingam, B., M.D., Ramu, Bhauso and P. Jayashree (2014). Assessment of groundwater quality using GIS techniques: A case study of Mysore city. International Journal of Engineering and Innovative Technology. 3(8), 117-122.

Majumder, A. and L. Sivaramakrishnan (2014). Ground water budgeting in alluvial Damodar fan delta: A study in semi-critical Pandua block of West Bengal, India. International Journal of Geology, Earth & Environmental Sciences, 4(3), 23-37.

Mishra, B.P. and Lalzahawmi Chenkual (2014). Physico-chemical characteristics of Tamdil in Mizoram, northeast India. Sci Vis, 14(4), 200-206.

MIRSAC (2007). Natural Resources Mapping of Kolasib district, Mizoram using Remote Sensing and GIS, A project report. Mizoram State Remote Sensing Centre, S&T, Planning Dept. Mizoram, 28.

Nag, S.K. and S. Das (2014). Groundwater quality for irrigation and domestic purposes – a GIS based case study of Suri I and II blocks, Birbhum district, West Bengal, India. International Journal of Advancement in Earth and Environmental Sciences, 2(1), 25.

Neelakantan, R. and S. Yuvaraj (2012). Evaluation of ground water using geospatial data – A case study from Salem taluk, Tamil Nadu, India. International Journal of Remote Sensing & Geoscience, 1(2), 7.

Ramakrishna, N.D., Mohammad Suban Lone, S. Siddalingamurthy, and S. Sumithra (2013). Ground water prospectus studies of Tattekere watershed, Mysore district, Karnataka, India using remote sensing and GIS. International Journal of Remote Sensing & Geoscience, 3(1), 6-10.

RGNDWM (Rajiv Gandhi National Drinking Water Mission) (2011). Methodology Manual, 34.

Rokade,V.M., P. Kundal and A.K. Joshi (2004). Water resources development action plan for Sasti watershed, Chadrapur district, Maharashtra using remote sensing and Geographic Information System. Journal of the Indian Society of Remote Sensing, 32(4), 359-368.

Saraf,, A.K. and P.R. Choudhury (1998). Integrated remote sensing and GIS for ground water exploration and identification of artificial recharge site. International Journal of Remote Sensing, 19(10),825–1841.

Sharma, M.P. and A. Kujur (2012). Application of remote sensing and GIS for ground water recharge zone in and around Gola Block, Ramgarh district, Jharkhand, India. International Journal of Scientific and Research Publications, 2(2), 1.

Dey S. (2013). Delineation of ground water prospect zones using remote sensing, GIS Techniques - A case study of Baghmundi development Block of Puruliya district, West Bengal. International Journal of Geology, Earth & Environmental Sciences, 4(2), 62-72.

Shyamala, G. and J. Jeyanthi (2017). Integrated weighted overlay model using inverse distance weightage for assessing groundwater quality. Journal of Environmental Science and Management, 20(1), 26-32.

Vasanthavigar, M.K., Srinivasamoorthy, K. Vijayaragavan, K. Rajiv, R. Ganthi, R.S. Chidambaram, V.S. Sarama, P.R. Anandhan, Manivannan and S. Vasudevan (2010). Application of water quality index for ground water quality assessment: Thirumanimuttar Sub-basin, Tamilnadu, India. Environmental Monitoring and Assessment, 171(1-4), 595-609.

Journal of Geomatics Vol. 14, No. 1, April 2020

Assessment of landuse change implication on carbon stock of subtropical forests of East Khasi hills, Meghalaya

Biswajit Das*[1], Saurabh Baruah[1], Reetashree Bordoloi[1], Lobsang Tashi Thungon[1], Ashish Paul[1], Om Prakash Tripathi[1,2]
[1]Department of Forestry, North Eastern Regional Institute of Science and Technology
(Deemed to be University) Nirjuli – 791109, Arunachal Pradesh, India
[2]Department of Environmental Science, Mizoram University, Tanhril, Aizawl – 796004, Mizoram, India
*Email: biswajitdas.19.1989@gmail.com

(Received: Apr. 01, 2019; in final form: May 19, 2020)

Abstract: The study was carried out with an aim to enumerate the community characteristics, above ground biomass (AGB) and validation of field based biomass with the calculated AGB values using remote sensing and GIS. The study was carried out for East Khasi hills district of Meghalaya using random field sampling in selected land use. Sampling plots were selected in replicate keeping in account altiudinal variations and site characteristics. Soil samples were collected from two depths and anlyzed using sandard methods. The species richness was more in subtropical broad-leaved (SBL) forest than the pine forest (PF). However, stand density and basal cover was more in pine forest primarilly due to large number of individuals having more girth. Total tree biomass estimated in the SBL and PF were 300.5 t ha^{-1} and 195.89 t ha^{-1}, respectively. However predicted AGB was 232.77 t ha^{-1} in the SBL stand and 152.08 t ha^{-1} in PF stand. However, calculated AGB was 300.28 t ha^{-1} in SBL forest and 215.8 t ha^{-1} in PF. Finally, spatial carbon stock map of the selected forest type was prepared and the average biomass carbon was 128.02 t ha^{-1} in SBL and 107.9 t ha^{-1} in pine forest. Total carbon stock was calculated by summing the carbon stock of different pool i.e., tree, litter and soil. Implication of the land use change revealed that an amount of 86.36% carbon will be emitted in the situation when SBL is converted into abandoned land. However, an amount of 82.67% carbon will be emitted when PF are converted into abandoned land.

Keywords: LULC, Soil, Carbon, GIS, Emission

1. Introduction

Climate is one among the vital basis of vegetation composition globally and having important stimulus on species distribution and structural and functional aspect of the forests. It has been reported that landscape plant composition and soil acts as a noteworthy sink of atmospheric carbon dioxide (CO_2) (Wani et al., 2010). About 6.22 and 2.1 Gt CO_2 were released annually through deforestation and forest degradation, respectively (Pearson et al., 2017). About 80% of the above-ground terrestrial carbon and 40% of below-ground terrestrial carbon is stored in the forests (Olson et al., 1983; Dixon and Turner, 1991). Worldwide it has been recognized that deforestation and forest degradation requisite effective management for minimizing greenhouse gas emissions (GHGs). Changes in forest management generally results in less carbon sequestration (Lal and Singh, 2000). Global warming is viewed as increment in normal temperature of the Earth's surface and seas in late decades and its anticipated continuation. The Intergovernmental Panel on Climate Change (IPCC, 2007) anticipates that worldwide temperatures are probably going to rise by 1.1 to 6.4 °C between 1990 and 2100. The CO_2 is the specific constituent of photosynthesis hence influencing plant effectiveness while it is also the key members of ozone harming substances. Hence it is wise to acknowledge that alterations in climate scenario would also alter the functioning system of biological community. Other than carbon in the soil, forests also store a lot of carbon in the biomass (Freibauer et al., 2004). The biomass is by and large progressively used to measure pools and fluxes of GHGs along with land use changes (Cairns et al., 2003). To know the role of vegetation in carbon cycle, biomass and productivity estimations are the transitional steps (Kale et al., 2002). The measure of carbon sequestered by forests can be evaluated from biomass and is roughly 50% of forest dry biomass weight comprises carbon (Cairns et al., 2003; MacDicken, 1997). Researchers have developed a number of allometric equations for biomass estimation and were used at national level aboveground biomass studies (Chave et al., 2005). Further geospatial approaches, recently become more important and play a crucial role in mapping and monitoring forest degradation of large area with very minimum effort and time. Remote sensed images have shown high correlation between spectral bands and vegetation parameters like above ground biomass for the large area (Roy and Ravan, 1996; Lu, 2005).

Many studies reveal that satellite derived spectral vegetation indices such as simple ratio (SR), normalized difference vegetation index (NDVI) and enhanced vegetation index (EVI) have very strong relationship with biomass and plant productivity (de Fries et al., 1995; Kale et al., 2002; Roy and Ravan ,1996). Gupta and Sharma (2014) carried out a study on estimation of biomass and carbon sequestration of trees in protected area of Rajouri, India and reported 34.52 tons of carbon in its standing biomass. Bordoloi et al. (2017) had applied non-destructive approach and estimated AGB of 269.65 Mg Ha^{-1} and 206.03 Mg Ha^{-1} for *Tectona grandis* and *Gmelina arborea* plantations, respectively in Papum Pare districts of Arunachal Pradesh. Devagiri et al. (2013) carried out a remote sensing based approach to estimate AGB and carbon pool and reported 7.25 to 287.047 Mg ha^{-1} AGB from south western part of Karnataka. Kashung et al. (2018) had applied vegetation indices based approach in different landuse sector and reported 84.94 to 218.21 Mg ha^{-1} AGB from West Kameng district

Arunachal Pradesh. The aim of current study was to predict biomass and carbon stock in different forest type and effect of landuse implication on carbon stock of the study area.

2. Study area

The East Khasi Hills district is situated in south-central part of state of Meghalaya having a border with Bangladesh in the south. The district occupies a total geographical area of 2,748 km^2 (Figure 1) and is situated between 25°07″ and 25°41″ N latitude and 91°21″and 92°09″ E longitude. The climate of the district varied from tropical to temperate and weather is humid for major portion of the year excluding fairly dry period during December and March. The district is influenced by the south-west monsoon and receives heavy rainfall.

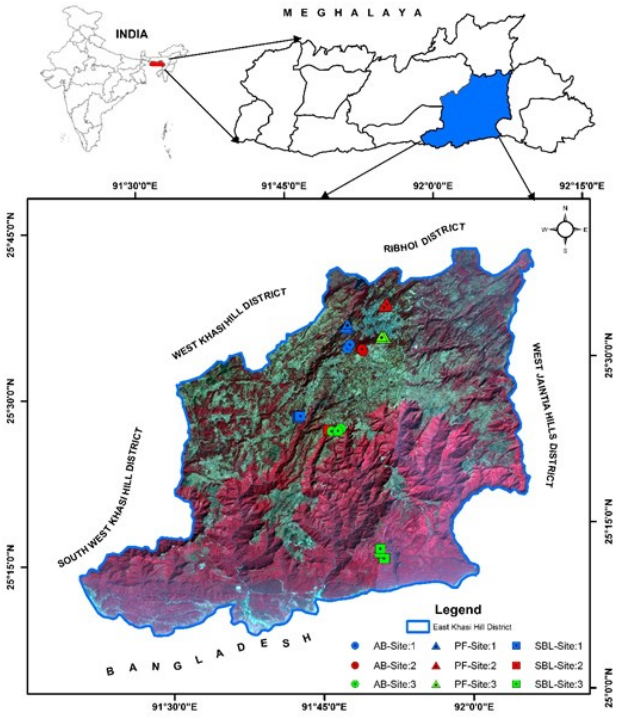

Figure 1: Location map of the study area

3. Materials and Methodology

The study has three phase work which include primary data collection, spatial and non-spatial database creation and spectral modelling. The field measurement was carried out in three different landuse types viz., subtropical broad-leaved forest (SBF), Pine forest (PF) and abandoned lands (AL). Altogether 45 quadrats (0.1 ha) were laid in selected forest patches using non-destructive approach. All the individual (dbh ≥10cm) encountered in the quadrats were measured with their height and diameter at breast height (1.37m above ground level). For litter carbon estimation, litter samples were collected from 1m x 1m qudrat from each sample plot in replicates and were brought to laboratory for further analysis. Soil samples were collected from each plot from two soil depths (0-25 cm and 25-50 cm). Soil pH, moisture content, bulk density and soil carbon were determined following standard methodology (Allen et al., 1974; Anderson and Ingram, 1993). The tested quadrat of the study area is covered by 3 sets of Landsat operational Land Imager (OLI) satellite data with 30m spectral resolution (path/row:136/42,136/43, and 137/42) downloaded from Earth Explorer. All these tiles have undergone the preprocessing operations viz., band-wise radiometric calibration for removal of spurious digital number in raw satellite data, which converted the DN values to at sensor radiance and conversion to surface reflectance following USGS (2019), layer stacking of bands to get false colour composite (FCC) image and re-projection to Universal Transverse Mercator projection system with zone 46 north. All the images were then mosaicked, study area was extracted and followed by land use and land cover classification using supervised approach (Figure 2).

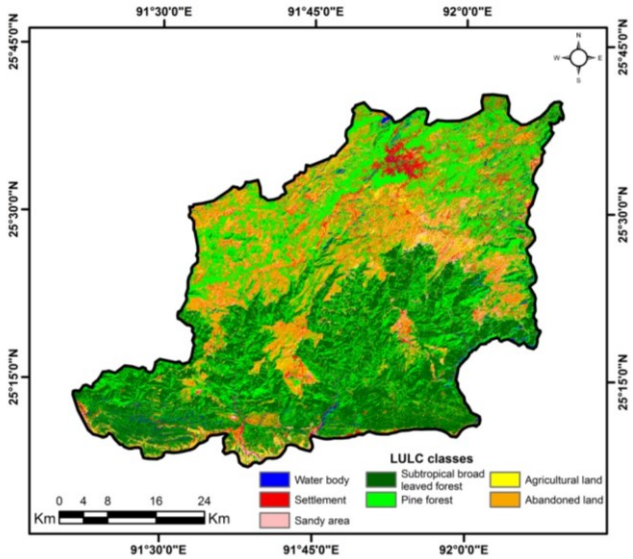

Figure 2: LULC map of the study area

The study area was classified into seven category namely waterbody, settlement, sandy area, subtropical broad-leaved forest, pine forest, agricultural land, and abandoned land (includes barren and degraded forest). The species-specific volumetric equations along with specific gravity or wood density were applied for calculating the volume of each individual tree. Tree alometric equations for many species were not available, hence general equation of the state were used. A fraction of 0.55 of biomass was used for estimating AGB carbon stock while below ground biomass (BGB) was estimated by taking 0.26 fraction of AGB (IPCC, 2003). The total carbon stock was calculated by summing the carbon stock of different pools viz. tree, litter and soil carbon. The prediction of biomass was carried out for selected landuse with the help of satellite data using Normalized Difference Vegetation Index (NDVI) Rouse et al. (1974) and Soil Adjusted Vegetation Index (SAVI), Huete (1988). A linear regression analysis was applied to find out the correlation between different vegetation indices and observed AGB. The resultant best-fit model was then used for spectral modeling of biomass and carbon stock of selected land use. Satellite derived vegetation indices were applied to the image of study area and based on location of sample plot, values of vegetation indices were extracted for each plot. Linear regression model was

applied to extracted vegetation indices value against the plot biomass based on field inventory data.

4. Results

4.1 Soil characteristics

Bulk density value of the SBL ranged from 0.70 g cm^3 while the values were 1.27 g cm^3 and 1.06 g cm^3 in the pine forest and abandoned lands, respectively. Arunachalam and Arunachalam (2000) have reported BD of 1 gcm^3 from sacred forest, Mawphlang forests, Meghalaya. The soil moisture content was greater (55.93% to 19.86%) in the upper soil layer than the lower soil layer (15.99% to 45.78 %). The moisture content in abandoned land was unusually higher than the rest of the sites which could be mainly due to dense ground growth. The pH of soil was acidic and values varied from 3.89 to 6.60 in upper soil depth and 4.25 to 6.96 in the lower soil depth. Soil pH was higher in PF followed by AL and SBL. In SBL forest, the upper soil layer showed lower pH than the lower soil depth which could be associated to lower levels of organic matter and greater extent of leaching of a few nutrient elements. The SOC is the organic fraction of soil exclusive of non-decomposed plant and animal residues and is an important indicator of soil health, mitigation and adaptation to climate change. Percentage of SOC ranged from 1.14% to 2.87 % in the upper layer and 0.82% to 2.13% in lower soil depth which shows vertical variability of SOC distribution (Table 1). In upper soil depth Site-2 of SBF had the greater percentage of SOC in both the soil depths while more organic carbon in lower soil depth was in Site-2 of SBL forests. High SOC provides nutrients to plants, enhances soil fertility and improves the water availability. The upper soil depth had greater SOC than the loer soil depth in all the landuse sectors.

4.2. Above ground biomass and carbon

Altogether, 71 tree species were recorded from the SBL and pine forest and the broad-leaved forests recorded maximum species richness (63 species) than the pine forest. Stand density did not differ much and ranges between 558 stems ha^{-1} and 585 stems ha^{-1} with basal area of 34.43 m^2 ha^{-1} to 38.10 m^2 ha^{-1} in the former and later forest stands. The litter carbon was lower (0.82 t ha^{-1} to 2.33 t ha^{-1}) in the SBL than the pine forest which could be attributed due to slow decomposition of pine needles. The SOC ranged from 21.25 t ha^{-1} to 41.53 t ha^{-1} in the SBL and 46.04 t ha^{-1} to 69.22 t ha^{-1} in the PF and 28.89 t ha^{-1} to 47.33 t ha^{-1} in abandoned land. The plot wise (0.1 ha) total biomass for the study area ranged from 10.67 to 62.76 t. The total biomass estimated in SBL forest was 300.5 t ha^{-1} where in the pine forest it was 195. 89 t ha^{-1}. Plot wise total biomass in SBL forest ranged from 13.21 t to 62.76 t and 10.69 to 27.58 t in Pine forest. The total carbon stock estimated were 165.28 t ha^{-1} for SBL forest and 107.74 t ha^{-1}in the Pine forest (Table 3). Pala et al. (2013) reported much higher biomass (1159.900 Mg ha^{-1}) and carbon density (587.190 Mg ha^{-1}) from sacred groves of Garhwal Himalaya. Waikhom et al. (2018) reported AGB from 962.94 to 1130.79 Mg ha^{-1} from sacred groves of Manipur. However, Sundarapandian et al. (2012) reported lower biomass (74.8 mt ha^{-1}) and carbon (47.13 mt ha^{-1}) density. Simalarily Devagiri et al. (2013) had reported lower biomass (70 t ha^{-1}) and carbon stock (33 t ha^{-1}). Correlation was established between plot biomass (t/ha) and basal area for each site and higher coefficient value was observed in Pine forest (R^2 = 0.97) than the SBL (R^2 = 0.95).

4.3. Regression analysis between vegetation indices and plot-based biomass

Satellite derived vegetation indices were extracted for each plot and linear regression model was applied to extracted vegetation indices against the field-based plot biomass. The reflectance based NDVI ranged between -0.74 and 0.84 (Figure 3a) and the negative values of NDVI correspond to waterbodies/lakes. NDVI value of SBL forest ranged from 0.27 to 0.73, in pine forest from 0.35 to 0.54 and 0.22 to 0.35 in the abandoned land. The NDVI and plot based correlation coefficient was low (R^2=0.47). The advantage of SAVI is that it the soil background effect and results are better than the NDVI. The SAVI value ranged from -0.22 to 0.63 while plot wise values varies between 0.09 and 0.44 (Figure 3b). The plot wise SAVI values (0.18 to 0.44) of SBL forest was more than the pine forest (0.14 to 0.25) and abandoned land (0.09 to 0.22). When linear regression model was applied to the extracted values of SAVI and biomass it showed greater correlation coefficient value (R^2=0.71) than the NDVI mainly could be because it considers the soil brightness factor and minimized the effects **(**Table 2**).** Linear regression analysis between field based estimated AGB and satellite derived vegetation indices were carried out to comprehend their associations. The observed correlation coefficient can be compared with the values of R^2=0.73, 0.70 and 0.68 as reported by Devagiri et al. (2013), Das et al. (2017) and Kashung et al. (2018).

4.4 Biomass and carbon stock modelling

The SAVI based model derived from linear regression analysis among the different vegetation indices and field based biomass was applied for modeling of total biomass of selected land use. The predicted total AGB for the study area was 199.91 t ha^{-1} (Figure 4). However, predicted biomass was 232.77 t ha^{-1} and 152.08 t ha^{-1} for SBL and Pine forest (Table 3). The mean total carbon stock for study area was 109.95 t ha^{-1}. The maximum total biomass carbon stock predicted for the SBL forest was 128.02 t ha^{-1} and for Pine forest was 107.90 t ha^{-1}. The predicted spatial carbon stock in different forest type is given in Figure 4. Carbon is among the larger constituents of the biomass and to assess carbon stock from biomass. We have used coefficient of 0.55 for calculating total biomass carbon of the area and total carbon. SBF stores greater carbon stock than the Pine forest followed by the abandoned land. Further PF accumulate greater carbon in the soil than the other two landuse (Table 4). Implication of the landuse change revealed that an amount of 86.36% carbon will be emitted in the situation when SBL forest is being converted into abandoned land. However, an amount of 82.67% carbon will be emitted in the situation when PF is being converted into AL. However once AL is converted into broad-leaved forest through management about 7.33 times carbon will be captured and stored while 5.77 times carbon will be stored in case of Pine forest.

.

Table 1: Soil organic carbon (%) in selected landuse types of East Khasi hills district, Meghalaya

Sites/ Soil depths (cm)	SBL		PF		AL	
	0-25cm	25-50cm	0-25cm	25-50cm	0-25cm	25-50cm
Site-1	2.2±0.15	1.75±0.05	1.39±0.07	1.24±0.02	1.77±0.01	1.386±0.02
Site-2	2.87±0.15	2.04±0.11	2.13±0.04	1.82±0.03	1.54±0.03	1.32±0.02
Site-3	1.33±0.16	0.82±0.08	1.72±0.03	1.44±0.006	1.14±0.04	0.94±0.09

Table 2: Coefficient for R^2 for biomass and different vegetation indices

Vegetation Indices	Equation	R^2
Normalize Difference vegetation Index (NDVI)	y = 42.325x – 3.6739	0.47
Soil adjusted vegetation Index (SAVI)	y = 78.895 x– 1.512	0.71

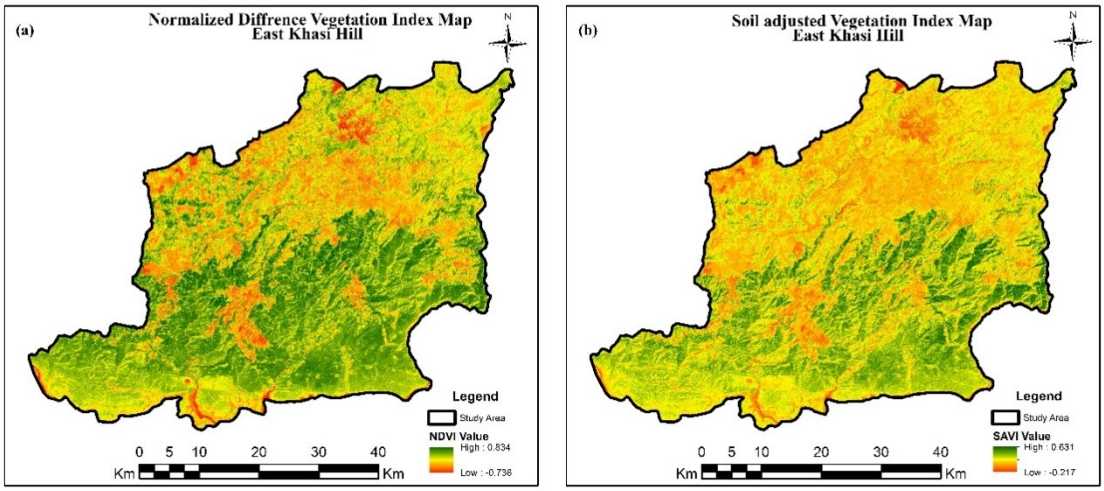

Figure 3: (a) NDVI (b) SAVI map of the study area

Table 3: Predicted and observed AGB and AGB carbon

AGB and carbon stock (t ha^{-1})	Average entire study area	SBL Forest	Pine Forest
Total Estimated biomass	256.91	300.50	195.88
Total Predicted biomass	199.91	232.77	152.08
Total Estimated carbon stock	141.30	165.28	107.74
Total Predicted carbon stock	109.95	128.02	107.90

Table 4: Carbon stock (t/ha) in different pool of selected landuse

Carbon stock	Broad-leaved forest	Pine forest	Abandoned land
AGB	165.28	107.74	-
BGB (root)	90.90	59.25	-
Litter	1.79	2.56	-
Soil	30.09	57.15	39.28
Total	288.06	226.70	39.28

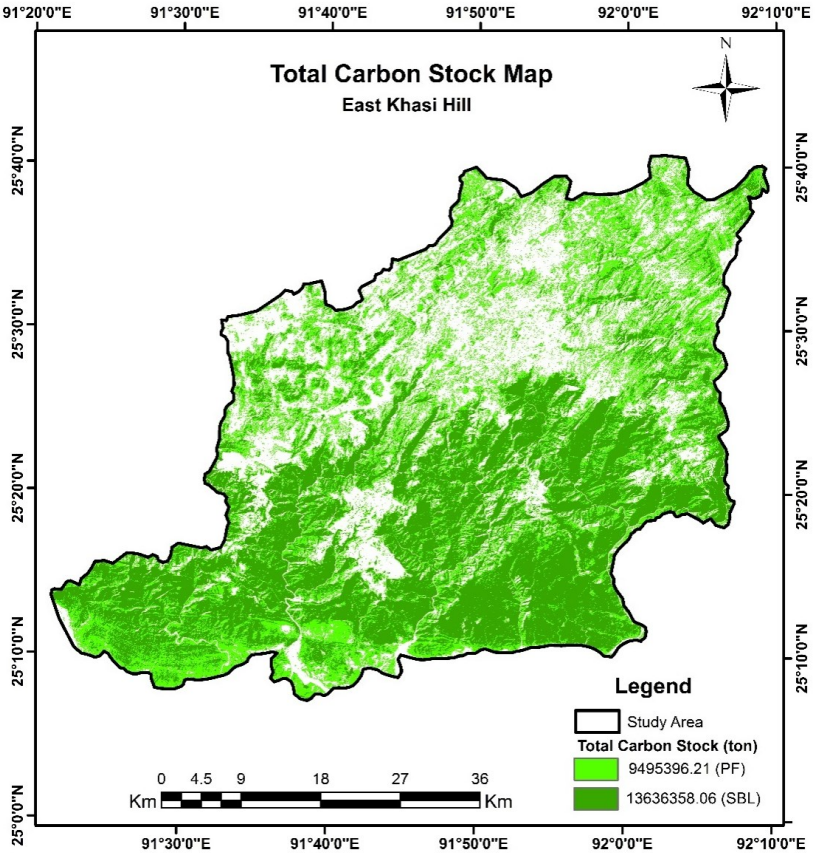

Figure 4: Predicted Carbon stock map for the study area

5. Conclusion

All together 71 tree species were recorded from study area and species richness was more in SBL forest the pine forest. Soil was acidic in nature and acidity was more in Pine forest. Acidity decreases with increase in soil depth mainly due to leaching and precipitation. Soil was sandy in nature. AGB was found to be greater in SBL forest than the pine forest and similar trend was obtained for carbon. Satellite derived biomass and carbon of selected landuse was also calculated using NDVI and SAVI indices. SAVI has resulted better correlation with the observed carbon values. Spatial maps of biomass and carbon was prepared using SAVI regression equation which will be useful for formulating suitable strategic plan for future enhancement of carbon stock of the study area. Total geographical area under subtropical broad-leaved and Pine forests in East Khasi hills district is 106517 ha and 88001 ha, respectively. Total estimated AGB for former forest was 17596675 tonnes and 9433795 tonnes for later forest with an average of 165.2 tones/ha and 107.2 tones/ha, respectively. Subtropical broad-leaved forest stores greater carbon stock than the Pine forest followed by the abandoned land. However, Pine forest accumulates more carbon in the soil than the other two land use. Implication of the land use change revealed that an amount of 86.36% carbon will be emitted in the situation that SBL forest is being converted into abandoned land. However, 82.67% carbon will be emitted in the situation when pine forests are being converted into abandoned land.

References

Allen, S.E., H.M. Grimshaw, J.A. Parkinson and C. Quarmby (1974). Chemical analysis of ecological materials, John Wiley and Sons, New York.

Arunachalam, A., and K. Arunachalam (2000). Influence of gap size and soil properties on microbial biomass in a subtropical humid forest of north-east India, Plant and Soil, 223(1-2), 187-195.

Bordoloi, R., B. Das and O.P. Tripathi (2017). Biomass estimation in plantation forests of Papum Pare district of Arunachal Pradesh, Malaya Journal of Biosciences, 4*(2)*, 63-70.

Cairns, M.A., I. Olmsted, J. Granados and J. Argaez (2003). Composition and aboveground tree biomass of a dry semi-evergreen forest on Mexico's Yucatan Peninsula, Forest Ecology and Management, 186(1–3), 125–132. http://doi.org/10.1016/S0378-1127(03)00229-9

Chave, J. et al. (2005). Tre allometry and improved estimation of carbon stocks and balance in tropical forests, Oecologia, 145, 87-89, 10.1007/s00442-005-0100-x.

Das, B., S. Deka, R. Bordoloi, P.K. Pandey, L.B. Singha and O.P. Tripathi (2017). Rapid assessment of above ground biomass in forest of Papum Pare district of Arunachal Pradesh: a geospatial approach, Malaya Journal of Biosciences, 4*(2)*, 48-*55*.

de Fries, R., M. Hansen and J. Townshend (1995). Global discrimination of land cover types from metrics derived from AVHRR pathfinder data, Remote Sensing of Environment, 54, 209-222.

Devagiri, G.M., S. Money, S. Singh, V.K. Dadhawal, P. Patil, A. Khaple, A.S. Devakumar and S. Hubballi (2013). Assessment of above ground biomass and carbon pool in different vegetation types of south western part of Karnataka, India using spectral modeling, Tropical Ecology, 54(2), 149–165.

Dixon, R.K., and D.P. Turner (1991). The global carbon cycle and climate change: responses and feedbacks from below-ground systems. Environmental Pollution, 73(3-4), 245-262.

Freibauer, A., M.D.A. Rounsevell, P. Smith and J. Verhagen (2004). Carbon sequestration in the agricultural soils of Europe. Geoderma 122, 1–23.

Gupta, B., and S. Sharma (2014). Estimation of biomass and carbon sequestration of trees in informally protected areas of Rajouri, J&K. India. International Research Journal of Environmental Science, 3(6), 56-61.

IPCC, (2003). Good practice guidance for land use, land-use change and forestry.

IPCC, (2007). Climate change 2007: Synthesis Report. Contribution of working group I, II, and III to the Fourth assessment Report of the Intergovernmental Panel on Climate change. IIPC, Geneve Swizerland, 1-104

Huete, A.R., (1988). A soil-adjusted vegetation index (SAVI), Remote Sensing of Environment, 25(3), 295-309.

Kale, M.P., S. Singh and P.S. Roy (2002). Biomass and productivity estimation using aerospace data and Geographic Information System, Tropical Ecology, 43(1), 123-136.

Kashung, Y., B. Das, S. Deka, R. Bordoloi, A. Paul and O.P. Tripathi (2018). Geospatial technology-based diversity and above ground biomass assessment of woody species of West Kameng district of Arunachal Pradesh, Forest Science and Technology, 14(2), 84-90.

Lal, M. and R. Singh (2000). Carbon sequestration potential of Indian forests. Environmental Monitoring and Assessment, 60(3), 315-327.

USGS (2019). Landsat 8 (L8) Data Users Handbook, Department of Interior, US Geological Survey, LSDN-1574, Version 5.0, 106.

Lu, D. (2005). Aboveground biomass estimation using Landsat TM data in the Brazilian Amazon, International Journal of Remote Sensing, 26(12), 2509-2525.

MacDicken, K.G., (1997). Winrock Internationl Institute for Agricultural Development, Forest Carbon Monitoring Program.

Olson, J.S., J.A. Watts and L.J. Allison (1983). Carbon in live vegetation of major world ecosystems (No. DOE/NBB-0037). Oak Ridge National Lab., TN (USA).

Pearson, T.R., S. Brown, L. Murray and G. Sidman (2017). Greenhouse gas emissions from tropical forest degradation: an underestimated source, Carbon balance and management, 12(1), 3.

Rouse, J.W., R.H. Haas, D.W. Deering and J.A. Schell (1974). Monitoring the vernal advancement and retrogradation (Green wave effect) of natural vegetation. Final Report. RSC 1978-4, Remote Sensing Center, Texas A&M Univ., College Station.

Roy, P.S. and S.A. Ravan (1996). Biomass estimation using satellite remote sensing data-An investigation on possible approaches for natural forest, Journal of Biosciences, 21(4), 535–561. http://doi.org/10.1007/BF02703218

Sundarapandian, S.M., J.A. Dar, D.S. Gandhi, K.K. Srinivas and K. Subashree (2012). Estimation of biomass and carbon stocks in tropical dry forests in Sivagangai district, Tamil Nadu, India, International Journal of Environmental Science and Engineering Research, 4(3), 66-76.

Tan, K., S. Piao, C. Peng and J. Fang (2007). Satellite-based estimation of biomass carbon stocks for northeast China's forests between 1982 and 1999, Forest Ecology and Management, 240(1-3), 114-121.

Waikhom, A.C., A.J. Nath and P.S. Yadava, (2018). Aboveground biomass and carbon stock in the largest sacred grove of Manipur, Northeast India. Journal of Forestry Research, 29(2), 425-428.

Wani, N., A. Velmurugan and V.K. Dadhwal (2010). Assessment of agricultural crop and soil carbon pools in Madhya Pradesh, India, Tropical Ecology, 51(1), 1-19.

Journal of Geomatics Vol. 14, No. 1, April 2020

Backscatter and coherence analysis using space borne C-band data for forest characterization

Arunima Singh[1*], S.K.P. Kushwaha[2], and Shashi Kumar[3]
[1]Forestry and Ecology Department, Indian Institute of Remote Sensing, Dehradun, Uttarakhand - 248001, India
[2]Geomatics Group, Department of Civil Engineering, Indian Institute of Technology, Roorkee, Uttarakhand - 247667, India
[3]Photogrammetry and Remote Sensing Department, Indian Institute of Remote Sensing, Dehradun, Uttarakhand - 248001, India
*Email: singharunima92@gmail.com

(Received: Aug. 30, 2019; in final form: May 19, 2020)

Abstract: Synthetic Aperture Radar (SAR) has shown immense potential in the area of forestry and proved to be one of the important tools of remote sensing in the characterization of a forest. Paper reports finding of a study carried out to characterize the forest area in the Dudhwa National Park, Uttar Pradesh, India using optical and SAR data. Backscatter (polarization VV and VH) and coherence images were generated with the help of a pair of datasets (Sentinel-1A of 29 May 2018 and 10 June 2018) for classification. Classification of SAR data was carried out using two classifiers i.e., Random Forest (RF) and K-Dimensional (KD) tree K-Nearest Neighbors (KNN) classifier. Results of these classifications of Sentinel-1A C-band datasets were analyzed and evaluated with respect to a reference map of forest type map prepared using Maximum Likelihood Classification (MLC) of Sentinel-2 dataset (22 March 2018). The accuracy achieved for MLC classification is 82.3%. The Random Forest accuracy is 75.2%, and the correlation is 0.7464, whereas the KD KNN accuracy is 82.5%, and having a correlation value of 0.829. So, the backscatter and coherence values can be used for the classification of forest area.

Keywords: Maximum Likelihood Classifier (MLC), KD tree KNN, Random Forest (RF), C-band, Sentinel-1A and Sentinal-2

1. Introduction

Forests are an important component of the earth system. Forest helps in the recycling of water, purification of air, enable oxygen and absorption of carbon dioxide from the air, etc. Forests are not a single entity as they also possess other resources and make an entire ecosystem. The maintenance of an ecosystem requires every single unit to function properly. The forest ecosystem is getting disturbed due to human interference and over-exploitation of the resources. Monitoring, preservation, and maintenance of such a system is the utmost necessity. Remote sensing techniques provide unique solutions in the large-area assessment of forest resources as compared to time-consuming ground surveys.

Optical remote sensing data have been used for discriminating forest type and density (Hirschmugl et al., 2018), however, this technique is limited by sensing more of surface characteristics of the forest canopy (De Souza Mendes, 2019). Radar remote sensing is emerging technology in the field of forestry. Mapping and monitoring of dry tropical forests using SAR data are more useful in regions associated with frequent cloud cover. It has been observed that during mapping of a forest, a low incidence angle of the sensor is sensitive to biomass whereas high incidence angle of the sensor is sensitive to detect deforestation. The deforested area of the forest can be mapped using both optical and SAR datasets (Rahman and Sumantyo, 2010). The accuracy of the dominant forest type classification is fairly good but the mixed deciduous or coniferous species classification is comparatively erroneous (Saatchi and Rignot, 1997). The main focus of this study is to classify the forest area using Sentinel-1 C-band data at the species level using two machine learning algorithms and to generate a forest type map of the Dudhwa National Park. The classification was carried out by generating backscatter and coherence values.

1.1 Classification Techniques

1.1.1 Maximum Likelihood Classifier

The Maximum Likelihood Classifier (MLC) works on the Gaussian theory of probability distribution (Paola and Schowengerdt, 1995). The discriminating function for each of the class is shown in the equation no 1 where X is data vector, n is number of bands, Σ_i is covariance matrix of class i , U_i is the mean vector of class i.

$$g_i(X) = p(X|w_i)p(w_i) = \frac{p(w_i)}{(2\pi)^{n/2}|\Sigma_i|^{1/2}} \cdot e^{-(1/2)(X-U_i)^T\Sigma_i^{-1}(X-U_i)} \quad \text{..... 1}$$

1.1.2 Random Forest Classifier

The random forest deals with the tree predictors and further the resampling technique is used for the construction, the best split selected among all the attributes after the random sampling of all the attributes (Du et al., 2015).

1.1.3 KD Tree KNN Classifier

A new method is K- Nearest Neighbor (KNN) based on the maximal margin principle. A function is defined for the given points (x) in the defined dimensional input parameters. The entire set of training samples are ordered with respect to the given points (Blanzieri and Melgani, 2008). The algorithm used for the classification of the binary classification problems is shown in equation no 2 where y_{r_x} (i) is the class label of the ith nearest training sample.

$$kNN(x) = sign\left(\sum_{i=1}^{k} y_{r_x(i)}\right) \quad \text{..... 2}$$

1.1.4 SAR remote sensing for forest vegetation

Remote sensing sensors are of two types i.e., active and passive sensors. An active sensor can transmit electromagnetic (em) pulses through a transmitter to illuminate and it requires a receiver to receive the backscatter signals from the illuminated area of the Earth surface. The passive sensors are those which can not transmit electromagnetic pulses and they are completely dependent on any other source of energy to do the imaging. The sensors used in optical, thermal, and passive microwave remote sensing techniques are passive by nature that can measure the radiation illuminating from an object. Synthetic Aperture Radar (SAR) is an active radar imaging system that has been widely used for biophysical characterization of forest vegetation (Kumar et al., 2019, 2017; Tomar et al., 2019). The basic principles are the transmission of high-frequency pulses and recording of returning echoes to generate high spatial resolution images for various applications (Shimada et al., 2010). SAR Interferometry (InSAR) is a technique that utilizes the acquisition of two SAR data with the same SAR geometry over an area on the Earth's surface. InSAR-based approaches are using phase information for precise measurement of height and displacement. The InSAR phase component is proportional to the vertical structure of the scene under observation, in particular, relief topography can be obtained by means of two interferometric SAR surveys (López-Martínez et al., 2012). The accuracy of the coherence magnitude is obtained as a function of the number of pixels averaged and the number of independent samples per pixel (Touzi et al., 1999). A recent study shows, classification of the forest can be done using Sentinel-2 successfully and gives a fine classification result for forest types on large scale (Puletti et al., 2017).

Forest degradation is an important issue in global environmental studies. Changes in land cover classes such as a degraded forest are analyzed by supervised analysis and backscatter spatial statistics (De Grandi et al, 2015). A better approximation of relative canopy density than optical data derived canopy density is obtained using SAR C-band data which can penetrate through forest vegetation and make it possible to extract information of crown components (Varghese et al., 2016). Optical remote sensing data have been used in the past in discriminating forest type, density, and extent. Optical sensors have major limitations in providing information related to forest structure as they can only detect forest canopy (Kumar, 2009).

Main et al., (2016) have investigated the relationships between hyper- temporal C-band ASAR data and woody structural parameters. Sentinel-1 radar backscatter provides useful observations during the cloudy monsoon season. The spatio-temporal variations have been analyzed using sentinel-1 and sentinel-2 data for agriculture practices (Ferrant et al., 2017). Though remote sensing and GIS techniques are efficient in the assessment of forest health, the major advantage of SAR remote sensing is the assessment of biophysical parameters for landscapes that primarily depends upon traditional field methods (Chandola, 2014).

2. Study area

The Dudhwa National park is a part of the Dudhwa Tiger reserve and Kishanpur Wildlife sanctuary. The location of the park is on the Indo-Nepal border in the Nighasan Tehsil of District Lakhimpur Kheri in Uttar Pradesh, India and lies between 28˚18’ to 28˚42’N latitudes and 80˚28’ to 80˚57’ E longitudes (Figure 1). The total area of the park is around 768.62 km^2. The park is divided into two buffers, the southern and northern buffer which comprises 124.01 km^2 and 660.23 km^2 area. These areas were once part of the North Kheri Forest Division. It was declared as National Park by the State Government in 1975. The total grassland present is 19% of the forest area, the third-largest habitat in India and wetland comprising of rivers, streams, lakes, and marshes.

Dudhwa National Park is one of the most diverse forests in India, it comprises more of the endangered species, obligate species of tall wet grasslands, and species of restricted distribution. The total area is further subdivided into two parts, Core Zone and Buffer Zone, the former is 490.2 km^2 whereas later is having 190.03 km^2 and the total area taken for the study is 768.62 km^2. This is one of the most threatened ecosystems of India. The forest of the study area has been classified into two subcategories, tropical deciduous forest, and tropical evergreen forest.

The main flora consists of Sal (Shorea robusta), Asna (Terminalia tomentosa), Shisam (Dalbergia sisso), Jamun (Syzygium cumini), and Gular (Ficus glomerata). The grasslands are prominent features of the park. The wetlands constitute the third major habitat type.

3. Methodology

The processing of the datasets has been done in the Sentinel Application Platform (SNAP) version 5.0 software and interpretation, analysis is done in the R-studio. The pre-processing steps, generation of backscatter image, and coherence image are done in the SNAP software (Figure 2).

3.1 Backscatter image generation

The single look complex (SLC) data of Sentinel-1A was preprocessed to split the scene and to get a deburst product. The SLC data suffers from the slant range ambiguity due to the side looking nature of the SAR system. To minimize the slant range ambiguity the slant to ground range conversion is done. Slant to ground-range conversion includes the re-projection of Single Look Complex (SLC) data from slant- range onto a flat ellipsoid surface. The process redistributes the SLC data in range with equal pixel spacing. Due to two spatial resolutions within a single SAR resolution cell, the shape of the resolution cell becomes rectangular. To generate squaLopezre pixel shape the Multilooking operator of the SNAP v5.0 was used.

To obtain an amplitude image these two channels (real and imaginary) are combined to obtain the composite signal intensity and the pixels of the resultant image show amplitude values. The processing to obtain amplitude images from complex SAR data includes the square of

the sum of the square of the real and imaginary values of the complex pixel values of Sentinel-1 data. The radiometric calibration was performed to generate a normalized backscatter cross-section image. The backscatter image represents an actual radar return from a resolution cell that is a coherent sum of backscatter contribution due to different objects within the SAR resolution cell. The backscatter image was orthorectified with the help of the Range Doppler Terrain Correction algorithm of the SNAP v 5.0 tool to minimize the ambiguity in the SAR data due to the topographic variations of the scene. The digital elevation model (DEM) with a resolution of 1 arc-second (~ 30 meters) of the Shuttle Radar Topography Mission (SRTM) was used in the Orthorectification procedure. The backscatter cross-section image was normalized with a local angle of incidence image to get actual radar returns from the resolution cell.

3.2 Classification of the SAR data using Random Forest Classifier using backscatter values

The classification has been done using backscatter values as the threshold in the random forest classifier and the KD KNN Classifier and later on the accuracy of both the classifiers is compared.

3.3 Coherence image generation

The coherence is defined as the complex correlation between two SAR images. The coherence image is generated using two datasets i.e., master and slave image. InSAR coherence is a measure of the decorrelation of two co-registered SAR data acquired in interferometric mode. The interferometric SAR datasets are co-registered, stacked and multi looked. Coregistration was performed at the sub-pixel level that is an essential requirement of interferometric processing of the SAR data. To minimize the speckles from the coregistered product a total of four filters were tried and the refined Lee filter was used for removing speckles and noise from the data.

The coherence image shows the correlation between the pixels of master and slave images. The pixel values of a coherence image lie between 0 and 1. The pixel value 1 of a coherence image shows the total correlation and if the value lies near to zero then it shows total decorrelation. The objects that are stable and not going to change in the interferometric data acquisition show maximum coherence and unstable structure shows low coherence. The stable scatterers like rocks and urban structures behave like a stable structure and these objects appear brighter in the coherence image. Forest vegetation shows moderate to low coherence because the top canopy surface of the forest vegetation is not a completely stable structure.

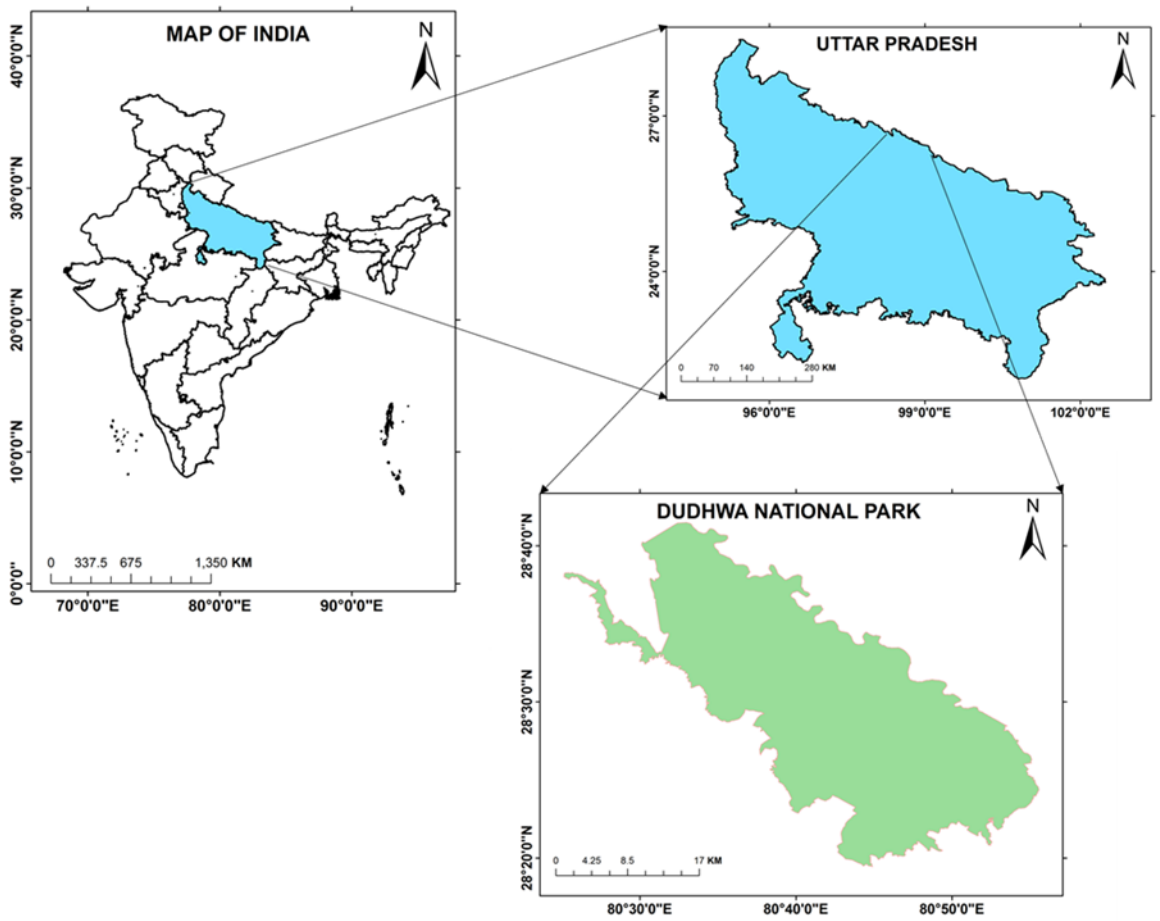

Figure 1: Location map of the study area

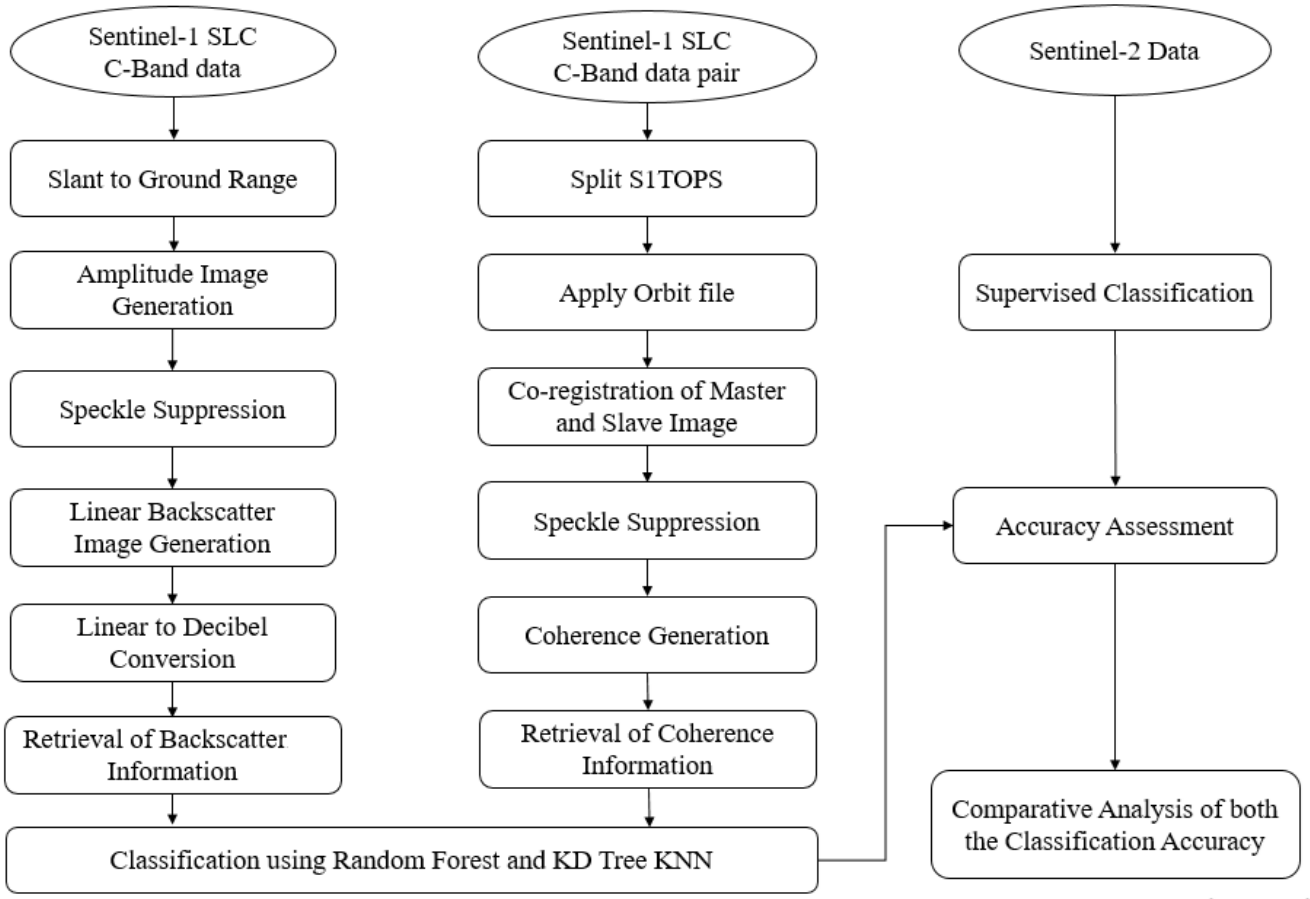

Figure 2: Workflow

Correlation values help in the identification of the density of the forest. Due to wind velocity variation and natural structure, forests shows high decorrelation. The settlements or urban areas also show a high correlation.

3.4 Satellite data used

The datasets used to carry out this research are shown in table-1.

Table 1: Datasets used in the study

Parameters	Data set-1	Data set-2	Data set-3
Sensor	SENTINEL-1	SENTINEL-1	SENTINEL-2
Date	29-05-2018	10-06-2018	22-04-2018
Orbit	22112	22287	
Track	165	165	
Product	S1A_IW_SLC_1SDV	S1A_IW_SLC_1SDV	
Polarization	VV+VH	VV+VH	
Swath	IW2	IW2	
Node	Descending	Descending	
Wavelength	5.6 cm	5.6 cm	

4. Results and discussions

4.1 Supervised classification of Dudhwa National Park using Sentinel 2 data

The vegetation type map (Figure 3) is prepared using supervised classification and maximum likelihood classifier using the Sentinel-2 data set. This map is used as a reference for assessing the accuracy of classification achieved using Sentinel 1A datasets. The training datasets are used and the accuracy obtained is 82.3 %. The classes used for the classification are Eucalyptus, Sal, Sal mixed, fallow land, settlements, grassland, scrubland, agriculture, waterbody, dry riverbed, open land. The maximum likelihood classifier works on the principle of the probability density function and it classifies the pixels into different classes based on their probability of finding that pixel into that particular class.

4.2 Backscatter values analysis of the VH and VV intensity for species-level mapping

Backscatter images of VH and VV (Figure 4 and Figure 5) are generated using the workflow shown in figure 2 and further analysis of the backscatter values is done for the classification and identification of the species classified in the optical data. The backscatter values are required to compare the classification accuracy because this gives the geometry and the structure of the tree. Also, the darker areas show the forest area comprising of different species with different values as well as the fallow land with the presence of moisture, whereas the brighter portion of the backscatter image shows settlement and open dry land. In this study, the information retrieved from the canopy of the tree is used for the classification of trees because C-band gives better canopy structure information than optical sensors.

4.2.1 Backscatter values of VH band

The cross-polarization is more sensitive to the forest zone because of the volume scattering phenomenon in a

forested area. The VH band is vertical transmit and horizontally received. Due to multiple scattering in the forest system, the cross polarised bands are more robust as compared to the co-polarised. The scattering from the forest occurs in the three components, that is, surface, double bounce, and direct scattering. The surface scattering occurs due to sparse vegetation and scattering from the ground, whereas the double bounce results due to the interaction of band from ground and trunk, and the direct scattering occurs from the crown of the tree. Since the C-band wavelength is comparatively shorter so, it cannot penetrate deep inside the forest so most of the scattering is obtained from the crown or little deeper till branches.

4.2.2 Backscatter values of VV band

The backscatter image generated using VV band is useful to discriminate built-up and dry riverbed and open land from other classes as these areas look much brighter than the other features. This is vertical transmit and vertical receive since the built-up features show double-bounce scattering.

The VV band is the vertical transmit and vertically received co-polarised wave which is best for the discrimination between the settlement and the open land and also can discriminate the vegetation within the built-up or the fallow land.

4.3 Backscatter maps of VV and VH bands to characterize forest area of Dudhwa National park using Random Forest Classifier and KNN Classifier

The Random Forest Classification of the area is done and the classification accuracy is satisfactory, it can be interpreted that the maximum error is 0.0085 in the classification of vegetation classes, especially in the plantation group (Figure 6), this is because of the mixing of the pixels of two interrelated classes. The KD KNN Classification has been done on the basis of different classes as in Random forest classification (Figure 7). The classes mainly taken are built-up, Eucalyptus, Sal, Sal-mixed, River bed, Open grassland, etc. But due to the mixing of pixel information of different vegetation types the class is further merged as vegetation class. The accuracy achieved with classifier is 82.5%, this accuracy came for three different classes as Built-up, Vegetation, and Open grassland. The accuracy of these classes is same for random forest classifier. The backscatter values of the segregating classes is mentioned in figure 4 and figure 5 for VH and VV bands respectively. The accuracy, correlation, and error rate are depicted in table 2 and statistical values of the KNN classifiers are given in table 3. This is for the Random forest classifier. It is clearly shown that the error rate is maximum for the Eucalyptus and Teak plantation. From both the classifier, few of the pixels get mixed for different classes, the backscatter values are nearly equal for these classes and hence, the accuracy is varied between the classifier and also for the mentioned classes. The comparative analysis of the two classifiers can be done. The Eucalyptus plantation, Teak plantation, Settlement, and Agriculture show pronounce accuracy in RF whereas it is poor in KNN. The classes such as scrubland, open land, waterbody are well segregated in the KNN classifier as a comparison to RF. The class-wise segregation performance of different classifiers is different and overall classification accuracy is different.

4.4 Coherence map of VV and VH bands between 29/5/2018 (Master image) and 10/6/2018 (Slave Image)

The coherence map shows different values for the different classes and the value ranges between 0 to 1, the higher coherence value shows the built-up areas whereas the lower values shown by the vegetation classes. This is the reason; the built-up area looks brighter in the image whereas vegetation parts look dull. Since C-band cannot penetrate deep through the canopy till the ground, so all we can get is the canopy information, the geometrical properties of the leaves, and the scattering behavior determines the backscatter values among the various vegetation types. The coherence image of both VV and VH bands gives information of correlation and decorrelation between the various features on the ground in the two different imagery which help in the identification of features. The coherence of VV and VH bands are generated and the values obtained are further analyzed. The VV band is able to separate the urban and grassland area from the forest (Figure 8 and Figure 10). The VH band is not effectively showing the clear cut demarcation between these classes (Figure 9 and Figure 11).

Table 2: The statistical values of the Random Forest classification of Sentinel-1 product of Dudhwa National Park

Class Type	Accuracy	Precision	Correlation	Error
Eucalyptus	0.559	0.4	0.483	0.44
Teak	0.58	0.147	0.473	0.41
Settlement	0.852	0.32	0.319	0.14
Agriculture	0.943	0.151	0.12	0.05
Scrubland	0.9161	0.076	0.085	0.083
Open land	0.9814	0.728	0.714	0.018
Water	0.998	0.842	0.841	0.0017

Table 3: The statistical values of the KNN Classifier of Sentinel-1 product of Dudhwa National Park

Class	Accuracy	Precision	Correlation	Error
Eucalyptus	0.44	0.32	0.321	0.56
Teak	0.35	0.132	0.355	0.52
Settlement	0.753	0.22	0.303	0.2
Agriculture	0.921	0.12	0.09	0.15
Scrubland	0.901	0.062	0.65	0.093
Open land	0.885	0.625	0.55	0.025
Water	0.865	0.785	0.75	0.0035

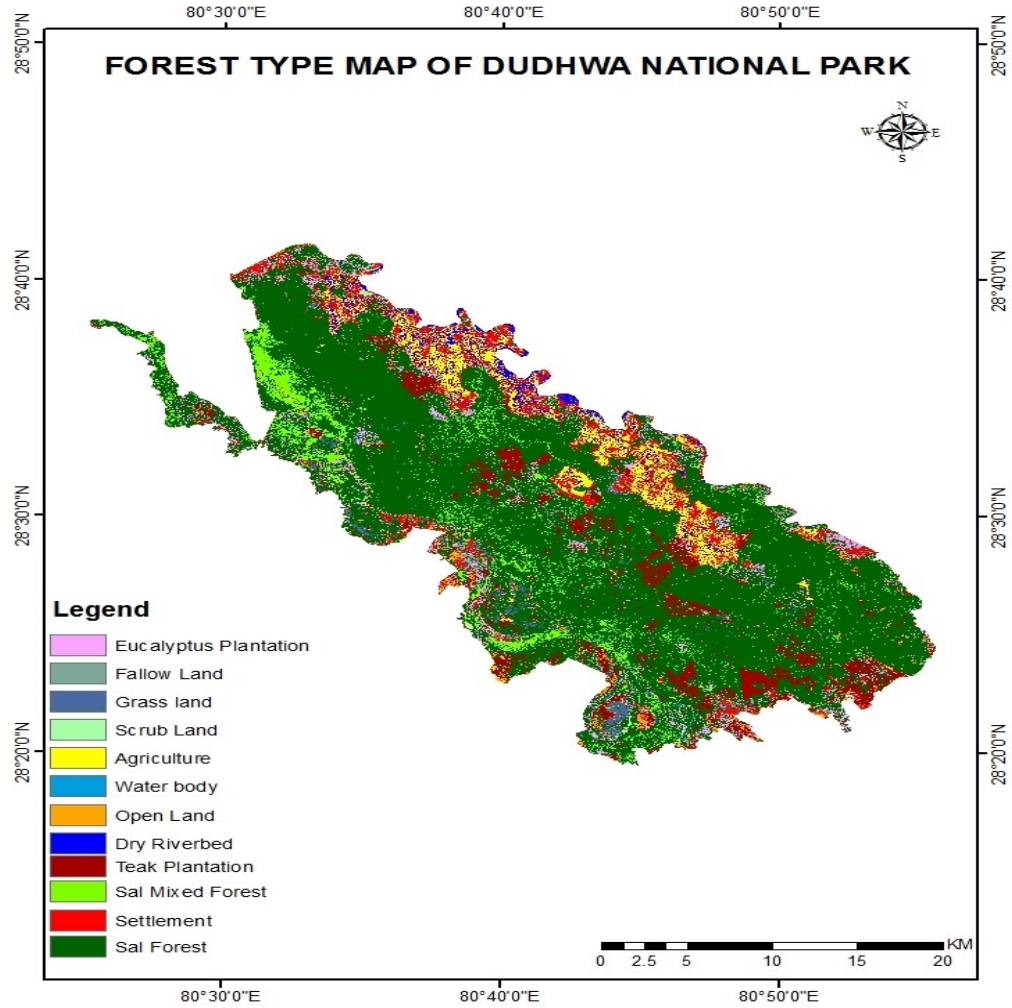

Figure 3: Supervised Classification Map of Dudhwa National park of different Forest types

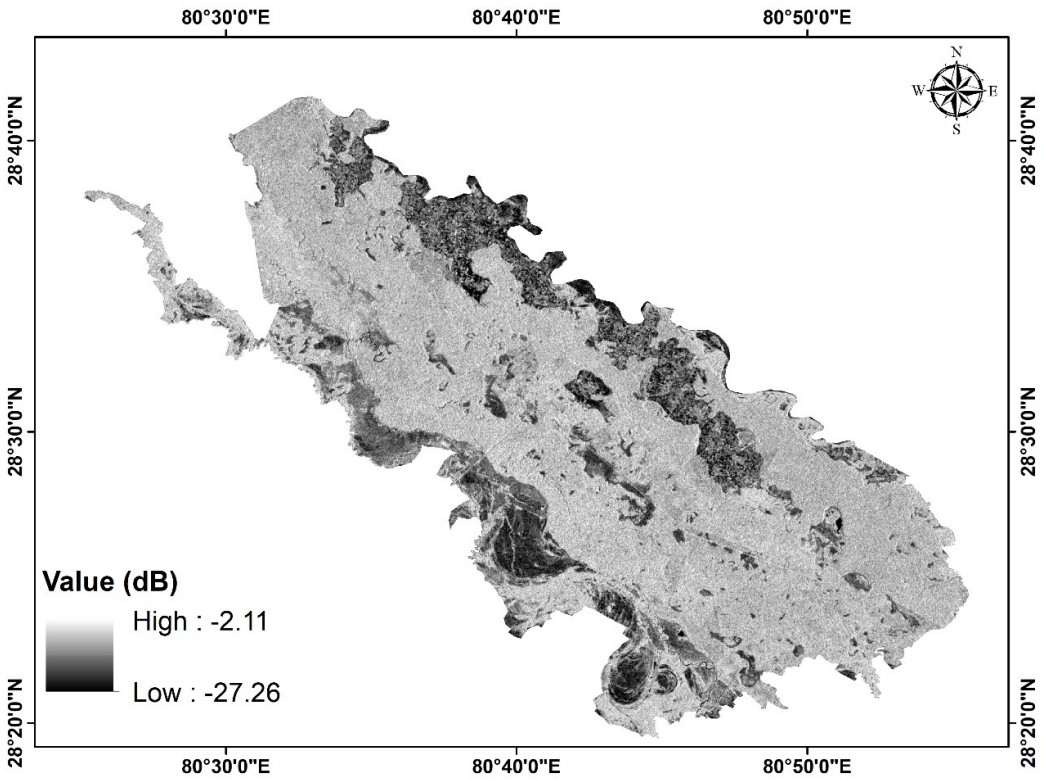

Figure 4: Backscatter map of VH band

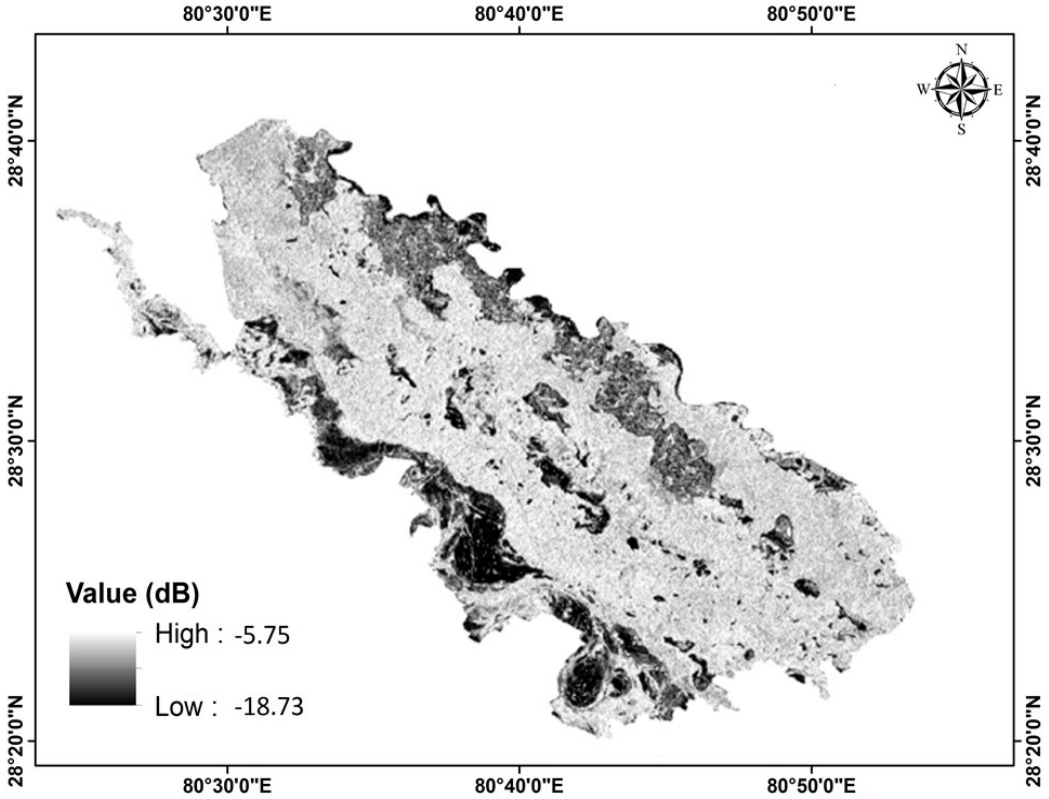

Figure 5: Backscatter map of VV band

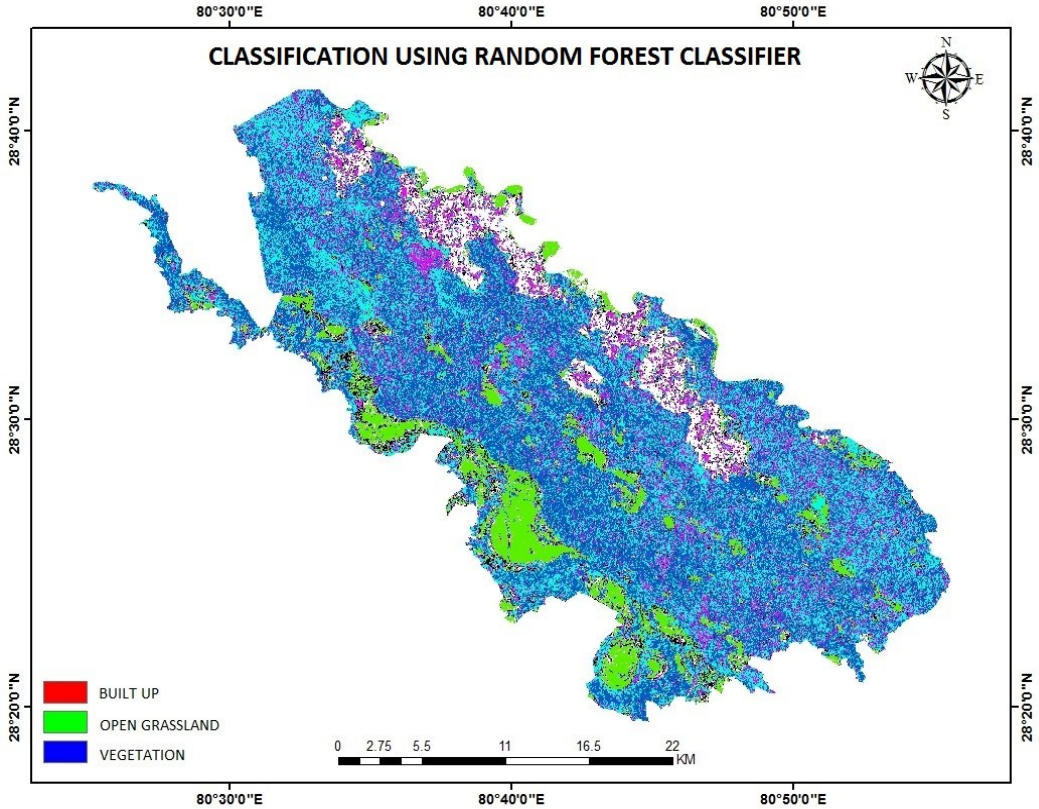

Figure 6: Classification map with the Random Forest Classifier using backscatter value

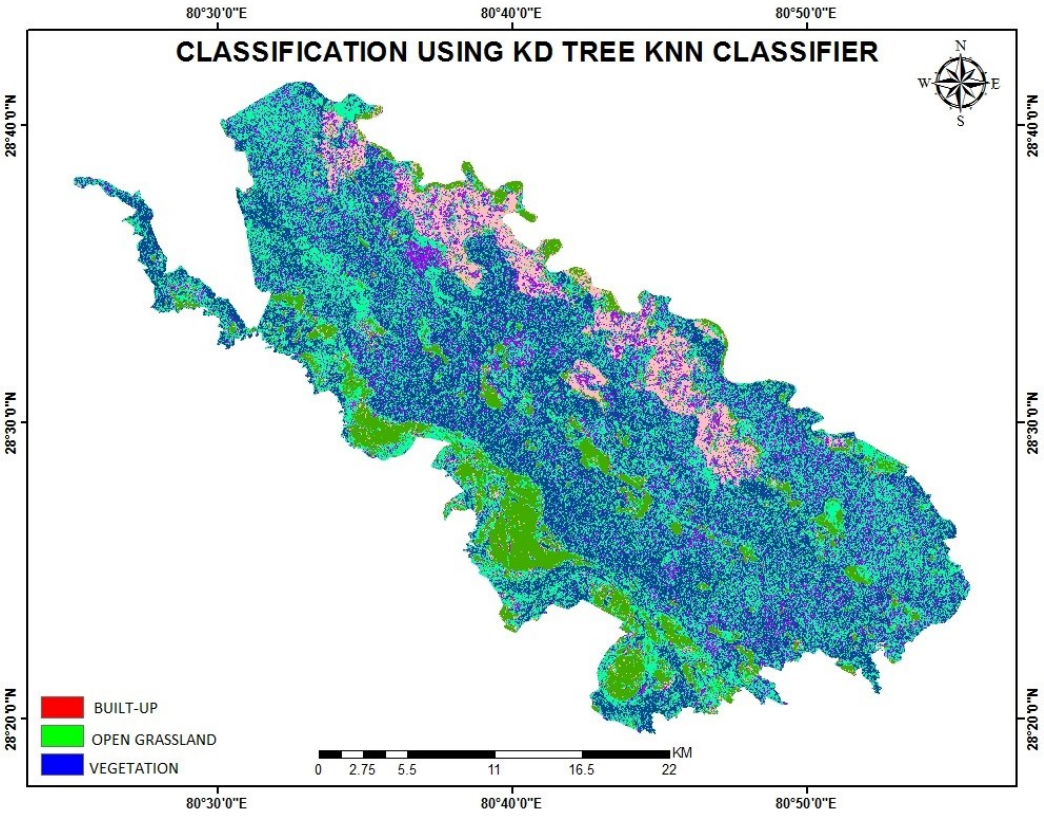

Figure 7: Classification map with the KNN Classifier using backscatter value

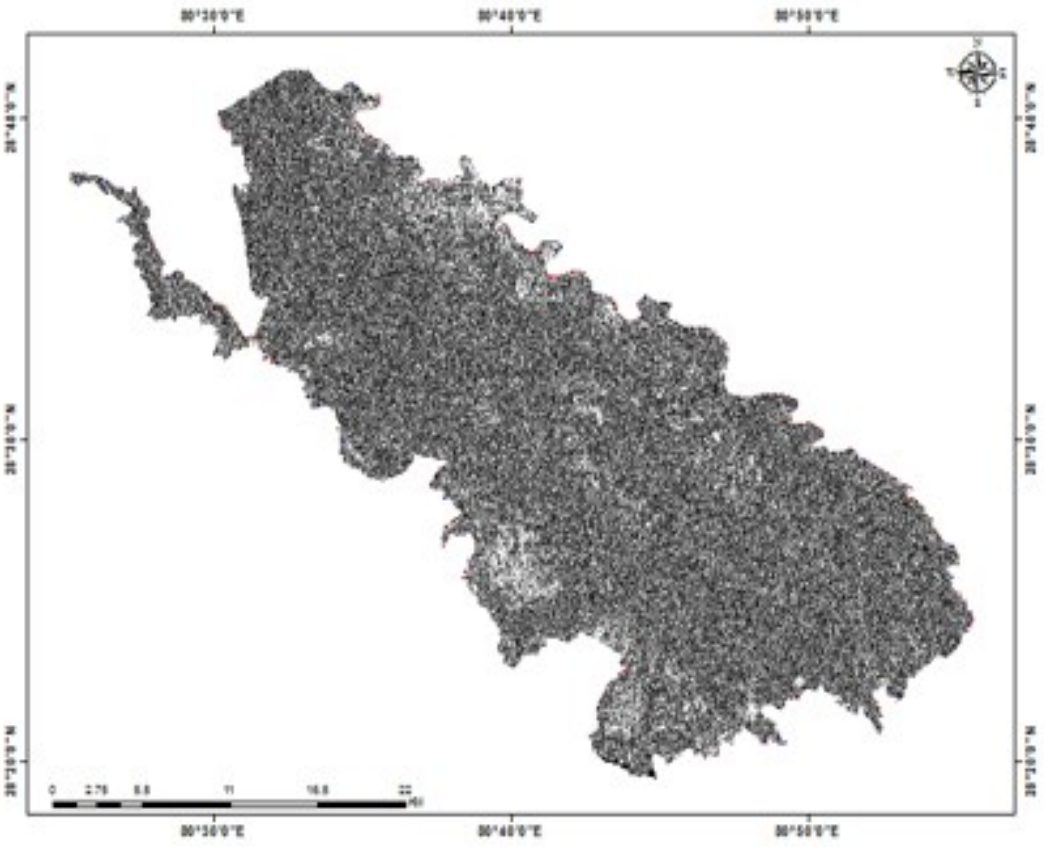

Figure 8: Coherence Map of VV band of Dudhwa National park

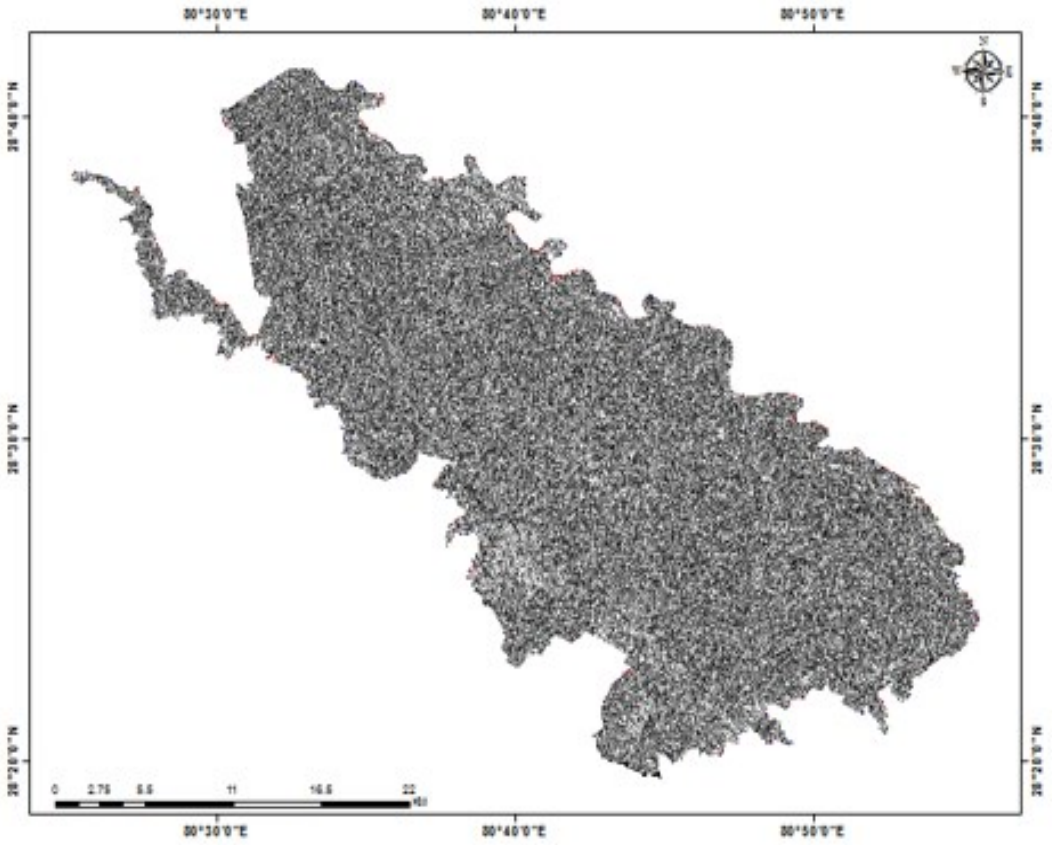

Figure 9: Coherence Map of VH band of Dudhwa National park

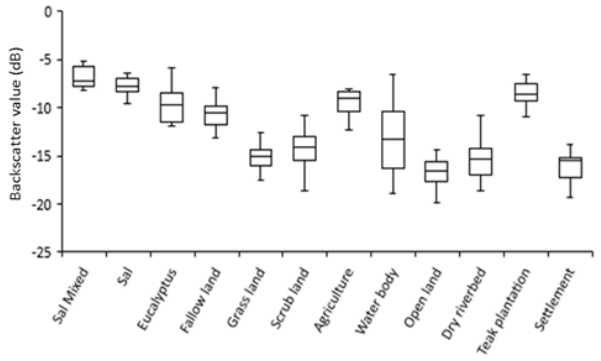

Figure 10: Backscatter values range for different classes of VV band

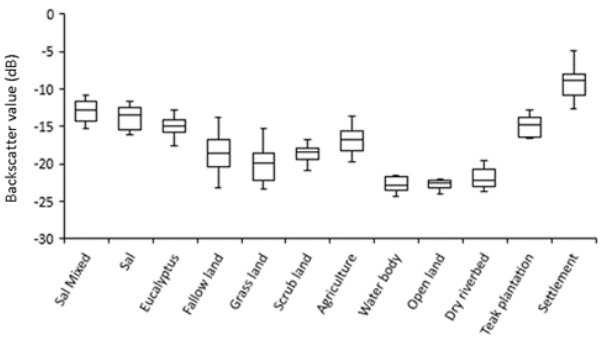

Figure 11: Backscatter values range for each class of VH band

5. Conclusions and recommendations

The classifications were done using two classification algorithms i.e., RF and KNN. The backscatter and coherence image information is used for the classification. Coherence proved to be efficient in the segregation of vegetative and non-vegetative classes. The built-up and vegetation areas show higher values of backscatter in the VH band. The accuracy assessment is done and based on that, it has shown that RF gave pronounced results as compared to KNN. It can be concluded that the mixed species in the forest area are not able to segregate due to mixing in the information of backscatter and coherence, whereas, the dominant species can be easily separated from the other classes. Multi-temporal observations of different seasons and advanced techniques like deep learning may further improve in the classification of forest Species.

References

Blanzieri, E. and F. Melgani (2008). Nearest neighbor classification of remote sensing images with the maximal margin principle. IEEE Transactions on Geoscience and Remote Sensing, 46(6), 1804–1811.

Chandola, S. (2014). Polarimetric SAR Interferometry for Forest Aboveground Biomass Estimation, M.Sc. (Geoinformation Science and Earth Observation) Thesis, ITC Netherlands and IIRS, Dehradun, India, 62p.

De Grandi, E.C., E. Mitchard, I.H. Woodhouse and G.D. De Grandi (2015). Spatial wavelet statistics of SAR

backscatter for characterizing degraded forest: A case study from Cameroon. IEEE Journal of Selected Topics in Applied Earth Observations and Remote Sensing, 8(7), 3572–3584, https://doi.org/10.1109/JSTARS.2015.2420596

De Souza Mendes, F., D. Baron, G. Gerold, V. Liesenberg and S. Erasmi (2019). Optical and SAR remote sensing synergism for mapping vegetation types in the endangered Cerrado / Amazon ecotone of Nova. Remote Sensing, 10(11), 1161.

Du, P., A. Samat, B. Waske, S. Liu and Z. Li (2015). Random forest and rotation forest for fully polarized SAR image classification using polarimetric and spatial features, ISPRS Journal of Photogrammetry and Remote Sensing, 105, 38–53. https://doi.org/10.1016/j.isprsjprs.2015.03.002

Ferrant, S., A. Selles, M. Le Page, P.A. Herrault, C. Pelletier, A. Al-Bitar, S. Mermoz, S. Gascoin, A. Bouvet, M. Saqalli, B. Dewandel, Y. Caballero, S. Ahmed, J.C. Maréchal and Y. Kerr (2017). Detection of irrigated crops from Sentinel-1 and Sentinel-2 data to estimate seasonal groundwater use in South India. Remote Sens. 9. https://doi.org/10.3390/rs9111119

Hirschmugl, M., C. Sobe, J. Deutscher and M. Schardt (2018). Combined use of optical and synthetic aperture radar Data for REDD + Applications in Malawi. Land, 4, 1–17. https://doi.org/10.3390/land7040116

Kumar, S., 2009. Retrieval of forest parameters from Envisat ASAR data for biomass inventory in Dudhwa National Park,U.P.,India. M.Sc.(Geoinformation Science and Earth Observation) Thesis, ITC Netherlands and IIRS, Dehradun, India, 80p.

Kumar, S., R.D. Garg, H. Govil, S.P.S. Kushwaha, 2019. PolSAR-decomposition-based extended water cloud modeling for forest aboveground biomass estimation. Remote Sens. 11, 1–27. https://doi.org/10.3390/rs11192287

Kumar, S., U.G. Khati, S. Chandola, S. Agrawal, S.P.S. Kushwaha, 2017. Polarimetric SAR Interferometry based modeling for tree height and aboveground biomass retrieval in a tropical deciduous forest. Adv. Sp. Res. 60, 571–586. https://doi.org/10.1016/j.asr.2017.04.018

López-Martínez, C., X. Fabregas and A. Alonso-González (2012). Analysis and validity of the PolInSAR line model on forested areas. In EUSAR 2012; 9th European Conference on Synthetic Aperture Radar (pp. 697–700).

Main, R., R. Mathieu, W. Kleynhans, K. Wessels, L. Naidoo and G. Asner (2016). Hyper-temporal C-band SAR for baseline woody structural assessments in deciduous savannas. Remote Sensing, 8(8), 661.

Paola, J.D. and R.A. Schowengerdt (1995). A detailed comparison of backpropagation neural network and maximum-likelihood classifiers for urban land use classification. IEEE Transactions on Geoscience and Remote Sensing, 33(4), 981–996. https://doi.org/10.1109/36.406684

Puletti, N., F. Chianucci and C. Castaldi (2017). Use of Sentinel-2 for forest classification in Mediterranean environments. Annals of Silvicultural Research, *0*(0), 1–7. https://doi.org/10.12899/asr-1463

Rahman, M.M. and J.T.S. Sumantyo (2010). Mapping tropical forest cover and deforestation using synthetic aperture radar (SAR) images. Applied Geomatics, 3(2), 113–121. https://doi.org/10.1007/s12518-010-0026-9

Saatchi, S.S. and Rignot, E. (1997). Classification of Boreal forest cover types using SAR images. Remote Sensing of Environment, *3*(60), 270–281.

Shimada, M., M. Ohki and H. Noguchi (2010). Incidence angle dependence of PALSAR repeat pass interferometry. In 8th European Conference on Synthetic Aperture Radar (pp. 1–4).

Tomar, K.S., S. Kumar and V.A. Tolpekin (2019). Evaluation of hybrid polarimetric decomposition techniques for forest biomass estimation, IEEE J. Sel. Top. Appl. Earth Obs. Remote Sens. 12, 3712–3718. https://doi.org/10.1109/JSTARS.2019.2947088

Touzi, R., A. Lopes, J. Bruniquel and P.W. Vachon (1999). Coherence estimation for SAR imagery, *I*EEE Transactions on Geoscience and Remote Sensing, 37(1 PART 1), 135–149. https://doi.org/10.1109/36.739146

Varghese, A.O., A. Suryavanshi, A. and A.K. Joshi (2016). Analysis of different polarimetric target decomposition methods in forest density classification using C band SAR data. International Journal of Remote Sensing, 37(3), 694–709. https://doi.org/10.1080/01431161.2015.1136448

Journal of Geomatics Vol. 14, No. 1, April 2020

WebGIS for water level monitoring and flood forecasting using Open Source Technology

Shweta Mishra*, Shard Chander, Rohit Pradhan, Amit Kumar Dubey, Markand P. Oza and Shashikant A. Sharma
Space Applications Centre, ISRO, Ahmedabad, Gujarat - 380015
*Email: jaiswals@sac.isro.gov.in

(Received: Jan. 07, 2020; in final form: June 30, 2020)

Abstract: Geographic Information System (GIS) has been widely used as a tool for spatial data manipulation, analysis and dissemination of spatial / non-spatial results in standardised format. This paper describes the design and implementation of a spatial database for satellite altimetry derived water level of large number of water bodies in India on a regular basis. Fully Automatic processing chain is developed which include downloading satellite data, water level extraction using developed models, database insertion and publishing of layers and graphs. The Web-GIS provides user-friendly GIS operations for visualizing thematic maps, as well as reporting services for selecting, displaying and downloading report of water level data for selected waterbody. The presented application developed using Free and Open Source Software (FOSS), facilitate user to visualise and plot the water level of various waterbodies at selected location and time period. It also provides next three days' water level forecast (Experimental), plots and downloading of a report for the Brahmaputra River in form of OGC Web services. Entire Application is developed using FOSS i.e. GDAL, Python, Flask (REST API), GeoServer, PostgreSQL and JavaScript APIs. Developed Application is deployed in Web Portal "VEDAS", developed by Space Applications Centre, ISRO, Ahmedabad and can be accessed through https://vedas.sac.gov.in/vstatic_1/hydro/index.html.

Keywords: WebGIS, Spatial Database, Hydrology, India, FOSS, OGC

1. Introduction

Hydrological data and related information on water resources such as river, reservoirs etc. in terms of water quantity and quality are key prerequisites for water resource management. Due to several human activities such as deforestation, urban development, unmanaged sewage discharge and water pollution, there is additional uncertainty on water resource status and conditions. Several hydrological models have been developed to simulate the hydrological cycle to help in decision-making and to find solutions for better water resource protection and management. Hydrological models mostly developed for research purpose, requires data from different resources (i.e. precipitation, DEM), involves complex interfaces, therefore, these models have not yet been applied to their full potential in terms of water resource management and policy-making (Zhang et al., 2019). To make outputs of these models available for public use for water resource management require tremendous efforts. As a tool, Geographic Information System (GIS) has a capability to acquire, store, and process spatial data for hydrological models. Applications and regular use of hydrological models became possible after integration with GIS. However, for operational deployment of model, user has to manually download required data at their end for further processing of data in GIS and regularly feed it to the model, which is itself a resource intensive task. Further, installation of software, integration of GIS and model all depend on the operating system. Additionally, due to huge cost of software and its maintenance, lack of domain expertise of GIS and hydrological modelling for their integration prevents the usage of models in mainstream use.

Combining GIS with web technologies provides facility to process spatial data, perform spatial analysis and display generated results using interactive maps or graphs in the web browser. Web-based GIS is an open source, distributed technology standardized by OGC (Open Geospatial Consortium) that brings GIS technology to the users in the form of interactive maps at little or no cost. In other words, Web-GIS provides a user-friendly interface to access spatial data, perform on-the-web spatial analysis and visualisation of Web-GIS services using web browser (Chhugani et al., 2018). In order to utilize these advantages, several researchers and application scientists have attempted to integrate scientific models with WebGIS. Mishra et al. (2017) have attempted to estimate crop intensity at pixel level and integrated the intensity estimation model with WebGIS. Vaitis et al. (2019) have developed a spatial database and WebGIS based Information System for Greece which provides a facility of cartographic operations for thematic maps visualisation and manipulation along with reporting services for selected areas. They have used spatial database to produce cartographic layers for climatic and other parameters through database views dynamically. Swain et al. (2015) have reviewed the several Free and Open Source Software (FOSS4G) solutions for web application development for water resources management. Choi et al. (2005) have developed a prototype of a spatial decision support system based on Web-based GIS for watershed management. It provides watershed delineation, map interfaces and data preparation, a hydrologic model for hydrologic/water quality impact analysis and web interface programs for operation through the Internet. Therefore, one of the greatest benefits of using WebGIS technology in decision making is to utilise its potential to overcome limitations in terms of cost, distance and geospatial data transfer. It is not required to install any expensive software and models at user end. User can simply access the developed WebGIS based system for visualising results using their web browsers and use it for further analysis and decision making. The results of the scientific models can be presented to multiple users simultaneously.

The dissemination and management of water related data i.e. water-level using web based information system is a promising technological approach for sharing information both with administrators and the general public. Using WebGIS technology, one can facilitate users with spatial data and descriptive information over the internet /cloud accessible through common web browsers. The data organisation and dissemination are based on standard data formats and transmission protocols (Costantino et al., 2019).

OGC is an international consortium responsible for making standards for geospatial information and services FAIR (Findable, Accessible, Interoperable and Reusable). Web Map Service (WMS), Web Feature Service (WFS) and Web Coverage Service (WCS) are the three important OGC standards. WMS is used to serve raster and vector data as GIS enabled images in PNG, JPEG or GIF format. OGC compliant WFS provides an access to vector data with authentication for insertion, manipulation and updation, whereas WCS is used to serve or share raster or image layers on the web. Web Processing Service (WPS) is another OGC standard that is used for Geoprocessing of data on the web (Sharma and Mishra, 2017).

This paper presents a WebGIS based information system developed using FOSS integrated with hydrological model. In this work, GIS is responsible for data capturing, preparation and providing required data to the model. Water level information generated by model is transferred to the database using developed scripts on daily basis. REST (Representational State Transfer) API (Application Programming Interface) is developed to publish the generated output images automatically and disseminate water level in graphical format. The main aim of this application is to provide water level data of user selected waterbody in user interface along with the overlay layers and related non-spatial data efficiently in web environment. Paper also describes the design and implementation of a spatial database used for satellite altimetry derived water level of water bodies in India on regular basis.

2. Methodology and Development Process

The main aim of this WebGIS information system is to provide appropriate tools under a web-based platform for analysing water level data at different locations which facilitates quick decision making for water management for present and future needs. The framework of the system has interactive Graphical User Interface, Hydrological model for water level estimation from satellite derived data and spatial database for derived water level storage and management. There are two hydrological models viz., i) for water level estimation developed using different satellite derived products at various locations in India, ii) for the inundation probability forecast (Experimental) for Brahmaputra River in North-East Indian region. Brief methodology, specifications of sensors and products used to water level estimation along with relevant references are provided in following sections.

2.1 Water level estimation from Scatterometer and altimeter

Traditional method to measure water level uses in-situ hydrological stations such as water level gauge, radar gauge etc. These instruments are sensitive to long term drift and highly vulnerable during extreme events such as floods. Thus they require time-to-time testing and calibration which is time consuming and expensive. Remote sensing can play a crucial role in estimation of these hydrological variables with acceptable accuracy. Methodology is developed for estimation of river water level and detection of surface inundation using SCATSAT-1 derived backscattering coefficient and Brightness Temperature (BT) datasets respectively (Gupta et al., 2019). SCATSAT-1 is used to estimate river water levels utilizing satellite-measured soil wetness conditions through the process of run-off at the catchment scale. Detailed methodology is described in Gupta et al., (2019). Gauging sites covering some of the major river basins of India such as the Brahmaputra, Godavari, Mahi, Tapi, Narmada, Mahanadi, Subarnarekha, Brahmini and Baitrani were taken for river water level retrieval (Figure 1). Altimeters are non-imaging, nadir looking instruments that covers the same location after fix interval of time, temporal resolution varies between 10 to 35 days depending upon the altitude of the sensor (dense track coverage for later). Altimeters send an electromagnetic pulse towards earth surface and measures the returned power and time information. This time vs power graph is known is "Waveform" in altimetry community. These waveforms can have different shapes such as ocean-like, specular, peaky, rectangular etc. depending on the roughness and dielectric variability within the altimeter foot-print (Desai et al., 2015). These waveforms are than retraced by either physics based models or shape based empirical retrackers (Ganguly et al., 2015).

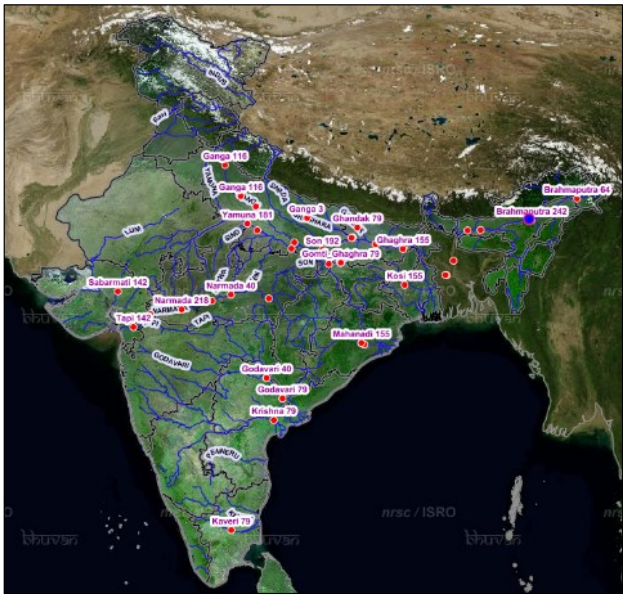

Figure 1: Gauging sites of the major rivers used for river water level retrieval using SCATSAT-1

Dedicated inland water range corrections, that takes care the atmospheric and air-water effects are also required to convert range into water level information (Chander et al.,

2017). A complete algorithm chain starting from raw altimetry measurements to water stage estimation is provided in Chander et al., 2017. Figure 2 shows sites of the major rivers used for river water level retrieval using JASON (Joint Altimetry Satellite Oceanography Network) series of altimeter (https://podaac.jpl.nasa.gov/JASON3).

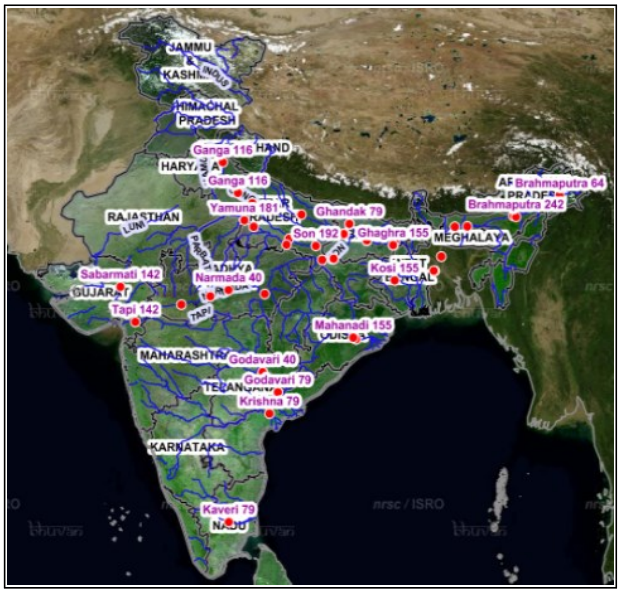

Figure 2: Gauging sites of the major rivers used for river water level retrieval using JASON-3 Altimeter

2.2 Short range water level and inundation forecast for the Brahmaputra River

The Brahmaputra River experiences number of long-duration flood waves during the monsoon season annually. Therefore, near real time flood prediction at basin scale with available weather forecast dataset is necessity for effective flood management. In the present study, WRF-Hydro model was setup over the Brahmaputra river basin for hourly discharge estimation at Guwahati gauge station. WRF (Weather Research Forecasting)-Hydro model is used to predict next 3-day water level and inundation probability in the Brahmaputra river at Guwahati gauge station. VEDAS Hydrology Forecast (2020) provides more insight into water level and inundation forecast for the Brahmaputra River.

2.3 Integration of hydrological models with WebGIS

To feed required datasets to the hydrological models, scripts are coded in python. Script is invoked immediately when data is available at data distribution site and download the data in specified directory. Hydrological models mentioned above are deployed on server and run through a developed python script and generate output on daily basis. For example, in case of model which is used for water level estimation from scatterometer, invoked through a python script, SCATSAT-1 derived backscattering coefficient and BT datasets are used by the model to generate output (text files) containing location IDs of basins along with water level at fixed output directory.

Immediately after the output generation, data from text files get transferred to a spatial database created to insert the water level data along with dates. Here PostgreSQL along with PostGIS is used to store and manage spatial data. PostgreSQL is an open source, spatial and relational database management system with an emphasis on extensibility and standards compliance. PostGIS is a spatial database extension for PostgreSQL which adds support for geographic objects allowing location queries to be run in SQL (https://postgresql.org). Master table containing location Ids and location of basins are stored in database. It is used to extract water level data for selected dates and location using spatial query operations. This table is published in WebGIS Server as Web Map Service (WMS) by making the connection between PostgreSQL and GeoServer. GeoServer (http://geoserver.org) is a WebGIS Server which is used here for sharing geospatial data on the web as WMS. RESTful web service is developed in flask framework in python which can be accessed through Hyper Text Transfer Protocol (HTTP). Python is an interpreted, object-oriented and high-level programming language. It supports modules and packages, which encourages program modularity and code reuse (https://python.org). Some of the packages used in development are GDAL, Psycopg2, Flask and gsconfig. Web service access the required water level datasets from the spatial database on the basis of a selected river basin of user. The same process is applied for water level generation, storage and dissemination from hydrological model using Jason-3 Altimeter products. In case of short range water level and inundation forecast for the Brahmaputra river, a daily 3-day inundation probability forecast (GeoTiff files) are generated. For automatic publishing of images gsconfig library is used. gsconfig is a python library for manipulating a GeoServer instance via GeoServer RESTConfigAPI (https://pypi.org/project/gsconfig/). Next 3-day every hour water-level estimation is also generated and stored in database using psycopg2 library. It is a PostgreSQL database adaptor for python programming language (https://pypi.org/project/psycopg2/).

2.4 WebGIS based Application Framework:

WebGIS provides a way for querying, monitoring, analysis and display of water level data for selected River / Reservoir location in India. The application framework is shown in figure 3. It is consisting of three main components: client, server and database. Client is any terminal that allows the interaction of users with the application and provides spatial and non-spatial information in an interactive way. Server includes Web GIS server, application server and spatial database server. Web server act as middle ware between Client and WebGIS server. When client makes a request, it will reach Web server first and then further Web Server parses the request and forward it to GeoServer for spatial data request and database for non-spatial data request. Thereafter the GeoServer or/and database server completes the query operations according to Web server requests and returns the relevant results to Web server. Subsequently Web server sends the results in the form of images through Web server. RESTful Web Service is created in Python to access the water level data for selected water body in User Interface.

VueJS (www.vuejs.org) JavaScript library and HTML are used for development of web application. Open Source JavaScript library Openlayers5 (https://openlayers.org) is used for creating map and displaying published spatial layers on the web. Geospatial data has no intrinsic visual component. In order to visualise the data with better understanding, style must be provided to the layer which means to specify the color, thickness, and other visible attributes. In GeoServer, OGC standard Styled Layer Descriptor (SLD) is used for styling. SLD is an XML-based markup language used for preparing illustrative visual map depictions.

3. Results

The WebGIS based application described in previous section is shown in figure 4. User Interface is consisting of Map Viewer and two tabs "Reference Layers" and "Data and Analysis" in the bottom. Reference Layer tab contains overlay layers i.e. Administrative boundaries, Rivers and streams, LISS-III Mosaic, Cartosat-1 Mosaic, AWiFS Mosaic etc. which are published as WMS in GeoServer. "Data and Analysis" tab contains three tabs as shown in figure 4.: - (i) Altimeter (ii) Forecast (iii) Scatterometer. By clicking on Altimeter tab, user gets options of selecting waterbody (River / Reservoir), location from combo box and dates. After clicking on submit button user gets water level estimation for selected location in graphical format as shown in figure 5. There is also an option for selecting "year over year profile" which provides facility to compare multiple years' data with each other.

Same functionality is provided in Scatterometer tab for water level visualisation for selected location of river. Daily Inundation Probability Forecast based on WRF-Hydro model is generated and automatically published in GeoServer. Same is shown in figure 6 for August 04, 2019. Graph is showing inundation water level forecast along with three levels (Warning Level, Danger Level and Highest Flood Level) starting from August 04, 2019 6:30 A.M. User can also download the inundation map and graph using "Export to PDF" functionality provided for generating and sharing reports. Developed WebGIS based Information system for Hydrology is deployed in VEDAS (https://vedas.sac.gov.in) Visualisation of Earth observation Data and Archival System (VEDAS) is a portal to showcase end-products from EO applications which feed into decision making system. Application can be access through VEDAS portal.

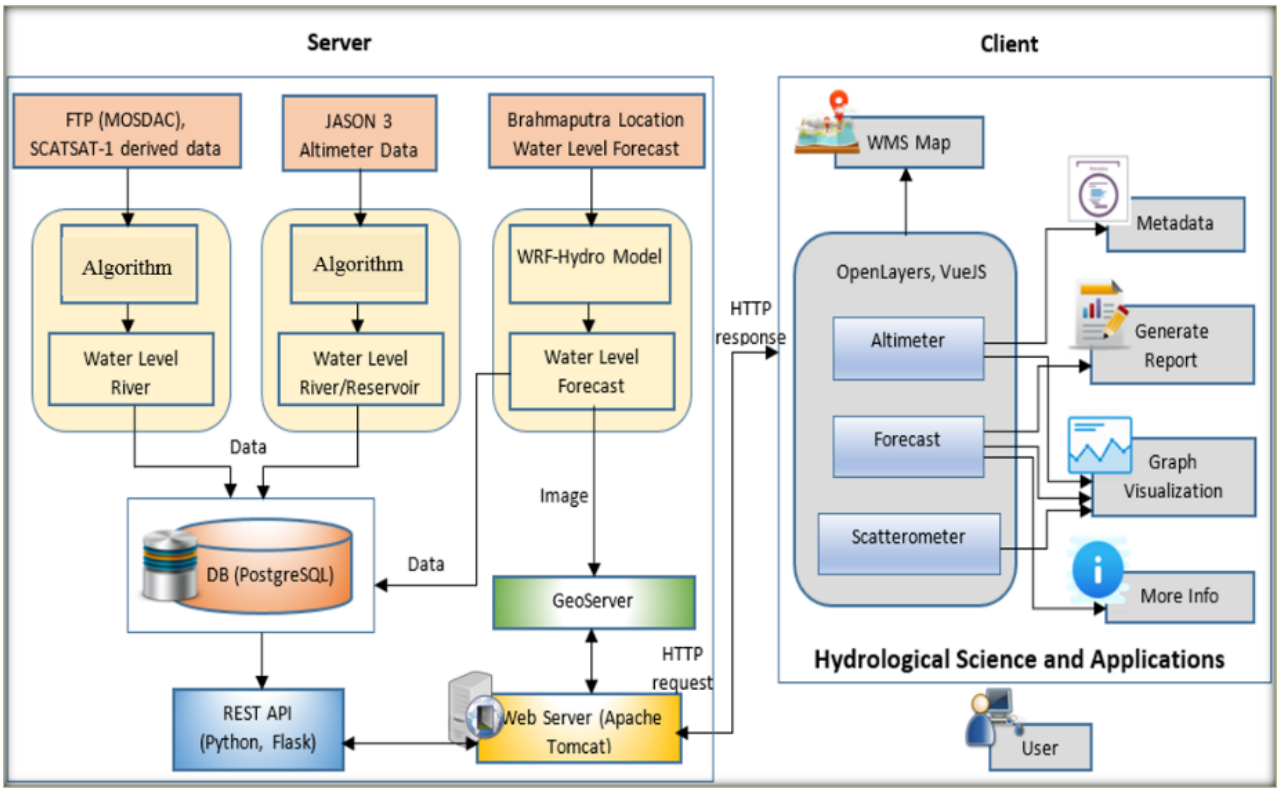

Figure 3: WebGIS based Application framework

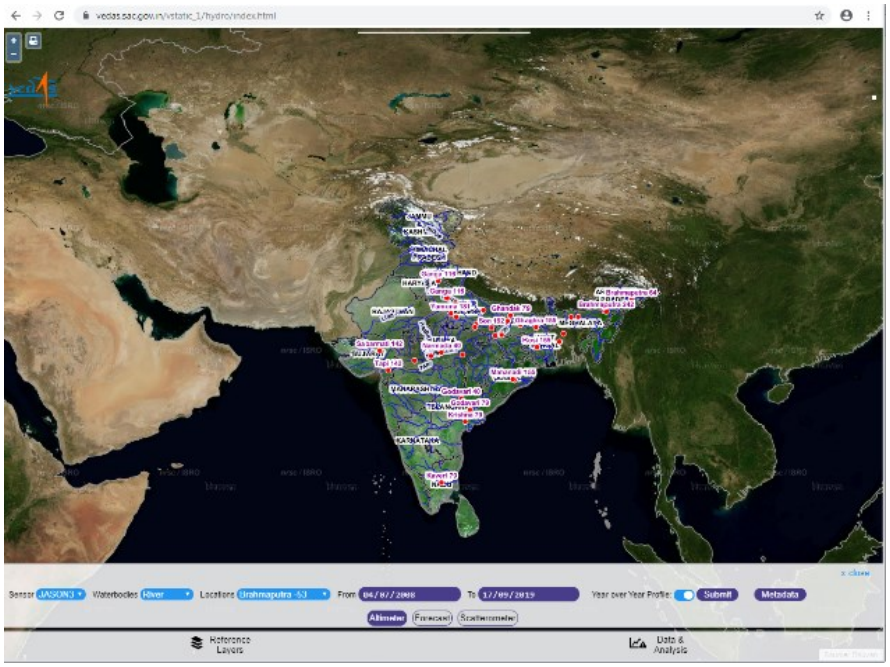

Figure 4: Main User Interface of WebGIS based Application

Figure 5: Water level of location Ganga-192 for selected dates

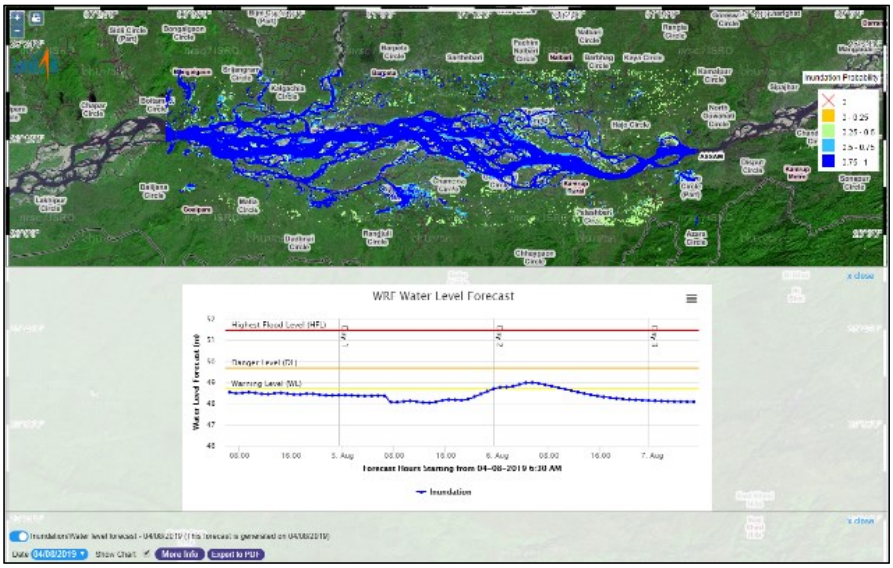

Figure 6: Inundation probability map and water level forecast for 04 August, 2019

4. Conclusion

A Web-based Framework has been developed to dynamically provide observed and predicted EO derived hydrological information for use by decision makers and the general public. It can be a useful system for decision-makers for river basin management and for potential users who require updated and ready access to easy-to-use water fluxes for hydrodynamic modelling. It shares the information and geospatial datasets allowing users with limited GIS knowledge to access the information customized for specific applications that reduces operation costs management.

Acknowledgements

The authors would like to thank Director, Space Applications Centre, ISRO, Deputy Director –EPSA for providing all required infrastructure and encouragement to conduct this work. The authors would also like to acknowledge the MOSDAC web portal of ISRO and JASON-3 data distribution websites for providing dataset and information for conducting this work.

References

Chander, S. and D. Ganguly (2017). Development of water level estimation algorithms using SARAL/Altika dataset and validation over the Ukai reservoir, India, Journal of Applied Remote Sensing, 11(1), 016012.

Chhugani, S., S. Mishra, G. Jain, S. Suthar and P. Shah (2018). Development of WebGIS based Information System: A case study of energy sector, Journal of Geomatics, 12(1), 63-68.

VEDAS Hydrology Forecast (2020). Experimental short range water level and inundation forecast for the Brahmaputra river. https://vedas.sac.gov.in/vstatic_1/hydro/pdf/WRF_Brahmaputra_Flood_Info.pdf, Retrieved June 30, 2020.

Desai, S., S. Chander, D. Ganguly and P. Chauhan (2015). Waveform classification and water-land transition over the Brahmaputra River using SARAL/AltiKa & Jason-2 Altimeter, Journal of the Indian Society of Remote Sensing, 43(3), 475-485.

Choi, J.Y., B.A. Engel and R.L. Farnsworth (2005). Web-based GIS and spatial decision support system for watershed management, Journal of Hydroinformatics, 7(3), 165-174.

Costantino, D., M.G. Angelini, V.S. Alfio, M. Claveri and F. Settembrini (2020). Implementation of a system WebGIS open-source for the protection and sustainable management of rural heritage, Applied Geomatics, 12, 41-54

Ganguly, D., S. Chander, S. Desai and P. Chauhan (2015). A subwaveform-based retracker for multipeak waveforms: a case study over Ukai dam/reservoir, Marine Geodesy, 38(sup1), 581-596.

Gupta, P.K., R. Pradhan, R.P. Singh and A. Misra (2019). Scatterometry for land hydrology science and its applications, Current Science, 117(6), 1014-1021.

Mishra S., M.P. Oza and S.A. Sharma (2017). Crop phenology identification using NDVI time-series and its dissemination using WebGIS, 38th Asian Conference on Remote Sensing, New Delhi, India, October 23-27, 2017.

Sharma, N. and S. Mishra (2017). Dissemination of heat wave alerts using spatial mashup technology and open source GIS, Journal of Geomatics, 11(2), 268-274.

Swain, N.R., K. Latu, S.D. Christensen, N.L. Jones, E.J. Nelson, D.P. Ames, and G.P. Williams (2015). A review of open source software solutions for developing water resources web applications. Environmental Modelling & Software, 67, 108-117.

Vaitis, M., H. Feidas, P. Symeonidis, V. Kopsachilis, D. Dalaperas, N. Koukourouvli, D. Simos and S. Taskaris (2019). Development of a spatial database and web-GIS for the climate of Greece, Earth Science Informatics, 12(1), 97-115.

Zhang, D., W. Fu, Q. Lin, and X. Chen (2019). WOF-SWAT: A web-based open-source framework for investigating the hydrological impacts of climate change and human activities through Online simulation and visualization of SWAT models, ISPRS International Journal of Geo-Information, 8, 368.

https://vedas.sac.gov.in/vstatic_1/hydro/index.html.

https://podaac.jpl.nasa.gov/JASON3

https://postgresql.org

http://geoserver.org

https://python.org

https://pypi.org/project/gsconfig/

https://pypi.org/project/psycopg2/

https://vuejs.org

https://openlayers.org

Journal of Geomatics Vol. 14, No. 1, April 2020

Integration of Cellular Automata-Markov Chain and Artificial Neural Network model for urban growth simulation

Kriti Rastogi* and Shashikant A. Sharma
Space Applications Centre, ISRO, Ahmedabad-380015
*Email: kritirastogi@sac.isro.gov.in

(Received: Jan 08, 2020; in final form: June 30, 2020)

Abstract: The urban sprawl and growth modelling helps in identifying areas of potential urban expansion. This will help in exploring alternatives in urban design and human-environment interactions. Also, it minimizes the negative impact of urban sprawl for sustainable and environment-friendly futures. In this study, a spatio-temporal urban growth modelling for year 1992-2032 of Ahmedabad city is performed by simulating historical urban built-up data and predicting future urban growth. The Indian Remote Sensing satellite data for year 1992, 2005 and 2018 is used for generating urban built-up land cover and change map. These are analysed along with the auxiliary data such as proximity from major roads, slope, population density which acts as the driving force for urban expansion. The integration of Cellular Automata-Markov Chain (CA-MC) model is used along with Artificial Neural Network for understanding the relationship between the driving forces and urban built-up. The urban built-up has increased from 146.67 km^2 to 193.82 km^2 during 1992 to 2005 which has further increased to 229.52 km^2 in 2018 with increase of 36% in urban built-up in past 27 years. The 2018 predicted urban expansion is validated using overall accuracy of 97% and with kappa value 0.94. The prediction of 2032 urban expansion as per the optimised ANN CA-MC model has an area of 275.76 km^2.The results show that the increase in built-up area are closely associated with the existing built-up areas.

Keywords: Urban Sprawl, Cellular Automata**,** Markov Chain, Artificial Neural Network

1. Introduction

Rapid increase in population lead to unprecedented urban growth stemming variety of complex problems such as traffic congestion, air pollution, deforestation, farmland decrease and chaotic urban settlements with poor infrastructure. Urban growth in sub-urban areas of the metropolitan cities are scattered development with low density, poor accessibility involving massive change in urban land cover affecting the ecosystem, biodiversity and natural resources. In order to ensure sustainable development, decision makers and urban planners needs precise information regarding the urban growth and its future expansion. Urban land cover and change analysis and urban growth prediction is an important input, for assessing the amount and impact of development and its consequence on the environment (Jiang and Yao, 2010). Also, it is helpful for understanding and developing theories of urban morphologies and its interaction with other land use classes for developing environmental models such as urban climate models.

India has taken major initiative to start smart cities mission for establishing sustainable cities through urban planning and proper management plans. Remote sensing and Geographical Information System (GIS) together offer a powerful tool for spatial and temporal analysis of urban growth and it can provide regular data of urban expansion. Urbanisation being a complex process needs comprehensive mathematical model, along with additional socio-economic and demographic variables for simulating its process. Several GIS-based mathematical models have been used for forecasting with spatial scope, such as Cellular Automata (CA) (Batty et al., 1999; Li and Yeh 2000; Sudhira et al., 2004; Aburas et al., 2016), Multi-Agent Model (Arsanjani et al., 2013; Zhang et al., 2015), Land Transformation Model (Pijanowski et al., 2002) and SLEUTH (Jat et al., 2017). Among these models, Cellular Automata (CA) is one of the most popular model used for simulation and prediction of urban growth.

CA simulations and predictions are governed on the assumption that previous urban growth will affect the future pattern through local and regional interactions among different land use classes (Sante et al, 2010). Because of its 'bottom-up' structure, CA can simulate the emergent macro-scale phenomenon (urban expansion) by micro-level interactions (cell state change) (Xu et.al., 2019). In allocating changes under the predefined conditional rules, CA always starts with the cells of the highest probability of change. Therefore, it is capable of predicting the most probable sites for development, estimating the probability of amount of change, as well as allocating the estimated quantity of change within a study area. However, the conventional CA approach considers only the neighbourhood effect in spatial allocation without quantitatively considering the role of urban expansion drivers (Aburas et al., 2016; Li et al., 2017; Mustafa et al., 2017).

The limitation of conventional CA model is resolved by its open structure, which can be integrated with other models such the logistic regression, fuzzy logic and Markov Chain (Wang et al., 2013; Bihamta et al., 2015) to stimulate urban growth pattern (Clarke, 1997). Among common integration of models Cellular Automata-Markov Chain (CA-MC) has been one of the popular methods used to model urban expansion. It requires comparatively smaller number of driving factors and physical constraints for adequately simulate and predict urban expansion (Arsanjani et al., 2013; Liu, 2012). For understanding the relation of urban growth with its drivers, logistic regression could be used for creating optimum set of variables for the CA-MC model. However, it may not work well if the relationship between urban expansion and its drivers is non-linear (Mustafa et al., 2017) and also

working with large datasets. In order to incorporate non-linearity between the urban expansion and its drivers, Artificial Neural Network is used. Integrated ANN-CA-MC has the ability to model complex non-linear relationships between dependent (such as urban growth) and independent variables (such as distance to roads, demographics etc) with fewer statistical assumptions and most importantly without knowing prior relation between these variables. For this reason, ANNs have been incorporated into other models such as CA-MC to simulate and predict urban expansion despite the difficulties in properly parameterizing and optimally configuring an ANN model.

In this study, we integrate an optimised ANN with CA-MC to stimulate and predict the urban expansion of Ahmedabad city in 2018 and 2032. This study attempts to identify the urban sprawl patterns using remote sensing and GIS technique and predicts the urban growth for future. The model is validated with the reference data, quantified using overall accuracy and kappa coefficient.

2. Study Area

Ahmedabad city is in the central part of Gujarat, India, which is located in the western part of India. It is a semi-arid region. It has an area of 720 sq. km (Figure 1). Ahmedabad is located on the banks of Sabarmati River. It emerges as an important economic and industrial hub in India. Historically, it is called "Manchester of East" and recently declared as Heritage City of India by UNESCO. The city is governed by Ahmedabad Municipal Corporation (AMC) and Ahmedabad Urban Development Authority (AUDA). AUDA is responsible for both land use planning and strategic planning of the city. As per the AMC, 2006, the inner city is considered as Central Business District (CBD) with dense building structures. Area east of Sabarmati river has old and dense building structures with several industries and area west of Sabarmati river is predominantly having residential, commercial and isolated buildings around farm lands.

3. Spatial Data Base Creation

Remote sensing data from Indian Remote Sensing satellite (IRS-1A) and Resouresat-1 and 2 for the year 1992, 2005 and 2018 for the month between Octobers to December have been used in this study. These images cover the entire area study area with same season, which is important for change detection analysis as it minimises seasonal vegetation differences and the effects of varying sun positions. Each time frame is classified into two classes urban and non-urban. Non-urban consists of classes such as vegetation, fallow land, soil and water bodies. These images were classified using semi-automated and object-based image analysis method with the accuracy of 89% (Jain and Sharma, 2019).

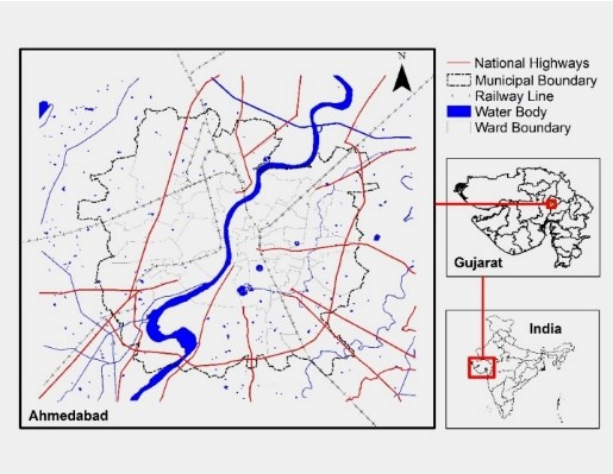

Figure 1: Study Area of Ahmedabad City

3.1 Auxiliary Data used

Driving factors are responsible for initiating the LULC change. These can be the categorised into, slope, elevation and infrastructure's proximity. Infrastructure's proximity such as proximity from road, highway is used. Slope is an important factor that drives the land cover changes, steep slope could become limiting factor for built-up area. However, most of built-up area is found to be in relatively flat area because of its relative easiness for building construction. All of driving factors are used for CA-MC model based on Artificial Neural Network. The auxiliary data for this study includes physical factors (DEM, slope), Euclidian distance to road networks and population data obtained from AMC. The Digital Elevation model (DEM) has been generated from Cartosat-1 stereo pair with 5 m spatial resolution.

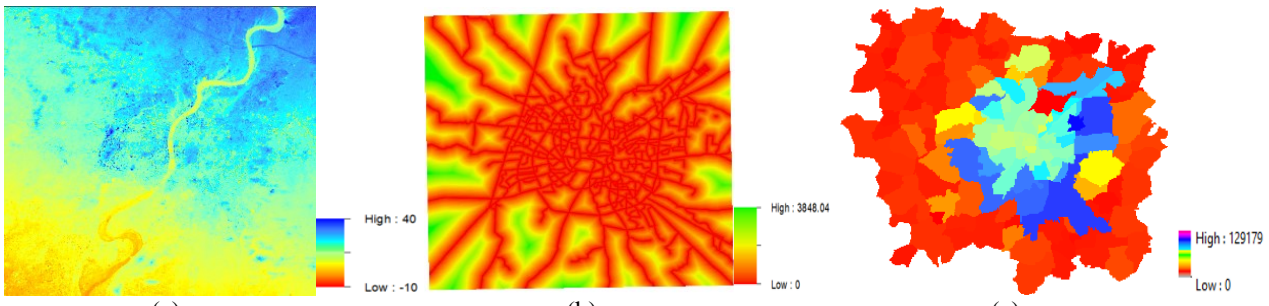

(a) (b) (c)

Figure 2: Auxiliary data used for urban growth modelling. (a) Slope (b) Proximity to road (c) Population density

4. Methodology

In this section, the essential characteristics of the integrated model are discussed (Figure 3.) First, the land use maps of 1992, 2005 and 2018 were produced using IRS data and temporal change in land use were evaluated. Second, the main driving force for urban expansion were investigated and trained by ANN for optimal network. Then the CA-MC model is applied for simulating urban growth. In order to verify the results, the land use map was validated as per the reference maps using kappa index. Finally, the model is used to simulate future land use maps of 2018 and 2032.The detailed description of models are following.

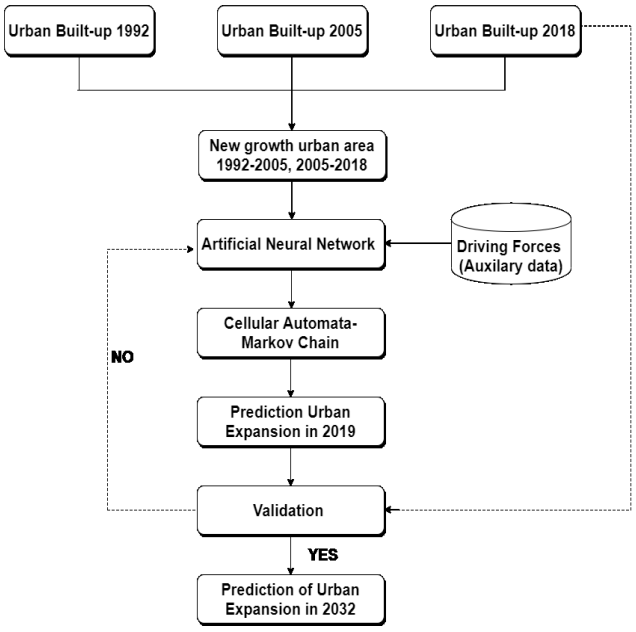

Figure 3: Flowchart of the ANN-CA-MC method in simulating urban expansion

4.1 Artificial Neural Network

Artificial Neural Networks (ANNs) are widely used for modelling with self-adapting, self-organizing, and self-learning abilities (Pijanowski et al., 2002; Park et al., 2011; Berberoğlu et al., 2016). The most frequently used and efficient feed-forward, error Back-Propagation Three-Layer Perceptron (BP-TLP) is adopted to simulate urban expansion owing to its simplicity, ease of training, and its abilities for reasonable associative memory and prediction (Rumelhart et al., 1986). The selected three-layer ANN is composed of an input layer, a hidden layer, and an output layer with 3 input nodes, 50 hidden nodes, and 2 output nodes (Figure 4). Each input node represents an independent variable and the number of hidden nodes significantly affects ANN performance (Hagan et al., 1996). Too few nodes will cause a significant prediction error, while too many will prolong the training process and lead to overfitting. In this study, the number of optimal hidden nodes was set to 50 by trial and error method. The selection of this number was based on model performance and network simplicity. The expected output has two possibilities of (1, 0) and (0, 1). The former indicates that the cell in question meets the expectation of conversion to urban, and the latter signifies non-urban cells. The network was trained stepwise iteratively with a targeted Root Mean Square Error (RMSE) of 0.001 between the model output and the reference data. However, reaching this RMSE threshold might cause overfitting, which was avoided by setting the number of training epochs to 500. These two parameters reduced the possibility of overfitting by early stopping. After an initial weight was assigned to each input variable, the ANN started to 'learn' from the training samples by adjusting the weights between neurons in response to the RMSE between the modelled output and the observed value. The training was terminated according to the targeted RMSE threshold, or the number of training epochs, whichever was reached first.

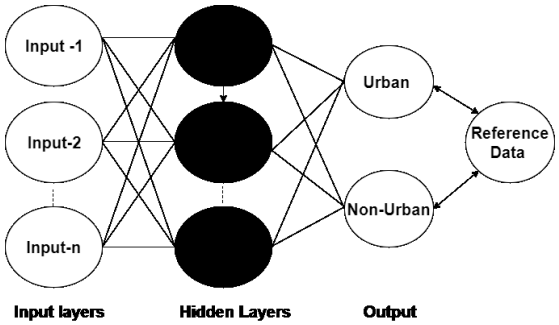

Figure 4: The architecture of the ANN adopted in this study.

4.2 Markov Chain-Cellular Automata

Markov chain is employed to predict the probability of urban land cover class change from one state to another by taking into account the past land cover change trend. Markov chain is a series of random values whose probabilities at a time interval depends on the value of the previous time (Surabuddin et al., 2013). Markov chains output describes as transitional probability matrix (equation 1):

$$p = \left(P_{ij}\right) = p11\ p12\ \ldots\ldots p1n \quad (1)$$
$$p21\ p22\ \ldots\ldots p2n$$
$$pn1\ pn2\ \ldots\ldots pnn$$

The probability of changes from (i^{th}) class into (j^{th}) class is described as a transformation probability (P_{ij}); n is the number of classes with the constraint below (equation 2). The transition probability matrix is a set of conditional probabilities for the cells in the model to go to a particular new state. (Akin et al., 2014)

$$0 \le P_{ij} \le 1\ (i, j = 1,2,3, \ldots\ldots, n)\ (2)$$
$$\sum_{i=1}^{n} P_{ij} = 1\ (i, j = 1,2,3, \ldots\ldots, n)$$

Markov chains model is obtained by (equation 3):

$$P(n) = P(n-1)P_{ij} \quad (3)$$

Where (n) is state probability of any times and $P(n-1)$ is preliminary state probability. Markov chain calculates probability of changes but does not represent the spatial explicit and location of changes. This limitation is fulfilled by combing with CA in order to minimise the weakness of the method. But for incorporating drivers of urban growth ANN is combined along with CA-MC model.

4.3 Accuracy Assessment

Accuracy test of urban growth model is an important part of the model whether the result of the model can be used by policy maker or not. Simulation and prediction techniques are ineffective and will have no scientific importance, if these techniques or models are not validated. Hence, the accuracy assessment of projected urban growth maps using validation methods is an extremely important step in urban growth modelling. The accuracy of the predicted land cover model was assessed using the kappa statistics. Overall accuracy and Kappa index are the most significant coefficients used to validate urban growth simulation (Yang et al., 2011; Al-sharif and Pradhan, 2013).

4.4 Model Implementation

The model was implemented as shown in figure 4. First, land cover maps in 1992, 2005 and 2018 were used to create two urban expansion maps (1992–2005, 2005–2018) through spatial overlay. Both transformed and untransformed samples were used as inputs to the ANN. Second, the ANN was cross-validated at least 500 times to optimize the selected calibration variables. The predicted result in 2018 was validated against the observed 2018 urban area using kappa index. With kappa value equal to 0.94 and mean square error as 0.083, the trained model indicates reasonable results comparison to other random allocation, this particular model was then applied to predict urban expansion in 2032. After the model passed the validation assessment, it was used to simulate urban area in 2032 with the land cover in 2018 as the baseline scenario under the assumption that future urban expansion would behave identically to what had occurred in the past. CA-MC model was applied to create the projection of 2018 land cover based on 2005 and 1992 land cover and projected model is being evaluated with kappa statistics based on reference image.

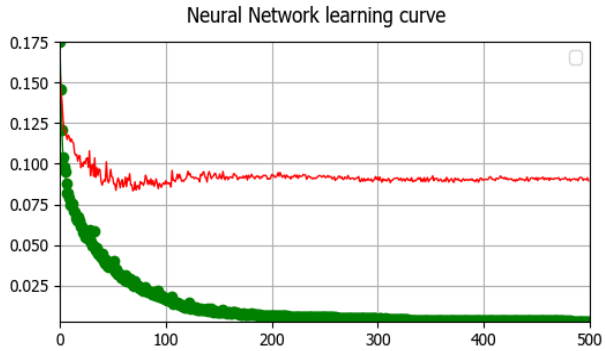

Figure 5: Optimised neural network adopted learning curve and loss function with learning curve (red) and loss function curve (green).

5. Results

The urban built-up has increased significantly between 1992, 2005, 2018 (Table 1 and Figure 6). It has indeed increased by 36% in past 27 years. Built-up area increased from 146.67 km^2 in 1992 to 193.82 km^2 in 2005 and 230 km^2 in 2018. The increase in built-up area can be attributed to the population growth and settlement expansion, these scenarios had culminated into conversion of natural vegetation and open spaces to built-up areas. Based on the rate of change between 1992 and 2018, the predicted urban built-up areas revealed that by 2032, built up area would increase to 275.76 km^2 in 2032. This is increase of 19.5 % of urban built-up area. The simulated results show that the increase in built-up area are closely associated with the existing built-up areas. Urban sprawl has mostly occurred in north-west and south-west part, it has attracted many automobiles industries and builders for construction of new housing colonies, hence there is low-density urban sprawl on the city's western periphery. The projected urban growth in 2032 indicates in future more industries and housing societies will come to this place making it denser (Figure 7). The growth in this area is attributable to population growth and also people shifting from the interior of city to the outskirts' due to inflation of price of land and denser built-up surrounding with less green spaces and more polluted air.

Table 1 Change in built-up area during (1992-2018)

Land cover	1992 Area (km^2)	2005 Area (km^2)	2018 Area (km^2)
Urban	146.67	193.82	230.0
Non-Urban	574.14	526.99	491.29

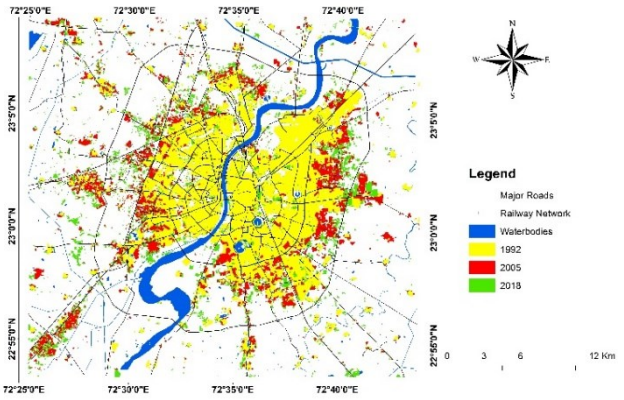

Figure 6: Urban Built-Up Change during (1992-2005) and (2005-2018) period

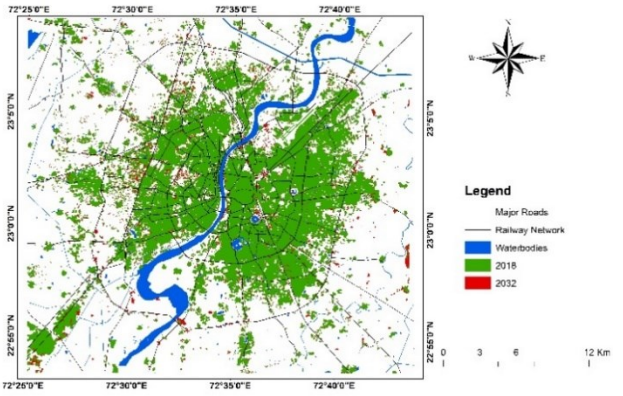

Figure 7: Predicted urban growth in 2032 and existing 2018 urban area for Ahmedabad city.

6. Conclusions

At global level, urban sprawl has become a challenge for sustainable development in cities and it has negative impact on environment as well as human society. Urban

built-up growth has increased by 36% from 1992 to 2018 in Ahmedabad and if this trend continues, the other land cover classes such as agricultural land, vacant land will be changing to built-up areas. The validation results demonstrate the possibility of using machine learning, such as ANN, to improve the capability of CA-MC simulation of urban expansion. In the simulation, the ANN plays the most important role for incorporating the relationship between the urban growth and socio-economic variables affecting urban expansion. It is predicted that urban areas will increase to 275.76 km^2 by 2032. The predicted result from this model shows that newly urbanized areas in 2032 are based on the urban growth in the past. The most affected regions for future urban growth will be western part of Ahmedabad. Overall, this model can be used to provide relevant and useful information for urban planners and local government decision makers.

Acknowledgements

The author would like to thank Shri D.K. Das, Director, Space Applications Centre for the Institutional support and encouragement during the course of the study. We would like to express our sincere gratitude to Dr. Raj Kumar, DD, EPSA and Dr. Markand Oza, Head, CGDD, Space Applications Centre for their valuable comments and encouragement.

References

Aburas, M.M., Y.M. Ho., Mohammad F.R., and Z.H Ashaari (2016). The simulation and prediction of spatio-temporal urban growth trends using cellular automata models: a review, International Journal of Applied Earth Observation and Geoinformation, 52, 380–389. doi: 10.1016/j.jag.2016.07.007.

Akin A., S. Aliffi, and F. Sunar (2014). Spatio-temporal urban change analysis and the ecological threats concerning the third bridge in Istanbul City, Int. Arch Photogramm Remote Sensing Spat Inf SCI 40 (7), 9.

AMC (2006). City Development Plan Ahmedabad 2006-2016. Ahmedabad Municipal Corporation, Ahmedabad.

Al-sharif, A.A.A., and B. Pradhan (2013). Urban sprawl analysis of Tripoli metropolitan city (Libya) using remote sensing data and multivariate logistic regression model, Journal of the Indian Society of Remote Sensing, 42(1), 149–163.

Arsanjani, J.J., M. Helbich, W. Kainz, and A.D. Boloorani (2013). Integration of logistic regression, Markov chain and cellular automata models to simulate urban expansion, International Journal of Applied Earth Observation and Geoinformation, 21, 265–275.
doi: 10.1016/j.jag.2011.12.014.

Batty, M., Y. Xie, and Z. Sun (1999). Modelling urban dynamics through GIS-based cellular automata, Computers, Environment and Urban Systems, 23 (3), 205–233. doi:10.1016/S01989715(99)00015-0.

Berberoğlu, S., A. Akin, and K.C. Clarke (2016). Cellular automata modelling approaches to forecast urban growth for adana, Turkey: a comparative approach, Landscape and Urban Planning, 153, 11–27.
doi: 10.1016/j.landurbplan.2016.04.017

Bihamta, N., A. Soffianian., S. Fakheran. and M Gholamalifard. (2015). Using the SLEUTH urban growth model to simulate future urban expansion of the Isfahan metropolitan area, Iran, Journal of the Indian Society of Remote Sensing, 43 (2), 407–414. doi:10.1007/s12524-014-0402-8.

Clarke, K.C., S. Hoppen, and L. Gaydos (1997). A self-modifying cellular automaton model of historical urbanization in the San Francisco Bay area, Environment and Planning B: Planning and Design, 24 (2), 247–261.doi:10.1068/b240247.

Jain, G.V. and S.A. Sharma (2019). Spatio-temporal analysis of urban growth in selected small, medium and large Indian cities, Geocarto International,34:8,887-908, DOI:10.1080/10106049.2018.1450450

Jiang, B. and X. Yao (2010). Geospatial Analysis and Modelling of Urban Structure and Dynamics. Springer, Dordrecht, The Netherlands, ISBN 9048185718.

Jat, M.K., M. Choudhary, and A. Saxena, (2017). Application of geo-spatial techniques and cellular automata for modelling urban growth of a heterogeneous fringe, The Egyptian Journal of Remote Sensing and Space Science, 223-241, doi:10.1016/j.ejrs.2017.02.002

Hagan, M.T., H.B Demuth, and M.H. Beale (1996). Neural network design. Boston, MA: PWS Publishing.

Li, X., Y. Chen, X. Liu, X. Xu, and G. Chen (2017). Experiences and issues of using cellular automata for assisting urban and regional planning in China, International Journal of Geographical Information Science, 31 (8), 1606–1629.
doi:10.1080/13658816.2017.1301457.

Liu, Y. (2012). Modelling sustainable urban growth in a rapidly urbanising region using a fuzzy-constrained cellular automata approach, International Journal of Geographical Information Science, 26 (1), 151–167.
doi:10.1080/13658816.2011.577434.

Li, X. and A.G.O. Yeh (2000). Modelling sustainable urban development by the integration of constrained cellular automata and GIS, International Journal of Geographical Information Science, 14 (2), 131–152.
doi:10.1080/136588100240886.

Mustafa, A., M. Cools, I. Saadi, and J. Teller (2017). Coupling agent-based, cellular automata and logistic regression into a hybrid urban expansion model (HUEM), Land Use Policy, 69 (Supplement C), 529–540.
doi: 10.1016/j.landusepol.2017.10.009.

Park, S., S. Jeon, S. Kim, and C. Choi (2011). Prediction and comparison of urban growth by land suitability index mapping using GIS and RS in South Korea, Landscape and Urban Planning, 99 (2), 104–114. doi:10.1016/j. landurbplan.2010.09.001.

Pijanowski, B.C., D.G. Brown, B.A. Shellito, and G.A., Manik (2002). Using neural networks and GIS to forecast land use changes: a land transformation model, Computers, Environment and Urban Systems, 26 (6), 553–575. doi:10.1016/ S0198-9715(01)00015-1.

Rumelhart, D., G. Hinton, and R. Williams (1986). Learning internal representations by error propagation. In: D.E. Rumelhart and J.L. McClelland, eds. Parallel distributed processing: explorations in the microstructures of cognition. Vol. 1, Cambridge: MIT Press, 318–362.

Santé, I., A.M. Garcia, and R. Crecente (2010). Cellular automata models for the simulation of real-world urban processes: a review and analysis. Landscape and Urban Planning, 96 (2), 108–122.

Sudhira, H.S., T.V. Ramachandra, and K.S. Jagadish (2004). Urban sprawl: metrics, dynamics and modelling using GIS, International Journal of Applied Earth Observation and Geoinformation, 5 (1), 29–39. doi:10.1016/j. jag.2003.08.002.

Surabbuddin, M.M., N. Sharma, M. Kappas, and P.K. Garg (2013). Modelling of spatio-temporal dynamics of land use and land cover of Brahmaputra river basin using geoinformatics techniques. Geocarto Int 28(7), 632-656.

Wang, H., S. He, X. Liu, L. Dai, P. Pan, S. Hong, and W. Zhang (2013). Simulating urban expansion using a cloud-based cellular automata model: A case study of Jiangxia, Wuhan, China. Landscape and Urban Planning,110,99–112.doi: 10.1016/j.landurbplan.2012.10.016.

Xu.T., J. Gao, and G. Coco (2019). Simulation of urban expansion via integrating artificial neural network with Markov chain – cellular automata, International Journal of Geographical Information Science, 33(10), 1960–1983 https://doi.org/10.1080/13658816.2019.1600701

Yang, W., F. Li, R. Wang, and D. Hu (2011). Ecological benefits assessment and spatial modelling of urban ecosystem for controlling urban sprawl in Eastern Beijing, China, Ecological Complexity, 8 (2), 153–160. doi: 10.1016/j.ecocom.2011.01.004.

Zhang, H., X. Jin, L. Wang, Y. Zhou and B. Shu (2015). Multi-agent based modelling of spatiotemporal dynamical urban growth in developing countries: simulating future scenarios of Lianyungang city, China, Stochastic Environmental Research and Risk Assessment, 29 (1), 63–78. doi:10.1007/s00477-014-0942-z.

Journal of Geomatics Vol. 14, No.1, April 2020

Mapping of crime incidences and hotspot analysis through incremental auto correlation – A case study of Shillong city, Meghalaya, India

Dibyajyoti Chutia*, Manali Santra, Nilay Nishant, P Subhash Singh, Avinash Chouhan and P.L.N. Raju
North Eastern Space Applications Centre, Department of Space, Government of India,
Umiam, Shillong, Meghalaya, India- 793103
Email: d.chutia@nesac.gov.in

(Received: Feb 14, 2020; in final form: June 30, 2020)

Abstract: The mapping of crime incidents in the spatio-temporal domain is one of the vital components to take up more decisive steps to minimize crime incidents. Distribution of crime incidents is not accidental as they occur due to the various socio-economic as well as environmental conditions. It has been reported that crime rates are rising frighteningly in developing countries. In India, several studies on the analysis of crime patterns, trends, and the causes have been carried out with the inputs from geospatial technology. There is no detailed study on the analysis of crime hotspots using spatio-statistical techniques for the Shillong city of Meghalaya, India. The main objective of this work is to determine the pattern of crime hotspots during different time frames for the Shillong city using the incremental spatial autocorrelation method. Three years of crime incident data (2014-2016) comprising of more than 4515 incidents were analyzed and categorized mainly in 5 major types such as house trespassing, murder, crimes against women, theft, and cheating related charges. The intensity of the spatial clustering of the crime incidents were obtained effectively by the *z*-score measured by increasing the distance band or threshold distance, which helped to understand the spatial distribution of crime incidents with a higher degree of confidence level. It was observed that the hotspots were primarily confined to the central part of the city and some of the hotspots (average) were unevenly distributed over space irrespective of the size of the population density. The crime against women were reported mostly during the evening and the highest theft were reported after 2200 hrs during night. Other crime cases were not observed with any specific pattern concerning the time of occurrences.

Keywords: Spatial autocorrelation, spatial distribution, spatial clustering, hotspots

1. Introduction

The crime rates are increasing alarmingly in all the developing countries due to various reasons like poor social, political, economic, and environmental conditions. The distribution of the crime incidents is not random since these are human phenomena only. “For incidents to occur, offenders and their targets – the victims and or property – are required to exist at the same location for a period of time” (Akpinar, 2005). The spatial distribution of crime is considered to be related to a variety of socio economic and crime opportunity factors (Wang et al., 2013). Crime is not something that goes away easily. Actions must be taken to reduce crime incidents for crime prevention. One important step for crime prevention is to analyze the current situation like determining areas of high crime concentration, which of the crimes are occurring more frequently than other crimes, but a big volume of crime data has made the process of analyzing crimes difficult (Nasridinov and Young-Ho, 2014). Analyzing the crime pattern and controlling it using various techniques has become possible using spatial information technology. The whole dynamics of crime analysis and mapping has started changing with new technologies. The traditional method of maintaining criminal records has become obsolete. It is not adequate for the requirements of today’s crime scenarios. It does not provide an accurate, reliable solution for decision support. It does not provide real-time data required for quick decision support. The law enforcing authorities previously faced a very hard situation, controlling the crime, as they had very limited resources compared to resources, which modern crime fighters’ use now a day. The solution to this increasing problem is to make meaningful utilization of information technology with the understanding of spatial patterns of crime incidences.

Geospatial technology with new methods and tools can play vital role in the mapping and analysis of crime. It supports better synoptic perspective to crime study, analysis, mapping, proactive decision making and prevention of crime (Balogun et al., 2014). Mapping of crime and related factors that affect the safety of people can be helpful to police for protecting citizens and are also used to raise people’s awareness regarding the dangerous locations (Tahani et al., 2015). The locations where crimes most commonly occur can easily be visualized by mapping and based on that resources can be effectively utilised. It can empower the law and enforcement agents with the analysis and visualization of the crime patterns, help understand relationship among different crime events and predict future crime incidents. It can be used to further identify factors contributing to crime, and thus allow police to proactively respond to the situations before they become problematic (Thangavelu et al., 2013). Danny (2015) presented a geospatial approach for crime mapping and attendant management in the enhancement of tight security using time series analysis in Asaba, Delta State, Nigeria. Jorge et al., (2012) combines statistical methods and spatial models to strengthen the Intelligence-Led Policing (ILP) methods to provide the necessary tools for Decision Support System (DSS) of police departments. On the other hand, in other few studies, spatial statistics were employed to quantify the relationship between features of the remote sensing images and crime events on the ground, and these analyses may be particularly useful as input to policy

decisions about policing within the community (Chen et al., 2015). A study on crime was reported to identify the spatio-temporal pattern in Dala L.G.A of Kano State, Nigeria (Mohammed and Salihu, 2013). Recently one study has used a density map of crimes with kernel method to predict the burglary crimes based on current situation (Gamze et al., 2018). It was concluded that it could be applied for other security and intelligence related applications. On the other hand, another study (Kounadi et al., 2018) developed population models to depict the spatial distribution of people who have a heightened crime risk for burglaries and robberies. This was reported very effective for carrying out crime analysis more precisely and which can provide accurate information about crime rates to the public. In a study by Snyders et al., 2018 carried out in two neighborhoods, Queenswood and Kilner Park, in the north-east of the City of Tshwane of South Africa on the specific crime patterns and fear of crime, it was concluded that the use and avoidance of places in the neighborhood do not always relate to the local crime hot-spots.

Identification of crime hot-spot in the spatial domain is one of the important aspects of crime mapping and analysis to take up more decisive steps to minimize crime incidents. A number of studies have been conducted on the crime hotspot analysis (Jaishankar et al., 2009; Kumar et al., 2012; Ansari and Kale, 2014; Saravanakumar and Revathy, 2016; Achuand Suja Rose, 2016; Ahmad et al., 2018). Achuand Suja Rose (2016) presented hotspot analysis where Moran'sindex (*m*) test statistic of spatial autocorrelation has been done prior to Getis-Ord *Gi** hotspot analysis to find out the clustering pattern as well as the outliers in the data. Recently, an effective crime analysis was reported where Voronoi diagrams (VDs) were employed in spatial analysis (Melo de et al., 2017; Melo de et al., 2018). It was found to recognize crime patters associated with crime concentration, crime along pathways, and the highly regularized distribution of crime in spatially limited areas. CrimeStat was another spatial statistical program for the analysis of crime incident locations (Levine, 2017). It can interface with most desktop GIS programs to provide hotspot analysis as well as other statistical tools. This was mainly used to assist the law enforcement agencies and criminal justice researchers in their crime mapping efforts.

Most of the hotspot analysis studies have been conducted based on the spatial autocorrelation of the crime incidents considering the fixed threshold distance. It affects the intensity of the spatial clustering and sometimes provides poor spatial autocorrelation. In this work, incremental spatial autocorrelation was employed to address this issue more effectively to find a better correlation among the hotspots with the higher *z*-score. The *z*-score is the measurement of the standard deviation which implies how the dataset dispersed from the average value. The *p* or probability value determines if the observed spatial pattern is the outcome of the random event (higher *p-value*) or it has some statistical significance (lower *p-value*). A higher *z*-score and smaller *p*-value of a feature specify spatial clustering of a higher degree. A number of studies on crime have been done using Geomatics worldwide including India. Perspective view on crime mapping was effectively presented using multi-temporal data of crime for a few major cities of India (Ahmad et al., 2017). This can help in assessing the crime trends in the spatial domain. A similar study was done by Ahmad et al. (2018) using geospatial technology for the Jharkhand state of India to understand the crime trend. Crime GIS was implemented for Chennai city policing to strengthen the policing the activity with the spatial crime analysis tool (Jaishankar et al., 2009). A number of spatial platforms have been developed for the operational activity of crime for better management. However, there is lack of detailed study for understanding crime hot-spots in the North-Eastern part of India till now. The present work has following major objectives-

a. Hotspot analysis using incremental spatial autocorrelation on temporal crime incidents reported during last the three years.
b. Understanding the type of reported crimes incidents occurred during different times of the day.
c. Understanding the pattern of crime hotspots over population density.

2. Study area

Shillong known as Scotland of India is a hill station and the State capital of Meghalaya. It is also the district Head Quarters of East Khasi Hills of Meghalaya situated at an average altitude of 1500m above mean sea level. Shillong is spread around 64.36 square km with a population of 143,229 according to Census 2011 with an average sex ratio of 1042. Shillong city is divided into 27 wards under a Municipal board with 7 police stations. Shillong is well connected by roads with all major North Eastern States of India. National Highway 40 is the lifeline of the city as it connects Shillong with Guwahati, the gateway of North Eastern States. Another National Highway 44 connects the city with Tripura and Mizoram and touches the International border with Bangladesh. The study area with the ward boundary and location of police stations overlaid on the Cartosat-1 satellite imagery is depicted in figure 1.

Recent crime statistics have shown that despite being a popular tourist destination in North East India, Shillong has a high crime rate. Although the employment ratio and literacy rate are higher in the city area, the outskirts of the city are still facing lower employment status with low literary rate. In the past few years, trespassing, murder, crimes against women, theft and cheatingrate are rising. The location of crime incidents occurred during 2014-2016 overlaid with the location of police stations and ward boundary are depicted in figure 2 and year-wise details given in figure 3.

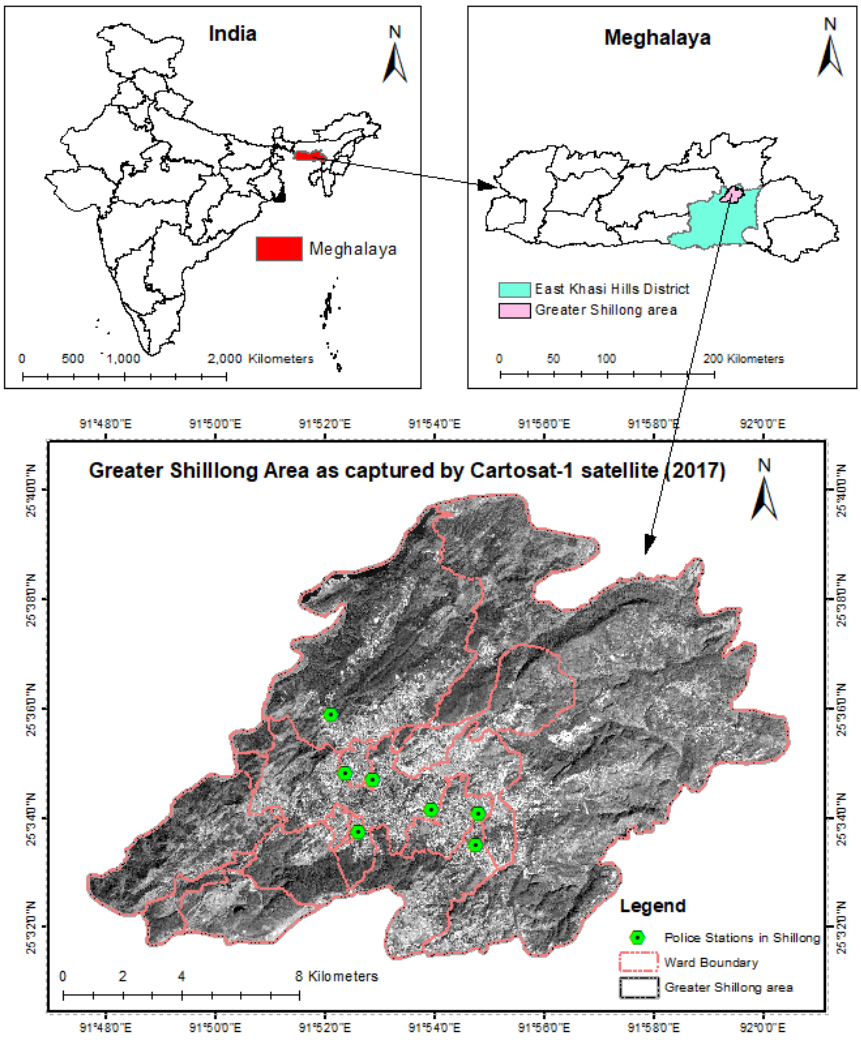

Figure 1: Shillong area as viewed by Cartosat-1 satellite data

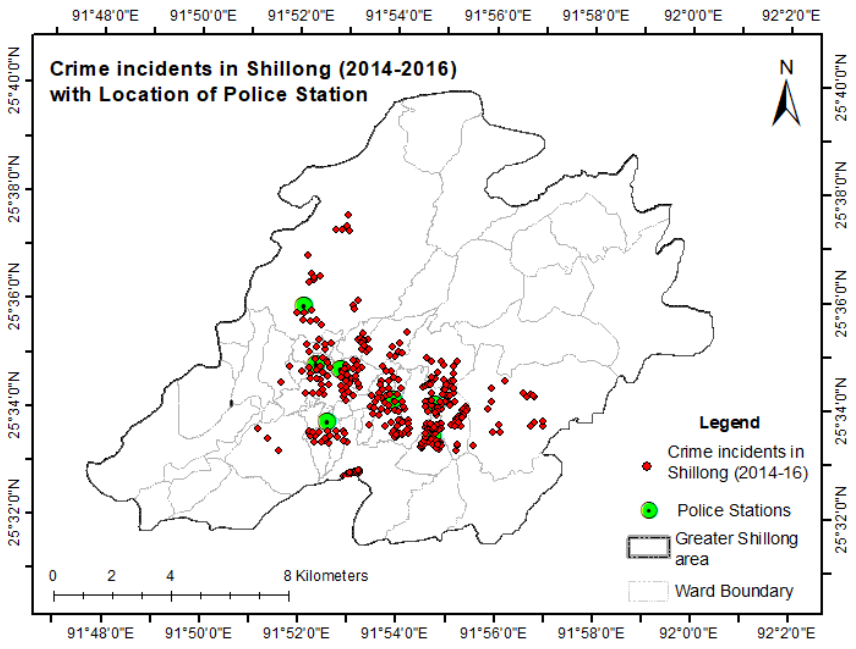

Figure 2: Location of crime incidents occurred during 2014-2016

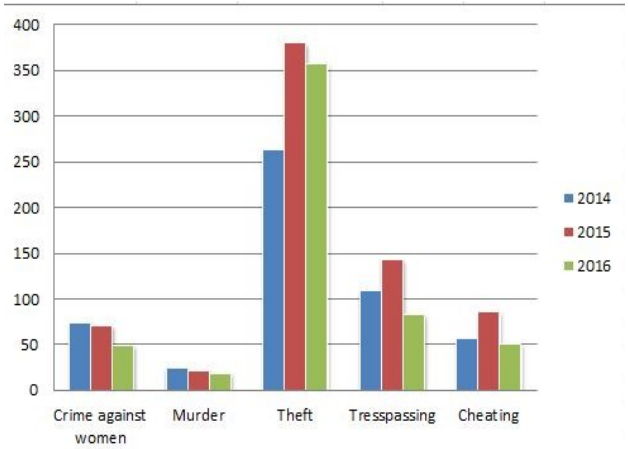

Figure 3: Category wise distribution of crime in three years (2014-2016)

However, Shillong is also known as a safer place for visit among all the tourist places of NE States. Increasing crime rate can hamper the lives of the common people as well as the tourist business. Security system from any place signifies the overall growth and prosperity. So the policing system must be organized and resourceful for good management of crime monitoring. To strengthen the police resource system and analyzing the current crime patterns in the city, we have selected Shillong as our study area

3. Data and Methodology

3.1 Datasets used

Crime incident comprised of 4515 records reported during the last three years 2014-2016 collected from the concerned Authority of the District Administration for analysis. Various crimes registered under the police stations under the Indian Penal Code (IPC) have been categorized in 5 major types in trespassing, murder, crimes against women, theft, and cheating. Existing base map such as roads, settlements as per census 2011 has been overlaid along with administrative GIS data, such as the ward boundary of Shillong city and police stations for better visualization and interpretation of crime incidents, already generated by North Eastern Space Applications Centre, Department of Space, Government of India, Umiam-Shillong, Meghalaya, India.

3.2 Preprocessing of crime incident data

Crime incident records received from the concerned authority comprises of spatially distributed point data. As the crime data have shown that multiple incidents have occurred within a short distance of one another, so the intensity of the crime incidents at every single location was measured by the Integrate and Collect event tool of ArcGIS 10.1 software:

Integrate – To snap features within a specified distance or given X, Y tolerance of each other and makes those features coincident or identical. It performs the followings task (ESRI Tool reference):

- Vertices lying within the X, Y tolerance of one another will be assigned the same coordinate location.
- When a vertex of one feature is within the X, Y tolerance of an edge of any other feature, a new vertex will be added on the edge.
- When line segments intersect, a vertex will be added at the point of intersection for each feature involved in the intersection.

It is recommended not to use high tolerance value as it may delete a number of polygons or lines which in turn may not produce good results The choice of value for the X, Y tolerance is critical. This tolerance value can be determined based on the characteristics of the crime data; how densely incident locations are spatially located. After analyzing the three years data with different ranges of the X, Y tolerance, it was observed that the optimal range of X, Y tolerance lies between 200m to 270m as the crime incidents records are comprised of spatially distributed point data.

Collect Event – Integrated crime incident points resulted in the previous step were used for the operation of collect event. It creates the incident points to a set of weighted point data by creating a new feature dataset of the previous one with an additional field to indicate the number of incidents at each location within a specified snapping distance.

3.3 Methodology

The proposed methodology is based on spatial statistical analysis. Simple interpolation tools like inverse distance weighted (IDW) and natural neighbor interpolation may not help in hotspot analysis of crime as they can only estimate the resultant surfaces without statistical significance. Similarly, interpolation techniques like spline and trend are not suitable for hotspot analysis. Statistical interpolation technique like Kriging is well established in geostatistics, however, this has been found suitable for the study related to soil or geology where there is a big gap between the samples and there is a spatially correlated distance or directional bias in the data (Deshmukh and Anappa, 2018).

The proposed method is composed of two parts, i.e. i) Incremental spatial autocorrelation using Moran's index (Moran 1950), ii) Hotspot analysis using Getis-Ord Gi* (Getis and Ord, 1992). Appropriateness of the both techniques in the context of crime analysis are illustrated below with statistical details.

i) Incremental Spatial autocorrelation: It measures the correlation of a feature expressed in clustered or dispersed. The strength of the correlation is determined at different distances where the clusters are prominently formed. Statistically significant peak positive z-score indicates distances where spatial processes promoting clustering are most pronounced. It can be computed using Moran's index (m) (Saravanakumar and Revathy 2016) which can be defined as follows:

$$m = \frac{n}{A_0}\frac{\sum_{i=1}^{n}\sum_{j=1}^{n} w_{i,j}z_i z_j}{\sum_{i=1}^{n} z_i^2} \quad (1)$$

Where z_i is the deviation of an attribute for feature m from its mean $(x_i - X)$, $w_{i,j}$is the spatial weight between feature m and j, n is equal to the total number of features, and A_0 is the aggregation of all the spatial weights.

$$A_0 = \sum_{i=1}^{n}\sum_{j=1}^{n} w_{i,j} \quad (2)$$

The z_m -score for the statistic is computed as:

$$z_{Im} = \frac{m - E[m]}{\sqrt{V[m]}} \quad (3)$$

where, $E[m] = -1/(n-1)$ is the expected value under the null hypothesis with no spatial clustering and $V[m]$is the variance which measures variability of the numbers from their mean value which can be computed as

$$V[m] = E[m^2] - E[m]^2 \quad (4)$$

The distance is one of the important criteria for receiving better results in hotspot analysis. It must ensure that all the spatially distributed incident points should have at least one neighbor. It is difficult to approximate the reliable set of neighbors for each incident point without defining the appropriate distance threshold between them. That is why; it has been suggested to use incremental autocorrelation in hotspot analysis where the intensity of spatial clustering of crime incidents is obtained effectively by the *z*-score measured by increasing the distance band or threshold distance. The distance corresponding to the higher *z*-score obtained at the peak is treated as a threshold distance for hotspot analysis as it reflects the more accurate formation of the cluster.

ii) Hotspot Analysis using Getis-Ord G_i*: Based on the threshold distance defined in the equations (Eq.1-Eq. 4), hotspot analysis indicates the locations with statistically significant hotspots and cold spots in the aggregated data that are within a proximate region on a calculated distance. It needs clustering in the data and returns *z*-score to indicate whether any clustering is present or not in the data. It creates clusters of features with similarly high or similar low values in the cluster. For a significant hotspot, *z*-score should be high and probability (*p*-value) should be low. On other hand, negative, low *z*-score with small probability value indicate a coldspot.

Here, Getis-Ord G_i* statistics is used to identify statistically significant hotspot or coldspots from a set of weighted features and can be defined as

$$G_i^* = \frac{\sum_{j=1}^{n} w_{i,j}\, x_{i,j} - \overline{X}\sum_{j=1}^{n} w_{i,j}}{S\sqrt{\frac{[\, n\sum_{j=1}^{n} w_{i,j}^2 - (\sum_{j=1}^{n} w_{i,j})^2\,]}{n-1}}} \quad (5)$$

where x_j is the attribute value for feature j,$w_{i,j}$ is the spatial weight between feature i, and j, and n is equal to the total number of features and:

$$\overline{X} = \frac{\sum_{j=1}^{n} x_j}{n} \quad (6)$$

$$S = \sqrt{\frac{\sum_{j=1}^{n} x_j^2}{n} - (\overline{X})^2} \quad (7)$$

The final outcome of the G_i* method is a feature dataset containing the cluster of hotspots and coldspots of crime incidents with corresponding G_iZ-score and G_iP-value. The higher the G_iZ-score, clustering of features with high value become more intense which creates the statistically significant hotspots as well as smaller the statistically significant negative *z*-score, clusters of features surrounded by lower values become prominent which is referred as cold spots.

In most of the experimental instances of hotspot analysis, it was observed that the hotspots are defined by hard boundary based on the statistical significance of the cluster. However, some of the important neighboring incidents are not represented in the hotspots. Spatial interpolation technique can address this issue by predicting such incidents based on the G_iZ-score. Here the IDW method is used to interpolate the hotspots and coldspots points for better representation in spatial domain. It assumes the prediction surface which is more influenced by the nearby points than the points in the distant location. The cell size of the output raster is calculated from the shorter of the width or height of the study area extent divided by 250, where the extent is in the output coordinate system specified in the environment.

4. Results and Discussion

Hotspot analysis on crime incidents is reported based on the two spatial statistical methods; spatial autocorrelation using Moran's index (*m)* to measure the correlation of crime incidents expressed in clustered or dispersed and Getis-Ord G_i* statistics to indicate the significance of hotspots or coldspots. Considering the spatial distribution of the crime incidents over a typical topographical terrain like Shillong city of Meghalaya spatial correlation was computed based on the incremental distances to find out the threshold optimal distance with a higher z-score which is required for the best results from Getis-Ord G_i* statistics.

4.1 Statistical analysis on crime hotspots

In this study, three years of crime incident data (2014-2016) comprising of more than 4515 incidents are analyzed and categorized mainly in 5 major types, such as trespassing, murder, crimes against women, theft, and cheating. The analysis was also done for each of the years to see the crime pattern from 2014 to 2016. The *z*-score achieved at different distances during the incremental spatial autocorrelation of three years data was plotted in figure 4. It was observed that the peak *z*-score (= 4.7)

was achieved at a distance of 1500m. The *z*- score achieved at different distances are also given in figure 4.

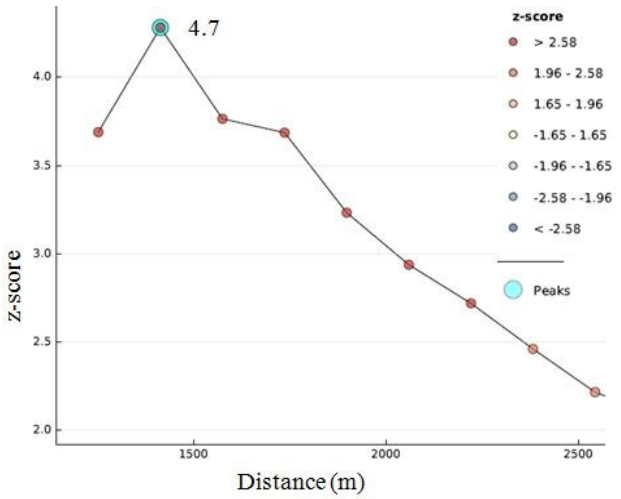

Figure 4: The peak *z*-score resulted at a distance of 1500m during incremental spatial autocorrelation

Similarly; we have achieved a *z*-score of 4.2 for 2014 crime incidents, 5.1 for 2015, and 4.5 for 2016 crime incidents. In all the cases, only one statistically significant peak was observed. These threshold distances are an important input to the hotspot analysis. The resultant G_iZ-scores and G_iP-values in Getis-Ord G_i* represent whether crime incidents are with either high or low-value cluster spatially. The highest and lowest scores of G_iZ achieved for four sets of crime incident data, i.e. incident records of 2014, 2015, and 2016 and three years combined (2014-2016) datasets are given in table 1**.** It is observed that G_iZ score was found higher in the hotspot analysis of combined 3 years data with 3.68 as compared to the other yearly recorded crime incident datasets. However, an incident with a higher GiZ score may not form statistically significant hotspots unless it is surrounded by other incidents with higher values. *Z*-scores are representing these standard deviations where very high or very low (negative) values are associated with very small *p*-value (probability). The *p*-value against each of the G_iZ-scores with less than or equal to 0.05 contributes statistically significant hotspots with more than 95 % confidence level. Hotspots in the form of crime density using IDW interpolation based on the G_iZ score is presented in figure 4 for the crime incidents record of 2014. Similarly, crime Hotspot analysis was carried out for the year 2015, 2016, and three years combined datasets are presented in figures 4-6.Here, hotspots are analyzed for each and every year separately and combined. From all the figures it was observed that the crime hotspot coverage (represented in red color in the figures) is comparatively higher in 2014 with minimal coldspots coverage represented in blue color. It is prominent that some of the hotspot areas in 2014 became the crime hotspots of average density in 2015 and again changed in 2016. Though in the year 2015; the crime occurrence rate was higher than the other two years, some areas faced more frequent crimes than other parts of the study area. Because of that, the yellow marked areas of 2015 have shown some visual changes when compared with 2014 and 2016 figures. These yellow marked areas in crime map of 2015 inference that other than the central city, crimes happened in the outer zone are statistically insignificant.

However, the pattern of crime density of 2014 (Figure 5) has a similarity with 2016 (Figure 7). On the other hand, the pattern of crime density of the year 2015 (Figure 6) does not have much similarity with 2014 and 2016 crime maps. Figure 6 indicates that most of the crime incidents occurred in the central part of the city during the year 2015 as compared to the years 2014 and 2016. Figure 8 indicates that crime risk zones generated from all three years of data of the study area. It was observed that the hotspots were also confined in the central part of the Shillong, and this was contributed by the crime incidents taken place during the year 2015. On the other hand, a large number of distinct cold spots are also noticed in most of the instances while hotspots analysis was carried out for all the years' together (Figure 9).

Table 1: Getis-Ord G_i* statistics achieved on different crime incident datasets against threshold distances

Serial No	Crime incident datasets	Number of incidents	G_iZ-score		G_iP-value	Threshold distance (m)
			High	Low		
1	Incidents of 2014	1083	2.71605	-1.2908	0.000600	1456
2	Incidents of 2015	2195	2.85133	-1.3585	0.000081	1205
3	Incidents of 2016	1245	3.41776	-1.63274	0.000014	1649
4	Incidents of 2014-16	4523	3.68501	-1.58792	0.000230	1500

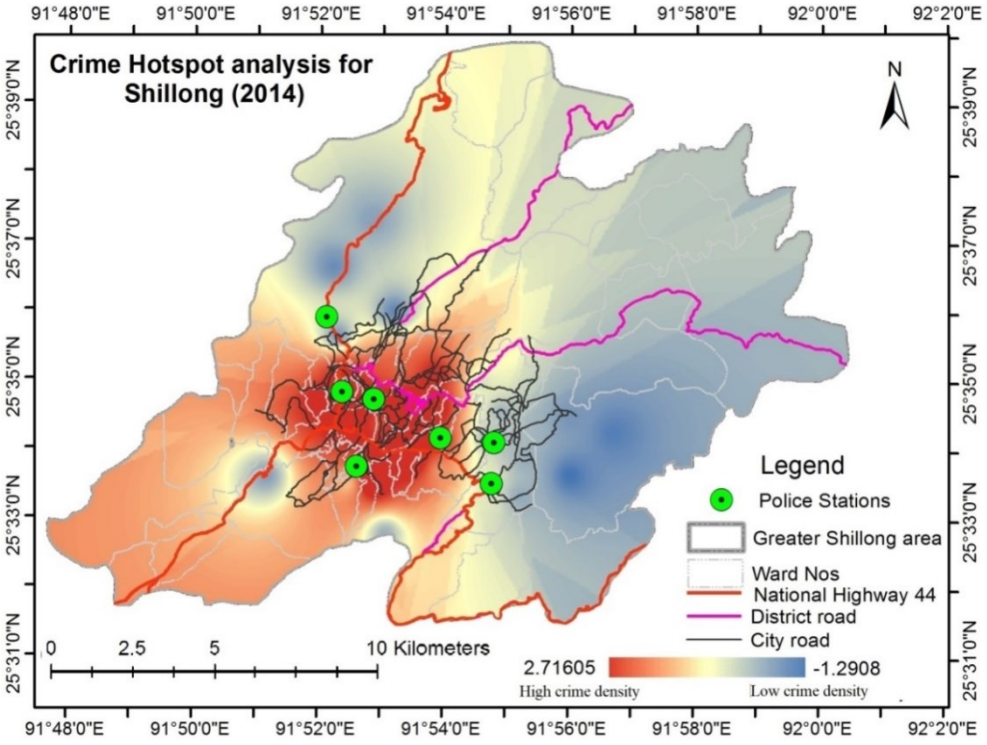

Figure 5: Hotspot in the form of crime density for 2014 crime incident dataset of Shillong city

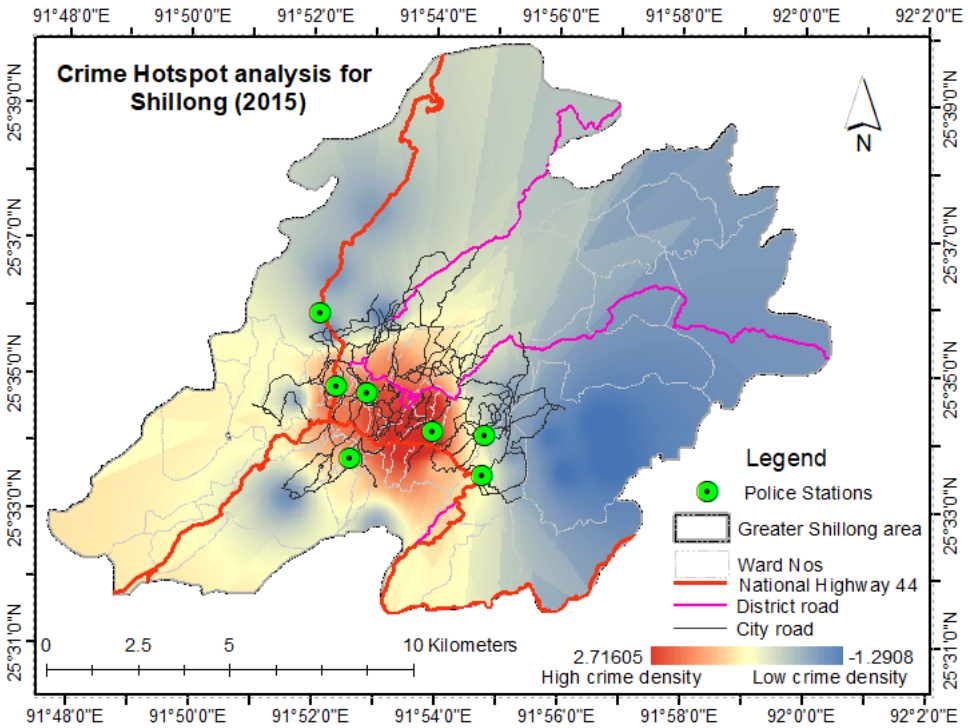

Figure 6: Hotspot in the form of crime density for 2015 crime incident dataset of Shillong city

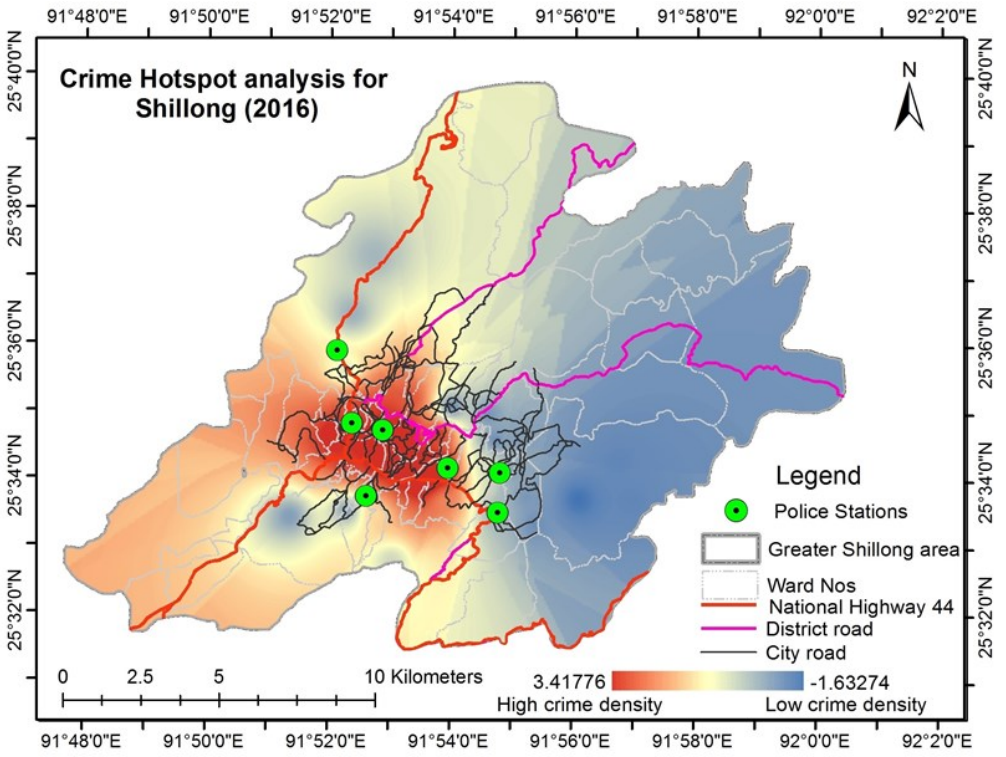

Figure 7: Hotspot in the form of crime density for 2016 crime incident dataset of Shillong city

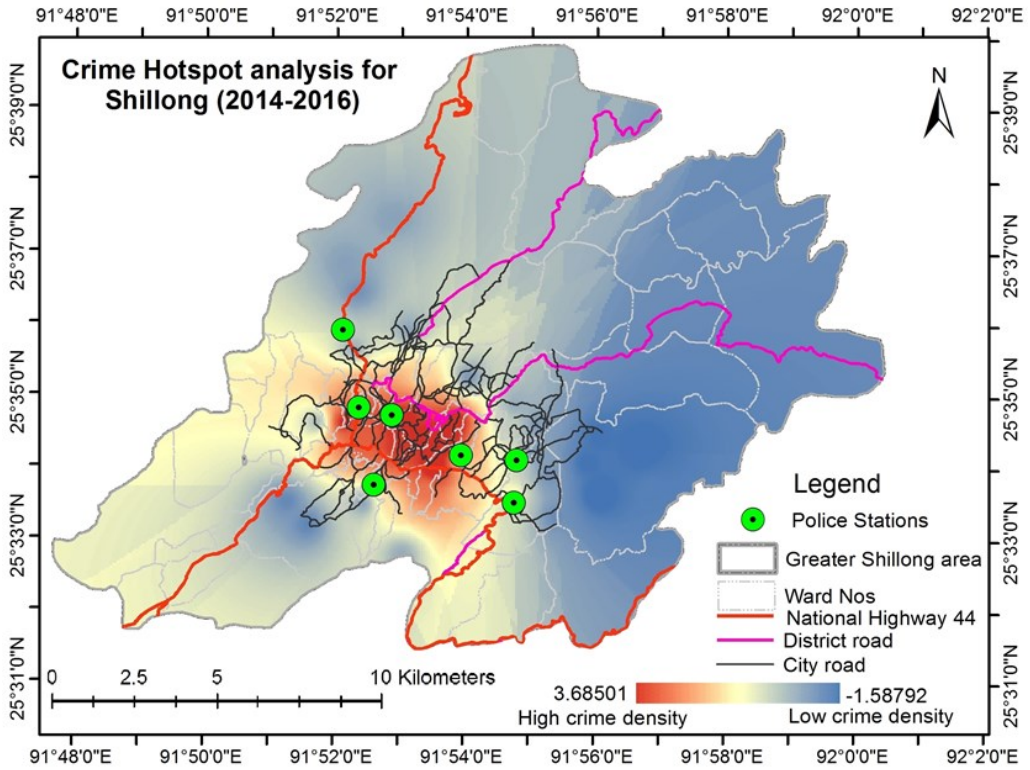

Figure 8: Hotspot in the form of crime density for 2014-2016 crime incident dataset of Shillong city

4.2 Patterns of crime incidents with time

The type of highest number of crime incidents registered during 2014-2016 was theft-related charges (Figure 2). It was highest in 2015 followed by 2016 and 2014, interestingly the highest number of theft-related cases occurred after 20:00 hrs and it reaches to its peak during 22:59-24:00 hrs. The number of crime incidents against each of the crime types registered in a different time periods is graphically presented in figure 9. The cases related to crime against women were occurring in higher rate during evening time (18:00 hrs.-20:00 hrs.). Other crime cases like cheating, trespassing, and murder related charges are not following any pattern with respect to time of occurrence. The human ecological character can often describe the relationship between time of occurrences or temporal behavior of such crime and the offender. As here crime mapping has been done focusing on the spatial character of the incidents happening, temporal analysis of crime incidents is beyond the scope of this paper.

4.3 Crime hotspots over population density

The spatial distribution of crime hotspot is associated with different types of socio-economic factors. In a world scenario, most of the crimes have occurred in highly populated areas. A population density map based on census 2011 data has been prepared. Crime hotspots (2014-2016) of the Shillong area overlaid on population density and existing police stations are given in figure 10. The crime density in each ward with their population density is given in table 2. It was observed that most of the crime hotspots appeared in those wards where population density is 10,000-20,000 per square kilometer. Interestingly crime hotspots were not observed in highly populated areas like Mawkhar and Jaiaw. Some of the hotspots (average) were found unevenly distributed over space irrespective of the size of the population density. For example, some of the areas with very less population density (500-2000) like Madanryting, Laitkor, and Pynthorumkhra are also found as crime hotspots (table 2).

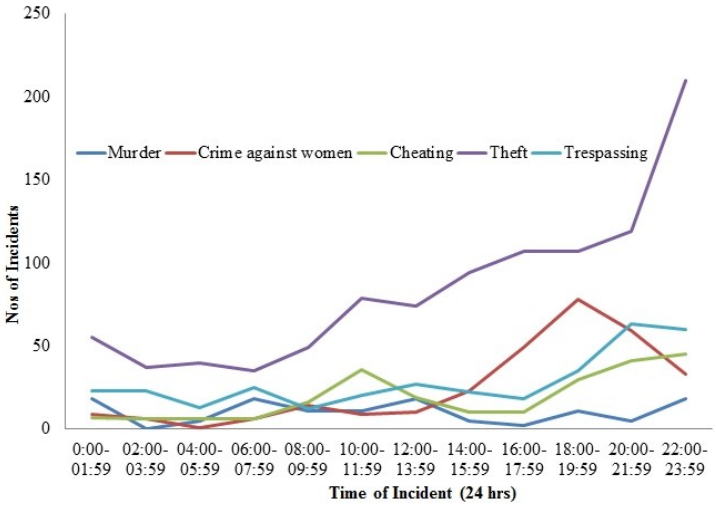

Figure 9: Number of crime cases registered in different time interval of the day

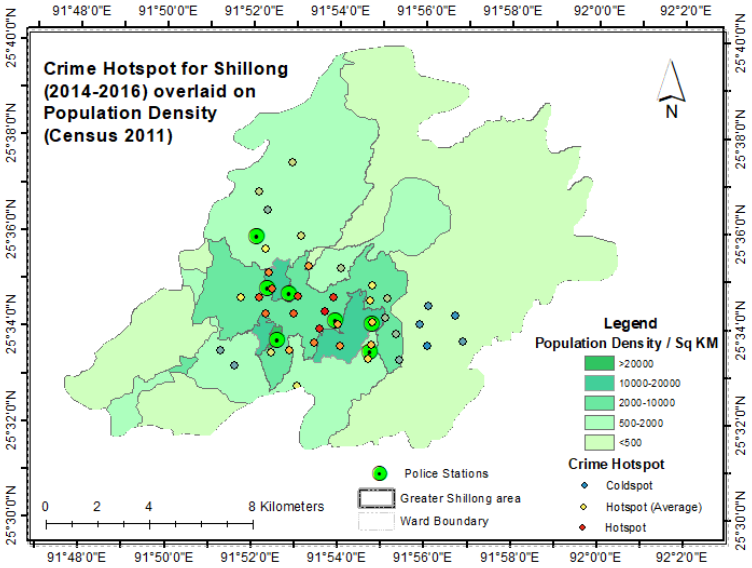

Figure 10: Crime hotspots of Shillong (2014-2016) over Population density

Table 2: Ward-wise Population density versus crime density

Ward name	Population Density/Sq km	Crime density
Mawkhar, Jaiaw, Jail Road, Laban, Malki	>20000	Average
Kench's Trace, Nongthymmai, Police Bazar	10000-20000	High
European Ward, European Ward, Jail Road, Laitumkhrah, Lumparing, Mawprem, Shillong Cantonment, 3rd Mile 5th Mile Laitumkhrah, Mawprem, Nongkseh, Rynjah, LapalangUmlyngka, Umpling	2000-10000	High
6th Mile, Kriet , Laitkor, Mawpat, Nongpiur, 4th Mile, Lawsohtun, Madanryting, Mawlai, Pynthorumkhrah	500-2000	High
Mawdiangdiang, Mawinaglah, Mawklot, MawlongMawpynthih, Mawtawar, Nongrah, Nongsawing, NongumlongSyllaiulur,Umsawli,Umshing Village	<500	Low

5. Conclusion

Spatio-statistical technique for analysis of crime hotspots in Shillong city, Meghalaya, India has been found to be extremely useful in understanding, mapping and predicting crime hotspots. The entire approach is based on a statistical method using Moran's index (m) and Getis-Ord G_i*. It involves deriving spatial distribution of patterns of crime with a higher confidence level based on optimal ranges of values of *z*-score and *p*-value with an appropriate threshold distance. It has been demonstrated that deriving threshold distance using incremental spatio autocorrelation can enhance the predictability of the crime hotspots.

The study identified the crime hotspots in the city with the occurrences of various types of crime occurred in different time periods of the day. It was observed that the hotspots were primarily confined to the central part of the city and some of the hotspots (average) were unevenly distributed over space irrespective of the size of the population density. The crime against women were reported mostly during the evening and the highest theft were reported after 2200 hrs during night. Other crime cases were not observed with any specific pattern concerning the time of occurrences.

It is difficult to achieve optimal values of crime statistics simultaneously for deriving the spatial distribution of crimes based on actual incidents. However, machine learning techniques could be explored for better analysis of hotspots as well as prediction for the coming year based on more time-series data.

Acknowledgements

The authors would like to thank the Office of the Superintendent, Shillong, Meghalaya for sharing of crime data of the period 2014-2016 for analysis in the reported work.

References

Achu, A.L. and R.S. Suja Rose (2016). GIS analysis of crime incidence and spatial variation in Thiruvananthapuram City, International Journal of Remote Sensing Applications (IJRSA), 6, 1, 10.14355/ijrsa.2016.06.001.

Ahmad, F., Md. M Uddin and G. Laxmi (2017). Role of geospatial technology in crime mapping: A perspective view of India, World Scientific News, WSN, 88(2), 211-226.

Ahmad, F., Md. M. Uddin and G. Laxmi (2018). Role of geospatial technology in crime mapping: A case study of Jharkhand state of India, American Journal of Geographical Research and Reviews, 1:5, DOI:10.28933/AJGRR-2018-01-1801.

Akpinar, E (2005). Using geographic information systems in analyzing the pattern of crime incidents and the relationship between land use and these incidents, Proceedings of the International Society for Photogrammetry and Remote Sensing, 2005.

Ansari, M.S. and K.V. Kale (2014). Mapping and analysis of crime in Aurangabad city using GIS, IOSR Journal of Computer Engineering,16(4), 67-76.

Balogun, T.F., H. Okeke, and C. Chukwukere (2014). Crime mapping in Nigeria using GIS, Journal of Geographic Information System, 6, 453-466.

Chen, D., J.R. Weeks, and J.V. Kaiser Jr (2015). Remote sensing and spatial statistics as tools in crime analysis. In F. Wang (Ed.), Geographic Information Systems and Crime Analysis Hershey, PA: IGI Global, 270-292. doi:10.4018/978-1-59140-453-8.ch016, 2015.

Danny, E (2015). Crime mapping using time series analysis in Asaba, Delta State, Nigeria: A remote sensing and GIS Approach, European Journal of Basic and Applied Sciences, 2(2).

Deshmukh, S., and B. Annappa (2018). Prediction of crime hotspots using spatiotemporal ordinary kriging, Integrated Intelligent Computing, Communication and Security, 683-691, doi: 10.1007/978-981-10-8797-4_70.

ESRI Tool reference. https://pro.arcgis.com/en/pro-app/tool-reference/data-management/integrate.htm.

Gamze, B., B. Sevket, H. EbruColak, and Y. Tahsin (2018). A crime prevention system in spatiotemporal

principles with repeat, near-repeat analysis and crime density mapping: Case study Turkey, Trabzon, Crime & Delinquency, 64(14), 1820-1835.

Getis, A., and J.K. Ord (1992). The analysis of spatial association by use of distance statistics, Geographical Analysis, 24: 189–206. doi:10.1111/j.1538-4632.1992.tb00261.x

Jaishankar, K., S. Shanmugapriya, and V. Balamurugan (2009). Crime mapping in India: A GIS implementation in Chennai city Policing, Geographic Information Sciences, 10:1, 20-34, DOI: 10.1080/10824000409480651.

Jorge, F., J. Paulo and J. Martins (2012). GIS for crime analysis: Geography for predictive models, Electronic Journal of Information Systems Evaluation, 15(1), 36-49.

Kounadi, Q., A. Ristea, L. Michael, and C. Langford (2018). Population at risk: using areal interpolation and twitter messages to create population models for burglaries and robberies, Cartography and Geographic Information Science, 45(3), 205-220, DOI: 10.1080/15230406.2017.1304243.

Kumar, J., S. Mishra, and N. Tiwari (2012). Identification of hotspots and safe zones of crime in Uttar Pradesh, India: Geospatial analysis approach, International Journal of Remote Sensing Applications, 2(1), 15-19.

Levine, N (2017). CrimeStat: A Spatial Statistical Program for the Analysis of Crime Incidents. In: Shekhar S., Xiong H., Zhou X. (eds) Encyclopedia of GIS. Springer, Cham.

Melo de, S. N., D. V. S. Pereira, M.A. Andresen, and L.F. Matias (2018). Spatial/temporal variations of crime: A routine activity theory perspective, International Journal of Offender Therapy and Comparative Criminology, 62(7), 1967–1991. https://doi.org/10.1177/0306624X17703654

Melo de, S. N., R. Frank, and P. Brantingham (2017). Voronoidiagrams and spatial analysis of crime, The Professional Geographer, 69(4).

Mohammed, A., and R. Salihu (2013). Spatiotemporal pattern of crime using Geographic Information System (GIS) approach in Dala L.G.A of Kano State, Nigeria, American Journal of Engineering Research, 51-58.

Moran, P (1950). Notes on continuous stochastic phenomena, Biometrika, 37(1/2), 17. doi: 10.2307/2332142

Nasridinov, A., and P. Young-Ho (2014). Crime hotspots analysis in South Korea: A user-oriented approach, Advanced Science and Technology Letters, 52, 81-85.

Snyders, E., K. Landman (2018). Perceptions of crime hot-spots and real locations of crime incidents in two South African neighbourhoods, Security Journal 31, 265–284, https://doi.org/10.1057/s41284-017-0099-9

Saravanakumar. S., and S.S. Revathy (2016). Crime mapping analysis: A GIS implementation in Madurai City, International Journal of Science and Research (IJSR), 5(3), 1894 – 1897.

Tahani, A., R. Mirza, and L. Elizabeth (2015). Crime prediction based on crime types and using spatial and temporal criminal hotspots, International Journal of Data Mining & Knowledge Management Process (IJDKP) 5(4).

Thangavelu, A, S.R. Sathyaraj, and S. Balasubramanian (2013). Assessment of spatial distribution of rural crime mapping in India: A GIS perspective, International Journal of Advanced Remote Sensing and GIS 20132(1), 70-85.

Wang, D., W. Ding and L. Henry (2013). Crime hotspot mapping using the crime related factors—a spatial data mining approach, Applied Intelligence, 39(4), 772–781.

Journal of Geomatics Vol. 14, No. 1, April 2020

Long-term determination of shoreline changes along the coast of Lagos

Peter C. Nwilo[1*], A. Chidi Ibe[2], Jimmy O. Adegoke[3], Jerry N. Obiefuna[4], Alfred S. Alademomi[1], Chukwuma J. Okolie[1], Olayemi O. Owoeye[1], Joel N. Nwokocha[1], Michael J. Orji[1], Abdulkareem A. Umar[1] and Olagoke E. Daramola[1]
[1]Department of Surveying & Geoinformatics, Faculty of Engineering, University of Lagos, Akoka, Lagos State, Nigeria
[2]Institute for Natural Resources, Environment and Sustainable Development, University of Port-Harcourt, Rivers State, Nigeria
[3]Department of Geoscience, Centre for Applied Environmental Research (CAER), University of Missouri, Kansas City, USA
[4]Department of Architecture, Enugu State University of Science & Technology, Enugu, Enugu State, Nigeria
*Email: [a]pcnwilo@unilag.edu.ng

(Received: Feb. 08, 2020; in final form: June 24, 2020)

Abstract: Analysis of shoreline changes is an important indicator in the study of coastal erosion and/or accretion. It aids in understanding the spatio-temporal trends in the changes triggered by natural processes and human impacts. The construction of two breakwaters (East and West moles) between 1908 and 1912 at the entrance to Lagos harbor inhibited the natural flow of the longshore drift, hence it accelerated erosion rate especially in the Victoria Island area while areas on the west of the breakwaters were accreting. This study relied on archival maps of 1900 – 1964 and satellite imageries of 2001–2016 to determine and visualize the magnitude of erosion and accretion along the coast of Lagos State. The shoreline positions at various epochs were extracted from the maps and satellite imagery by vectorization. The magnitude of change was determined by calculating the differences in the shoreline positions measured along vertical line segments spaced at 200-meter intervals. Then, the shoreline positions were plotted graphically. The analysis shows a trend of accretion on the western side of the shoreline up to the West mole and massive erosion eastwards of the East mole. However, the high magnitudes of erosion in the Victoria Island axis have been checkmated by the Eko Atlantic City project along with the construction of coastal defenses. Notwithstanding, evidence from recent satellite imagery and analysis of the shoreline changes shows that these anthropogenic interventions have only succeeded in transferring the erosive actions eastwards to areas downdrift of these coastal defenses.

Keywords: Erosion, accretion, coastal defenses, coastline, shoreline change

1. Introduction

The world's coastal areas are believed to house about two-thirds of the global population (Hanson and Lindh, 1993). It is therefore very important to understand the processes at work in coastal environments. The processes that determine the physical configuration of a coast are both natural and anthropogenic (Williams, 1960; Ibe, 1988; Nwilo, 1995). The natural processes include among others the waves, tides and surges, currents, the presence of canyons, earthquakes, the amount of rainfall, drainage characteristics, sea level trends and natural subsidence (Nwilo, 1995). Also, human activities such as the extraction of fluids, construction on and away from the coast, deforestation and canalization make a substantial contribution towards determining the physical configuration of the coastal environment (Nwilo, 1995). Coastal shorelines are defined as the interface between the land and sea (Bird, 1993; WIOMSA, 2010; Akinluyi et al., 2018), and the immediate position of the land–water line at an instant in time (Boak and Turner, 2005; Akinluyi et al., 2018). These shorelines are subject to changes in response to morphological, geological or climatic factors (Carter and Woodroffe, 1994; Pidwirny, 2006; Akinluyi et al., 2018). The analysis of shoreline changes is crucial to lot of studies being conducted by coastal scientists, engineers and geomorphologists.

Shoreline changes depict how the position of the shoreline moves with time; the shoreline can move landwards through the process of erosion or seawards by sediment accretion. This combined action of erosion and accretion changes the shape of the coast over time. Coastal erosion as a worrying phenomenon along the coast of Nigeria is influenced by tides, waves, longshore currents and ocean currents. This retreat of the Nigerian shoreline is a threat to coastal settlements, recreational grounds and oil export handling facilities which are located in coastal towns (Ibe and Antia, 1983). Waves constantly crash against the shore eroding the loose sandy beaches and moving the coastline farther inland. This is predominant along the coast of Lagos and was the reason for the loss of the Lagos Bar Beach in Victoria Island area of Eti-Osa Local Council. Annual rates of erosion between 20-30m/yr have been recorded in Lagos (Ibe, 1988; Orupabo, 1990; Nwilo and Onuoha, 1993). Ibe (1988) estimated that over 1.5km of the coastline had been lost in Victoria Island due to coastal erosion. Similarly, Obiefuna et al. (2013) have reported that the Lagos coastline along Eti-Osa and Ibeju/Lekki Councils was rapidly eroding and measured annual erosion rates in Eti-Osa Local Council as high as 8.75-10.11m between 2006 and 2009. More recently, Obiefuna et al. (2017) showed that the maximum rate of erosion on the eastern stretch of Lagos coastline between 2001 and 2013 occurred mainly in Eti-Osa Local Council at about 22.75m/yr around Kuramo Waters.

Coastal erosion is further exacerbated by accelerated sea-level rise being experienced globally. A coastal area with a low-lying topography like that of Nigeria will be adversely affected by a small rise in sea level (Nwilo, 1995). The impact of sea-level rise on coastal/shoreline erosion in low-lying coastal regions has received some attention by coastal scientists such as van Rijn (2011); Zhang et al. (2004) and Smith et al. (2010). Other coastal scientists have also inquired into the vulnerability of the coastal area to wind and storm surges. In that regard,

Harley et al. (2017) reported large-scale severe coastal erosion due to anomalous wave direction. Storms lead to coastal erosion and other changes in the shoreline due to high winds, an increase in the height of ocean water, and action of waves. IPCC (1992) has noted that the Nigerian coastal areas will be adversely affected by a small rise in sea level and from the accounts of Bruun (1962), a sea-level rise of 0.3m will cause a coastline recession of 30m on low-lying and flat coasts. Nwilo (1995) showed that the rate of sea-level rise along the Nigerian coast was 1mm/yr.

The Intergovernmental Panel on Climate Change (IPCC) in its Fourth Assessment Report (AR4) projected increased global sea-level rise rates between 1.5mm/yr and 9.7mm/yr in the 21st century (Meehl et al., 2007). The projections of sea-level rise in the more recent IPCC Fifth Assessment Report (AR5) are much higher than in AR4. According to the AR5 predictions summarised in Church et al. (2013), for the period 2081–2100, compared to 1986–2005, global mean sea level rise could be as high as 0.98m with a rate during 2081–2100 of 8-16 mm/yr. In furtherance to the observation of IPCC, the erosion issue in the Lagos coast is not influenced by sea-level rise alone. Other equally contributing factors are wave direction, storm surges, tides and lack of conservation of the coastal wetlands. In 2012, a storm surge coupled with erosion sheared off the entire Kuramo Beach and extended the Atlantic Ocean landward into Kuramo Waters, a hitherto partially landlocked waterbody. No significant study has been done on this storm impact since 2012. The recent Eko Atlantic City development that caused seaward sand filling of the ocean had mitigated erosion around the Bar Beach area. However, it is seemingly now causing severe erosion eastward of the beach.

Victoria Island in Eti-Osa Local Council has been the site of very active erosion following the completion in 1912 of the two stone breakwaters (stone moles) perpendicular to the shore purposely for protecting the entrance of dredged water into the Lagos harbor (Ibe et al., 1991). This inlet was known to be constantly silted thereby constituting navigational hazards to ships into Lagos harbor (Fowora-Ranardet Associates, 1981; Ibe, 1986, 1988; Nwilo, 1995). The construction of these stone moles impacted the normal flow of longshore sediment transport which was from west to east along the coastline. While the issue of siltation was remedied, it reduced the flow of sediments reaching the Victoria Island Beach on the east of the moles. As a result, while areas west of the West mole were experiencing accretion, there was acute erosion at Victoria Island east of the East mole. Figure 1 shows the positions of the East and West moles, and the direction of movement of the prevailing longshore current**.** This coastal erosion had destroyed the beach, constituted a threat to several high-brow developments on the frontage of Ahmadu Bello Way and infrastructures within the area. Kuramo Waters, a formerly enclosed water body in Victoria Island was breached by the Atlantic Ocean in 2012 (Obiefuna et al., 2017). Nwilo (2016) showed that its surface water area reduced by 0.24km^2 between May 2001 and December 2015; although the study did not consider the seasonal variations of water level in the rainy (wet) and dry seasons. Figure 2 shows observed changes in Kuramo Waters at five yearly periods – 2001, 2011, 2013, 2014 and 2015.

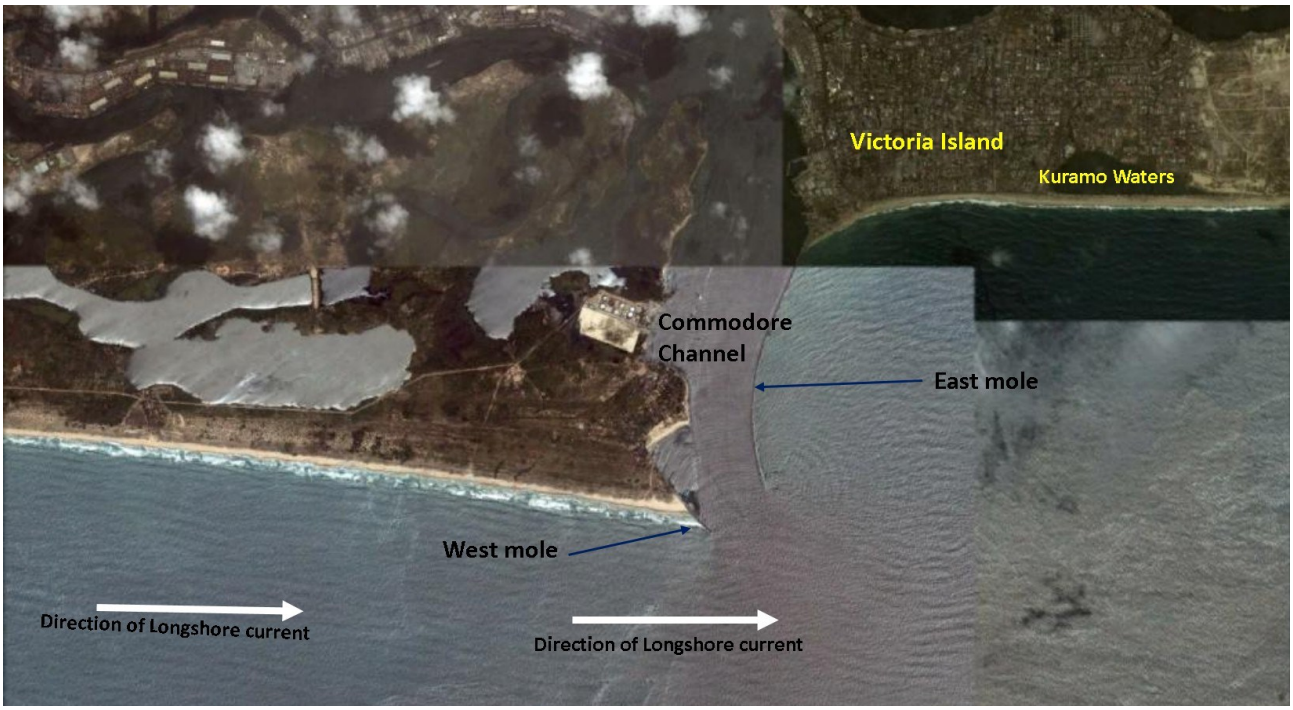

Figure 1: The positions of the East and West moles, and the direction of movement of the prevailing longshore current (Imagery source: Google Earth, October 2002)

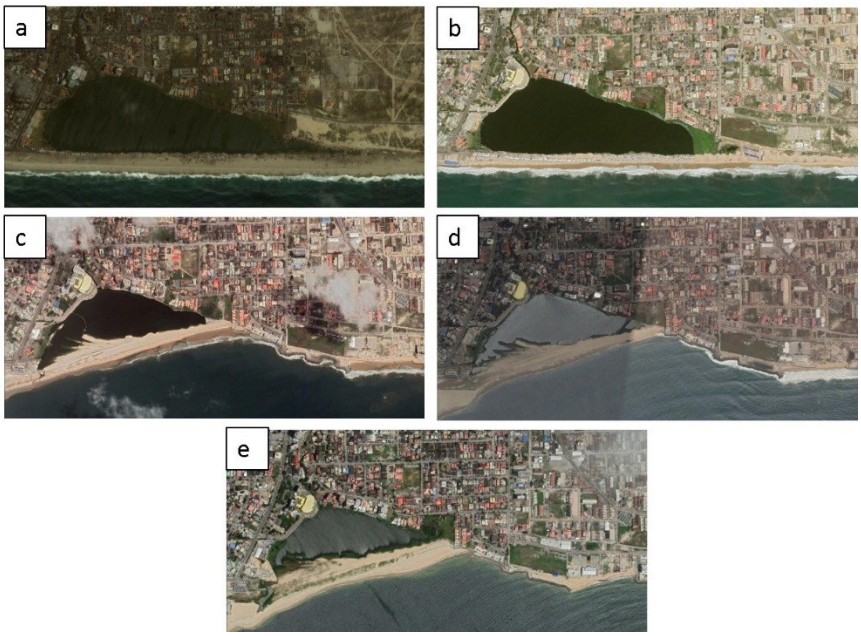

Figure 2: Observed changes in Kuramo waters at different periods – (a) May 5, 2001 (b) May 5, 2011 (c) October 20, 2013 (d) April 19, 2014 (e) October 12, 2015 (Imagery source: Google Earth).

Although several attempts including beach nourishment in the past (Ibe, 1988; Awosika, 1993) and in the subsequent years were made to rein in on the erosion menace on Victoria Island Beach, none was effective until the recent emplacement of coastal defenses and development of the Eko Atlantic City project. For effective coastal planning and management, it is desirable to continuously monitor both the developments on the Lagos coast along with the effects of emplaced coastal defense structures. Equally, it is worthwhile to undertake a historical evaluation of the impacts of these actions periodically to assess their effectiveness. This paper, therefore, addresses a long-term determination of shoreline changes in Lagos State. This is to understand the current situation of the shoreline since the construction of the moles as well as provide preliminary insights into the effectiveness of recent actions in taming the erosion menace on the affected parts of the Lagos coastal area.

1.1 Coastal morphology and wave regime

According to Obiefuna et al. (2017), the Lagos coastline is rimmed in its entirety by barrier islands. These barrier islands include the Badagry Island/Lighthouse Beach which is backed by Badagry Creek and Lighthouse Creek, the Victoria Island backed by Five Cowrie Creek, and Lekki Peninsula which is backed by the Five Cowrie Creek, and the Lagos and Lekki Lagoons. Geomorphologically, Ibe (1988) sees these barriers as part of the low-lying Barrier-Lagoon Complex which extends from the Nigeria/Benin border eastwards for about 200km. According to Ibe (1988), the morphology of this complex was determined by coastal dynamics, the drainage and a set of inter-related coastal processes. First, characterized by erosive beaches, there is the absence of 'exoreic' rivers which would have replenished from the hinterland sand lost from the longshore current action. This according to Ibe (1988), explains the absence of spits and barriers developing presently. Secondly, the longshore current is active in the area moving in a west-east direction.

Thirdly, there is a steep and narrow continental shelf (approximately 30km wide), that is indented by submarine canyons such as the Avon Canyon and Mahin Canyon, and gullies (Ibe, 1988; Obiefuna, 2015). This narrow continental shelf enables waves to reach the shore at higher heights and promotes the loss of nearshore sediments to the gullies and canyons. Lastly, there is intense wave action along the beaches, which is caused by the influence of the prevailing south-westerly winds. Also, Ibe (1988) notes that the barrier islands vary in width from ½ km to 21km and are generally aligned parallel to the Atlantic Coast. The barrier beaches form a narrow belt of largely sandy accumulations with width varying between 2-8km and average altitude of 0.75-5m above sea level (Abegunde, 1988). Features of the Lagos coastline which largely negate accretion and enhance beach erosion have been enumerated in Ibe (1988). These include high-intensity wave action, large swell waves with spilling breaker wave type as the most common, strong longshore currents, steep and narrow beach profile, erosive beaches, the steep and narrow continental shelf of 25km, presence of gullies and canyons and longshore transported sand of about 0.7 to 0.8million m^3/yr. Incessant high-energy swell waves, impacting the Lagos coast with a mean direction of 188°, induce a mean eastward longshore transport of sediments (van Bentum, 2012). According to Ibe and Antia (1983), "the angle at which the moles were constructed did nothing to mitigate the effect of waves on the coast. In fact, the eastern mole, by promoting eddying, accentuated the destructive impact of the waves which have continued to move sand eastwards from the Victoria Beach thereby precipitating the continuing erosion problem."

The waves have a south-westerly component driven by the south-westerly winds. Along the Lagos Bar Beach, waves are predominantly about 1 to 2 m high. However, during the rainy season, waves swell up about 3 to 4 m along most areas. The longshore currents are the predominant currents generated by the south-westerly breaking waves. Tides

occurring on the coast of Nigeria are semi-diurnal with two inequalities. The tides arrive in a south-westerly direction. Tidal range varies from 1m at Lagos and increases progressively eastwards to about 3m at Calabar (Awosika and Folorunsho, 2009). The action of the hydrodynamic forces makes the region vulnerable to storms in the rainy season (Busari and Osman, 2017).

1.2 Study area

The study area is the shoreline of Lagos state in Nigeria. Lagos is a low-lying coastal state and is Nigeria's center of commerce. It is located between Longitudes 2°41'15" - 4°22' 00" E and Latitudes 6°20' 10" - 6°43' 20" N. The study area falls within the Barrier-Lagoon Complex of the Nigerian geomorphological units. This coastal unit starts from the Nigeria-Benin Republic border and extends about 200km to the east. It is within the chain of barrier-lagoon complexes from Cote d'Ivoire through the mouth of the Volta River in Ghana, through Benin Republic and finally into Nigeria (Nwilo, 1995). As stated earlier, the Lagos coast consists of west-east trending barrier islands backed by the Badagry Creek, the Lagos and Lekki lagoons as shown in figure 3. The Lagos Lagoon has a direct link to the Atlantic Ocean through the Commodore Channel. Due to this link, the salinity of the Lagos Lagoon is higher than that of Lekki Lagoon (Ibe, 1988). Furthermore, along the Lagos coast, sediment transport by the longshore drift is controlled by the prevailing wind direction (Awosika and Folorunsho, 2009). Sediment transport by this drift is blocked by the breakwaters, the coastal defenses and groins of the Eko Atlantic City project. The erosion force is deflected inwards towards Victoria Island and areas on the downdrift side of the coast. Based on the old Local Government set-up, Lagos has 20 Local Government Areas (LGAs) or Councils. Over the years, accelerated migration from other parts of Nigeria and neighboring countries has resulted in a rapidly expanding and diverse population within Lagos State.

2. Materials and Methods

2.1 Data acquisition and analysis

The maps for the years 1900, 1946 and 1964 and a set of satellite imageries for the years 2001, 2012 and 2016 were compiled. The coverage of the 1900 and 1946 map does not extend beyond the Lagos harbor area. The imageries were downloaded from Google Earth using El-shayal software. Table 1 shows the characteristics of the datasets used in this study. In ArcGIS Software, the maps were georeferenced. The satellite imageries required no georeferencing since El-shayal maintains their rectification during download. All the datasets were re-projected from geographic coordinates to a Universal Transverse Mercator (UTM) projection referenced to the WGS84 datum. This transformation helped to overcome linear measurement difficulties, preserve geometric properties, and ensure harmony in the coordinate system and datum properties of the datasets. Following the approach of Zollini et al. (2019), the maps and imageries were manually vectorized to extract the shoreline positions within ArcGIS software. Two baselines were drawn along the east and west sides of the coast. Perpendicular line segments were projected from the baselines to intersect all the shorelines at intervals of 200m (183 segments on the eastern side of the coast and 191 segments on the western side). Figure 4 shows the baselines and extent of areas measured (A, B, C and D) drawn on the western and eastern sides of the coast. The categorization of the coastline into four areas, A, B, C and D aided the sub-division of the coastline into smaller portions with similar characteristics for more detailed analysis. The distances from the baseline to each shoreline along the segments, and the magnitudes of change between shorelines were then measured and compiled in a tabular form. The analysis was also supported by a field survey of the area to acquire photographs of some of the groins as well as to observe the effects of the erosional action.

Figure 3: Map showing the Lagos coastal area

Table 1: Characteristics of the datasets used

S/N	Data	Source/Publisher	Acquisition Date
1	Earth observation data	Google Earth	2001, 2012, 2016
2	Map of Lagos harbor area	National Institute for Oceanography and Marine Research (NIOMR)	1900
3	Nigeria City Plans, Edition 1-AMS (1:12,500)	US Army Corps of Engineers Army Map Service (USACE-AMS), Office of the Surveyor General of the Federation (OSGOF)	1946
4	Topographic maps (1:50,000)	Office of the Surveyor General of the Federation	1946, 1964

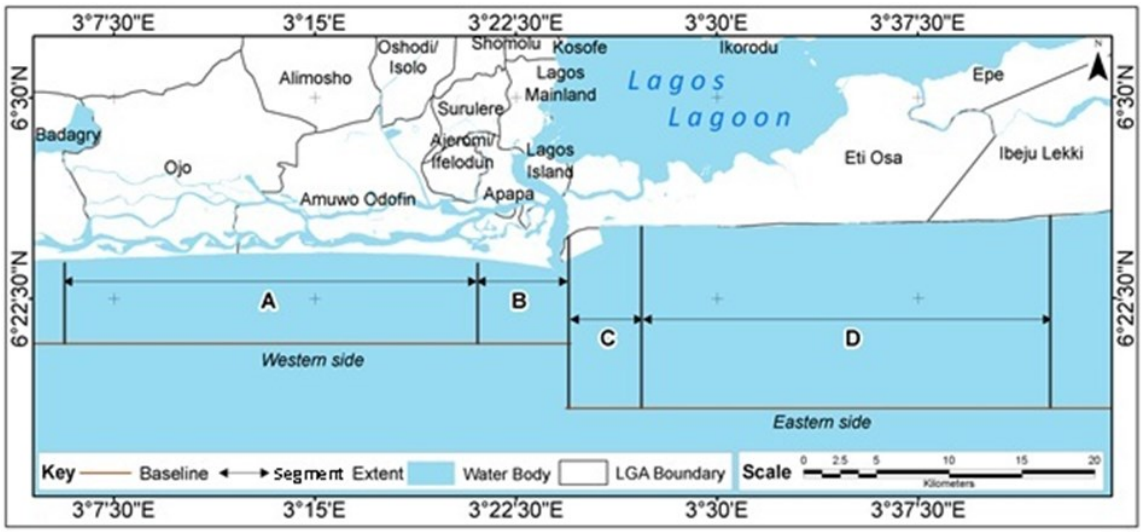

Figure 4: The two baselines and extents of measured areas (A, B, C and D) drawn on the western and eastern sides of the Lagos coast

3. Results and Analysis

The 191 line segments drawn on the western side of the coast (A and B) were spread over a total distance of 37.8km while the 183 transects drawn on the eastern side of the coast were spread over a total distance of 36.4km (C and D). For the western side of the coast, table 2 shows the vertical distance between shoreline positions on the western side of the Lagos coast (A) – an 8-kilometer section starting from Igbooja Beach at 510434mE and going eastwards. Table 3 shows the vertical distance between shoreline positions on the western side of the Lagos coast (B) - From Apapa at 538834mE to end-point at the West mole. For the eastern side of the coast, table 4 shows the vertical distance between shoreline positions on the eastern side of the Lagos coast (C) - a 5-kilometer stretch at Victoria Island from the East mole going eastwards. Table 5 shows the vertical distance between shoreline positions on the eastern side of the Lagos coast (D) – an 8-kilometer section starting from Victoria Island at 552097mE and going eastwards. Positive changes indicate erosion while negative changes indicate accretion. A few data gaps were observed in the tables at areas where there were gaps in imagery/map coverage.

There is evidence of erosion and accretion on the eastern and western sides of the coast respectively. However, the general trend on the eastern side shows erosion is more predominant while on the western side, accretion is predominant. Thus, the rate of accretion statistics measured on the western side was extracted and summarised in table 6 while the rate of erosion statistics was extracted and summarised in table 7. On the western side, the highest rate of accretion of 15.91m/yr occurred between 2012-2016 close to Siku village in Amuwo Odofin LGA while the lowest rate of accretion of 0.02m/yr was measured at two areas – at Igboeseyore in Amuwo Odofin LGA between 1964 and 2001; and at Olomometa in Ojo LGA between 2001 and 2012. On the eastern side, the highest rate of erosion of 26.5m/yr occurred at the area previously inhabited by Apese community in Eti-Osa LGA between 2001 and 2012. Apese community has since been submerged by water.

The positions of the shorelines as vectorized from the datasets are presented graphically in figures 5 to 8. In the 37.8km western section, figure 5 shows shoreline changes from Igbooja Beach, Ojo LGA to Apapa while figure 6 shows shoreline changes from Apapa to end-point at the West mole. On the 36.4km eastern section, figure 7 shows shoreline changes at Victoria Island from the East mole going eastwards while figure 8 shows shoreline changes from Victoria Island to Orimedu, Ibeju Lekki LGA. In figure 8, two downward spikes are observed close to the 2200m mark. These spikes take the shape of groins constructed on the coast.

Table 2: Vertical distance between shoreline positions on the western side of the Lagos coast (A) – an 8-kilometer section starting from Igbooja Beach (510434mE) going eastwards

Line Seg. ID	Line Segment Easting (mE)	Distance (m)		
		1964-2001	2001-2012	2012-2016
1	510434.62	-153.36	12.23	18.37
2	510634.62	-119.98	6.54	19.93
3	510834.62	-147.45	22.04	21.64
4	511034.62	-118.11	24.47	19.18
5	511234.62	-114.90	14.90	19.04
6	511434.62	-112.95	10.96	20.02
7	511634.62	-117.58	11.80	27.46
8	511834.62	-131.27	23.60	19.11
9	512034.62	-131.85	30.57	2.21
10	512234.62	-135.15	32.85	0.91
11	512434.62	-78.27	14.36	3.87
12	512634.62	-62.44	18.12	2.25
13	512834.62	-111.26	13.19	17.93
14	513034.62	-113.53	6.99	21.04
15	513234.62	-140.25	15.05	16.54
16	513434.62	-118.39	6.11	16.20
17	513634.62	-81.63	17.53	11.60
18	513834.62	-122.86	4.91	10.65
19	514034.62	-34.83	-0.22	8.31
20	514234.62	-99.41	0.21	15.05
21	514434.62	-82.00	-16.27	13.47
22	514634.62	-81.46	-15.44	13.12
23	514834.62	-84.79	-23.45	10.20
24	515034.62	-96.75	-29.07	17.20
25	515234.62	-52.00	-73.75	23.27
26	515434.62	-197.49	35.74	27.24
27	515634.62	-203.90	53.75	29.93
28	515834.62	-202.42	47.13	21.74
29	516034.62	-216.13	46.66	28.39
30	516234.62	-233.00	35.77	21.09
31	516434.62	-202.47	34.12	21.75
32	516634.62	-196.15	29.46	19.31
33	516834.62	-146.27	13.49	20.02
34	517034.62	-187.86	9.92	20.16
35	517234.62	-179.02	0.86	15.83
36	517434.62	-177.29	-0.90	10.52
37	517634.62	-159.62	4.89	7.14
38	517834.62	-158.57	-12.24	12.33
39	518034.62	-171.53	-16.61	15.58
40	518234.62	-176.14	-19.31	20.59
41	518434.62	-183.41	-12.55	25.31

On the western side, the predominance of accretion is very evident thereby causing sediment accumulation at the West mole, while on the eastern side, the predominance of erosion is evident. On the eastern side, high erosion is observed at an area previously inhabited by Apese community in Eti-Osa LGA between 2001 and 2012. Apese community has since been submerged by water. The wave pattern along the coast contributes to the accretion and erosion variation. Observations have shown that waves at the Victoria Island Beach are mainly swells caused by the prevailing westerly winds, with a long ocean fetch, having a wave period between 8 – 13secs while the longshore currents move eastwards (Afiesimama, 2003; Egberongbe et al., 2006). Between 2001 and 2012, there was an area with no observable change with no erosion and accretion (stable) at Orimedu in Ibeju Lekki LGA. There were also several areas without any observable change along the Eko Atlantic City wall where the position of the wall has remained stable within that same period. The unusually high magnitudes of erosion observed here between 2012 and 2016 seem to be occurring after the construction of the Eko Atlantic City especially as Ibe (1988) noted some accretion and minimal erosion previously in this area.

Figure 9 shows some of the newly constructed groins along the coast. These groins were constructed perpendicular to the coast to interrupt the water flow and limit the movement of eroded sediment being transported away

from the Victoria Island area. This led to accretion/deposition on the upper end and erosion on the lower end. The areas between the groins are observed to be u-shaped or crenulated. This shape is a result of despoliation by erosive forces acting within the groin fields (Figure 10).

Table 3: Vertical distance between shoreline positions on the western side of the Lagos coast (B) - From Apapa (538834mE) to end-point at the West mole

Line Seg. ID	Line Segment Easting (mE)	Distance (m)			
		1900-1964	1964-2001	2001-2012	2012-2016
1	538834.62	376.92	37.87	40.77	28.34
2	539034.62	380.38	41.77	37.57	43.04
3	539234.62	350.02	38.72	43.79	45.41
4	539434.62	341.77	54.64	33.64	63.64
5	539634.62	366.79	75.37	17.51	61.57
6	543434.62	345.44	25.23	52.66	47.35
7	541834.62	323.53	36.20	31.49	42.92
8	542034.62	344.49	41.80	26.70	47.94
9	542234.62	338.17	45.82	45.00	32.48
10	542434.62	495.56	22.82	49.12	38.86
11	539834.62	515.98	45.58	27.02	15.00
12	540034.62	540.19	26.19	37.76	37.70
13	540234.62	537.97	40.55	26.98	46.68
14	540434.62	562.33	34.97	34.06	62.26
15	540634.62	596.19	16.09	34.65	33.85
16	540834.62	617.45	8.02	37.47	57.04
17	541034.62	634.31	14.92	29.11	43.34
18	541234.62	654.46	38.55	28.32	46.69
19	541434.62	647.90	75.91	25.85	51.12
20	541634.62	547.75	40.12	40.32	42.41
21	542634.62	618.43	26.96	14.03	51.21
22	542834.62	650.37	57.07	9.64	49.49
23	543034.62	734.86	96.96	15.52	49.87

Table 4: Vertical distance between shoreline positions on the eastern side of the Lagos coast (C) - a 5-kilometer stretch at Victoria Island from the East mole going eastwards

Line Segment ID	Line Segment Easting (*mE*)	Distance (m)				
		1900-1946	1946-1964	1964-2001	2001-2012	2012-2016
1	545097.38	-1009.92	223.06	-475.62	2044.28	0.19
2	545297.38	-928.20	-26.96	-274.03	2051.38	-0.02
3	545497.38	-837.80	-63.75	-251.64	2025.35	0.00
4	545697.38	-737.77	-79.11	-	-	0.00
5	545897.38	-675.57	-65.55	-	-	0.00
6	546097.38	-556.87	-69.26	-302.71	1917.55	0.00
7	546297.38	-481.80	-84.62	-289.56	1852.66	0.00
8	546497.38	-415.57	-98.61	-264.46	1777.11	0.47
9	546697.38	-412.29	-60.99	-258.09	1708.48	0.00
10	546897.38	-369.44	-37.95	-237.12	1622.82	0.00
11	547097.38	-351.19	-15.14	-220.71	1538.16	0.00
12	547297.38	-349.24	18.61	-212.87	-74.93	1535.58
13	547497.38	-327.03	29.19	-216.45	-110.48	1511.65
14	547697.38	-311.11	25.27	-204.03	-167.02	1501.79
15	547897.38	-299.72	26.72	-203.18	-211.86	1514.67
16	548097.38	-299.88	24.75	-184.63	-282.69	1551.73
17	548297.38	-284.18	-1.92	-160.39	-291.48	1525.70
18	548497.38	-274.93	-3.22	-155.22	-255.86	1458.36
19	548697.38	-261.18	-3.19	-143.58	-200.97	1360.63
20	548897.38	-263.79	-11.18	-150.90	-112.71	1279.08
21	549097.38	-266.70	-12.60	-	-	1197.14
22	549297.38	-247.87	-11.56	-	-	1194.36
23	549497.38	-223.51	-22.64	-	-	1162.42
24	549697.38	-201.57	-7.92	-146.88	-65.31	1130.13
25	549897.38	-209.75	-1.28			-34.00

Table 5: Vertical distance between shoreline positions on the eastern side of the Lagos coast (D) – an 8-kilometer section starting from Victoria Island (552097mE) and going eastwards

Line Segment ID	Line Segment Easting (*mE*)	Distance (m)		
		1964-2001	2001-2002	2012-2016
11	552097.38	-213.01	12.78	159.09
12	552297.38	-209.89	-68.91	-6.87
13	552497.38	-218.47	-35.61	154.94
14	552697.38	-240.82	-46.84	-34.48
15	552897.38	-233.80	-37.67	-22.19
16	553097.38	-252.55	-36.03	-46.12
17	553297.38	-242.32	-24.03	-14.31
18	553497.38	-228.25	-35.16	-41.66
19	553697.38	-265.75	-5.66	-4.70
20	553897.38	-241.90	-15.74	-25.99
21	554097.38	-232.79	-3.41	2.36
22	554297.38	-237.15	-3.32	-11.60
23	554497.38	-195.79	-13.10	6.88
24	554697.38	-211.45	-12.40	-58.10
25	554897.38	-192.70	-13.33	-39.54
26	555097.38	-148.79	-31.23	-72.52
27	555297.38	-117.17	-21.76	-39.89
28	555497.38	-100.44	-16.17	-63.34
29	555697.38	-133.30	-17.43	-42.85
30	555897.38	-123.10	-22.44	-73.29
31	556097.38	-115.19	-26.58	-51.73
32	556297.38	-105.50	-24.56	-96.14
33	556497.38	-98.84	-45.35	-73.23
34	556697.38	-122.35	-38.02	-61.00
35	556897.38	-115.16	-48.56	-38.80
36	557097.38	-125.83	-45.52	-55.87
37	557297.38	-140.94	-31.21	-51.76
38	557497.38	-127.14	-38.53	-62.75
39	557697.38	-153.16	-37.70	-57.26
40	557897.38	-	-	-61.61
41	558097.38	-	-	-66.22
42	558297.38	-173.80	-11.46	-48.14
43	558497.38	-165.81	-21.99	-48.51
44	558697.38	-163.50	-28.75	-38.45
45	558897.38	-169.95	-32.95	-34.92
46	559097.38	-181.77	-24.41	-34.55
47	559297.38	-171.23	-19.04	-20.16
48	559497.38	-169.15	-13.92	-15.66
49	559697.38	-137.76	-23.30	-8.94
50	559897.38	-143.48	-12.62	4.03
51	560097.38	-143.88	-13.86	6.85

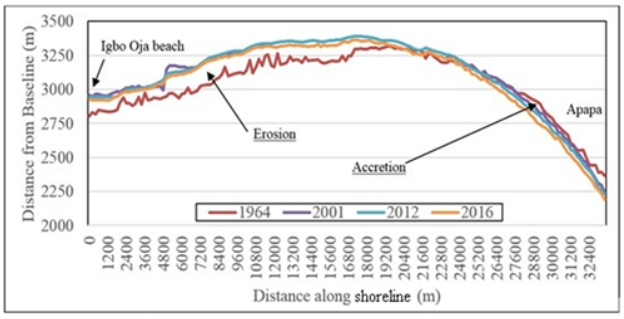

Figure 5: Shoreline changes from Igbooja Beach, Ojo LGA to Apapa (A)

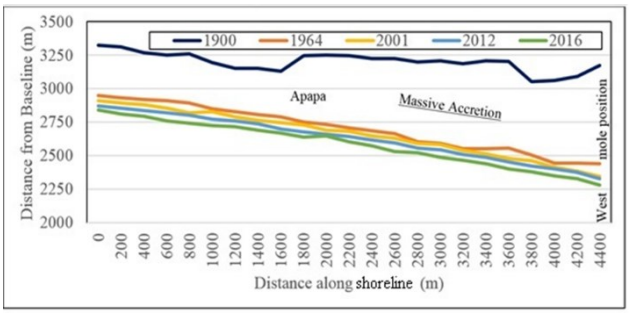

Figure 6: Shoreline changes from Apapa to end-point at the West mole (B)

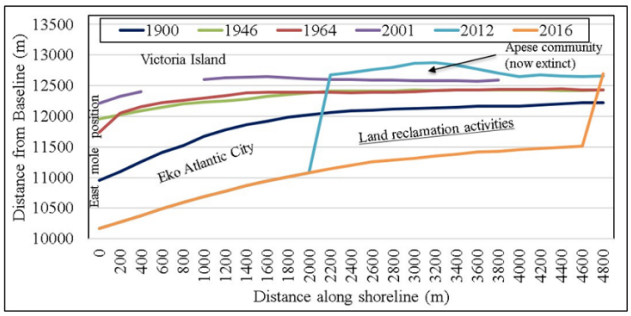

Figure 7: Shoreline changes at Victoria Island from the East mole going eastwards (C)

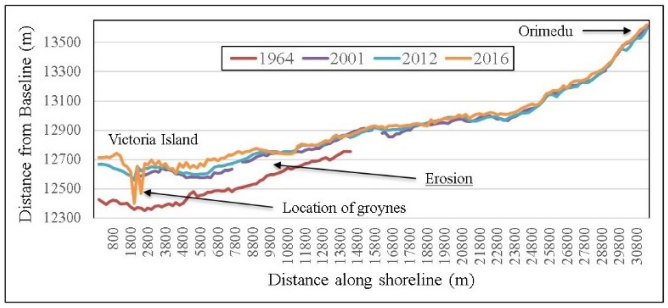

Figure 8: Shoreline changes from Victoria Island to Orimedu, Ibeju Lekki LGA (D)

Table 6: Rate of accretion (m/yr) on the western side of the Lagos coast

	From Apapa (538834*mE*) to end-point at the West mole				From Igbooja Beach (510434*mE*) to Apapa		
	1900 - 1964	**1964 - 2001**	**2001 - 2012**	**2012 - 2016**	**1964 - 2001**	**2001 -2012**	**2012 -2016**
Min	5.06	0.22	0.88	3.75	0.02	0.02	0.23
Max	11.48	2.62	4.79	15.91	3.27	4.89	15.91

Table 7: Rate of erosion (m/yr) on the eastern side of the Lagos coast

	From the East mole (545097*mE*) going eastwards					From Victoria Island (550097*mE*) to Orimedu, Ibeju-Lekki LGA		
	1900 - 1946	**1946 - 1964**	**1964 - 2001**	**2001 - 2012**	**2012 - 2016**	**1964 -2001**	**2001 - 2012**	**2012 -2016**
Min	4.38	0.07	1.97	5.94	0.00	1.24	0.00	0.08
Max	21.95	5.48	12.85	26.50	8.50	7.18	9.24	26.17

Figure 9: Newly constructed groins off the Lagos coast (Imagery source: Google Earth, December 2015)

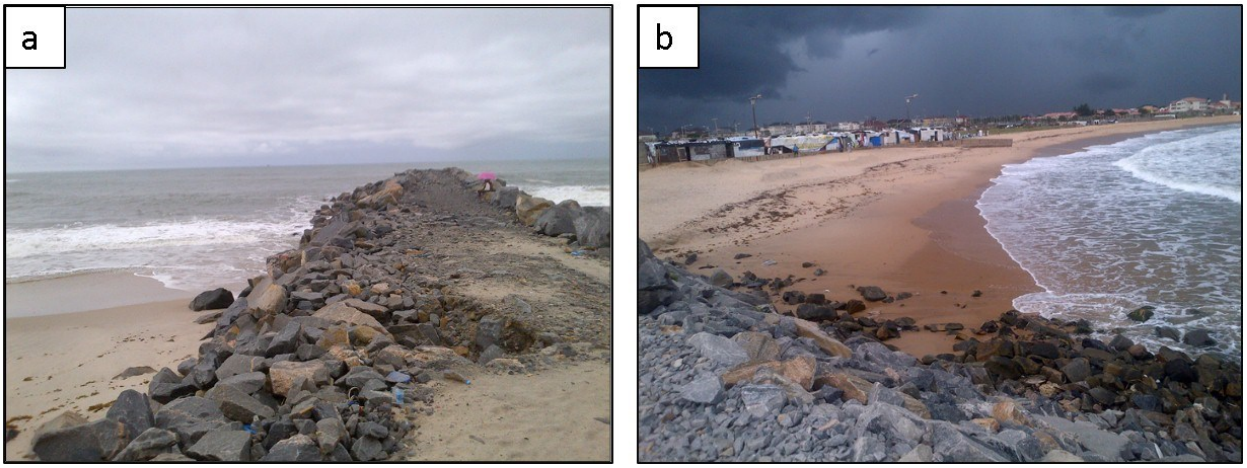

Figure 10: (a) A view down the length of one of the groins (b) Ongoing erosion alongside one of the groins constructed on the Lagos coast (Field survey, October 4, 2017)

4. Discussion

The findings confirm accretion on the western side of the coast. For example, in the measurement from Apapa to the end-point at the West mole, the maximum rates of accretion of 11.48m/yr and 15.91m/yr were obtained during the 1900-1964 and 2012-2016 periods respectively. The accretion is caused by the withdrawal of sediments from the longshore drift and subsequent accumulation which is very pronounced at the West mole area. The findings also confirm a general increase in the trend of landward erosion on the eastern side of the Lagos coast. From the East mole going eastwards, maximum rates of erosion of 21.95m/yr and 26.50m/yr were measured during the 1900-1946 and 2001-2012 periods respectively. The natural factors propelling this rapid erosion include the low coastal plain topography, intensive or high wave energy which generates destructive littoral currents; the 'microtidal' and 'mesotidal' nature of the coastline, vulnerable soil conditions; the semi-diurnal tides that set up near-permanent reversible currents which transport sediments away from the coastline at steep angles. Ibe (1988) also identified that anthropogenic activities ranging from harbor protection structures with jetties, beach sand mining and deforestation, all aid coastal erosion. He further stressed that the construction of dams on some rivers prevents the normal delivery of sediment thereby starving the coastal zone of sediment nourishment.

The recent and on-going development of the Eko Atlantic City project on the eastern side aimed at checkmating the erosion problem in Victoria Island appears to have reduced the acute erosion here. The possible factors that may be responsible for this could be the change of wave direction, longshore current, inappropriate coastal defense measures, the impact of large-scale land reclamation on the Atlantic Ocean at the west, and weak environmental safeguards. However, as evident from literature (Watson and Adams, 2011; Obiefuna et al., 2017), hard engineering coastal defense structures tend to deflect erosive action to unprotected areas downdrift of their location. Consequently, increased erosive action has been witnessed in recent years eastwards in the Lekki Peninsula, areas previously known to be either accreting or experiencing minimal erosion (Ibe, 1988). For example, on the eastern side of the coast from Victoria Island going towards Orimedu, erosion rates as high as 26.17m/yr were measured during the 2012-2016 period. This has been somewhat confirmed by the construction of several perpendicular groins downdrift on the Lekki Peninsula since 2013. According to Obiefuna et al. (2017), these newly constructed groins are apparent confirmation of existing serious erosion.

It is important that the nature of the coastal defense measures to be applied should depend very much on the nature of the coast, the processes that determine the nature of that coast and the level of development on it. The tendency is for a nation or state to protect areas with very high economic values as against areas that are sparsely developed. This is what is playing out in Lagos State. It is evident that the intervention measures introduced in Victoria Island were able to slow down erosion in the vicinity. However, on the coast towards Ibeju Lekki LGA, erosional action is still active and unabated. For instance, it was observed that Apese community located close to Victoria Island was submerged by water. The coastal defense measures put in place on the eastern side of the coast along the Eko Atlantic City and the groins constructed off the Lekki Peninsula appear to have wrought some adverse effects downdrift and even within the groins stemming from the coupled destruction of the aesthetic quality of the beaches in this corridor. The steady erosion of the Lagos shoreline portends long-term danger to the teeming inhabitants of this area. The shorelines of Ibeju/Lekki and Eti-Osa Local Councils are fast eroding. Despite this, these councils are parts of the barrier island of Lekki Peninsula that are experiencing rapid development. Within the area are many luxury housing estates, recreational centers and beaches, a proposed seaport and a Free Trade Zone that are all serviced by one single access, the Lekki/Epe Expressway.

5. Conclusion

In furtherance of the understanding of the coastal dynamics along the Lagos coast, this study integrated high-resolution satellite imagery and historical maps to determine the magnitudes of coastal erosion and accretion along the shoreline. The study has demonstrated a simple, stepwise

and repeatable approach for monitoring these changes over extensive periods. The results provide a vast knowledge base and spatial information to inform the relevant stakeholders charged with the oversight and management of the coastal resources and infrastructure in Lagos State and Nigeria.

6. Recommendations

The shoreline is a sensitive zone that requires careful and sensitive management. The need to understand the coastal processes at work on the Lagos coast cannot be overemphasized. With the recent developments along the coast, there is the need for intensive and robust investigation of their impacts on the coastal dynamics of the Lagos shoreline. The findings draw attention to the loss of socio-economic livelihoods of the dwellers along this coastal corridor. An example is the Apese community which has been completely uprooted and submerged by water. The government should take urgent steps to protect the coastal communities from annihilation by coastal erosion. Also, since coastal erosion is part of the physical processes inevitable in the barrier-lagoon complex of Lagos regardless of the coastal defenses being put in place, a more holistic plan of action should be taken by the Government in addressing the issue. Understanding the processes will be of immense benefit in the management and development of its coastal environment. Continuous monitoring of the Lagos coast is vital in addressing the issue of coastal erosion and accretion. In the planning of future coastal defense measures by the Government, it is advised that the geomorphology and sediment characteristics of the coast should be considered in determining the nature of the defenses to be emplaced. This will promote an integrated coastal management strategy and not just one influenced by economic benefits.

Continuous monitoring of the Lagos coast is vital in addressing the issue of coastal erosion. The Government should produce a deliberate institutional and funding policy for monitoring of the state's shoreline. The Federal Government should set up a Coastal Management Commission under the Ministry of Environment. This Commission should have the power to implement an integrated coastal management plan for the entire country without delay. The coastal management program should include the following steps: identification of the problems to be addressed; identification of the priorities among these problems; an analysis of specific processes that cause these problems; identification of specific management techniques designed to mitigate these problems; and a set of organizational arrangements and administrative processes for implementing a management program. Also, a vulnerability assessment of some major towns, installations and infrastructure in the country to coastal erosion should be undertaken. Lastly, national cooperation on the issue of coastal erosion should be established. The problems of coastal erosion have no state boundaries. Some response actions applied in one state can trigger off problems in a neighboring state. Cooperation and coordination are vital.

References

Abegunde, M.A.A. (1988). Shoreline Erosion and Land Use Management on the Active Sand Barrier Beaches around Lagos: A New Focus in Environmental Management in Sada, P.O. & F.O. Odemerho. (eds). Environmental Issues and Management in Nigerian Development, Evans Brothers, Ibadan, 231-238.

Afiesimama, E.A. (2003). Understanding ocean surges and possible signals over the Nigerian coast: a case study of the Victoria Island Bar–Beach Lagos. Retrieved from https://www.oceandocs.org/bitstream/handle/1834/420/Aniola_Nigeria.pdf?sequence=1

Akinluyi, F.O., A.O. Adebola and A.A. Adeseko (2018). Assessment of shoreline and associated landuse/land cover changes along Part of Lagos Coastline, Nigeria, Contemp. Trends. Geosci., 7(1), 59-71. DOI: 10.2478/ctg-2018-0004.

Awosika, L.F. (1993). Coastline erosion in Nigeria and some other West African coastal states: regional approach to response measures, 3rd Meeting of the Inter-Africa Committee on Oceanography, Sea and Inland Fisheries, Cairo, Egypt, April, 12-17, 1993.

Awosika, L. and R. Folorunsho (2009). The Ocean Data and Information Network of Africa. In M. Odido, & S. Mazzilli, African Oceans and Coasts (pp. 127-132). Kenya: United Nations Educational, Scientific and Cultural Organization.

Bird, E.C. (1993). Submerging Coasts: The Effects of a Rising Sea Level on Coastal Environments, Wiley, New York.

Boak, E.H. and I.L. Turner, (2005). Shoreline definition and detection: A Review, Journal of Coastal Research. West Palm Beach, Florida, 688-703.

Bruun, P. (1962). Sea-level rise as a cause of shoreline erosion, Proceedings of the American Society of Civil Engineers, Waterways and Harbours Division, 88, 153-232.

Busari, S. and O.M. Osman, (2017, July 10). Lagos floods: Heavy rain, storms cause chaos. Retrieved from CNN: https://edition.cnn.com/2017/07/09/africa/lagos-flood-storms/index.html

Carter, R.W.G. and C.D. Woodroffe (1994). Eds: Coastal Evolution: Late Quarter Shoreline Morphodynamics, Cambridge University Press, Cambridge, UK.

Church, J.A., P.U. Clark, A. Cazenave, J.M. Gregory, S. Jevrejeva, A. Levermann, M. A.Merrifield, G.A. Milne, R.S. Nerem, P.D. Nunn, A.J. Payne, W.T. Pfeffer, D. Stammer and A.S. Unnikrishnan (2013). Sea Level Change. In: Climate Change 2013: The Physical Science Basis. Contribution of Working Group I to the Fifth Assessment Report of the Intergovernmental Panel on Climate Change [Stocker, T.F., D. Qin, G.-K. Plattner, M. Tignor, S.K. Allen, J. Boschung, A. Nauels, Y. Xia, V. Bex and P.M. Midgley (eds.)]. Cambridge University Press, Cambridge, United Kingdom and New York, NY, USA

Egberongbe, F.O., P.C. Nwilo and O.T. Badejo (2006). Oil Spill Disaster Monitoring along Nigerian Coastline. 5th FIG Regional Conference: Promoting Land Administration and Good Governance.

Fowora-Ranardet Associates (1981). Stabilisation and Preliminary Engineering designs of Victoria Beach, Lagos. Submitted to the Federal Ministry of Works, 3 vols.

Hanson, H., and G. Lindh (1993). Coastal Erosion – An Escalating Environmental Threat, Ambio, 22(1), 189-195.

Harley, M.D., I.L. Turner, M.A. Kinsela, J.H. Middleton, P.J. Mumford, K.D. Splinter, M.S. Phillips, J.A. Simmons, D.J. Hanslow and A.D. Short (2017). Extreme coastal erosion enhanced by anomalous extratropical storm wave direction. Scientific Reports, 7: 6033. DOI:10.1038/s41598-017-05792-1 1.

Ibe, A.C. (1986). Harbour Development Related Erosion at Victoria Island. In Intern. Geomorphology 1986 Part 1. Edited by V. Gardinier, John Wiley Ltd, Chichester, 165-181.

Ibe, A.C. (1988). Coastline Erosion in Nigeria. Ibadan University Press, Ibadan, Nigeria. 217p.

Ibe, A.C. and E.E. Antia (1983). Preliminary assessment of the impact of erosion along the Nigerian shoreline. NIOMR Technical Paper No. 13. 17p.

Ibe, A.C., L.F. Awosika, C.E. Ibe and L.E. Inegbedion (1991). Monitoring of the 1985/86 Beach Nourishment Project at Bar Beach, Victoria Island, Lagos, Nigeria, Coastal Zone, 91 (II), 534-552.

IPCC (1992). Global Climate Change and the Rising Challenge of the Sea, Report of the Intergovernmental Panel on Climate Change, Response Strategies Working Group, Coastal Management Subgroup, p. 19.

Meehl, G.A., T.F. Stocker, W.D. Collins, P. Friedlingstein, A.T. Gaye, J.M. Gregory, A. Kitoh, R. Knutti, J.M. Murphy, A. Noda, S.C. B. Raper, I.G. Watterson, A.J. Weaver and Z.C. Zhao (2007). Global Climate Projections. In: Climate Change 2007: The Physical Science Basis. Contribution of Working Group I to the Fourth Assessment Report of the Intergovernmental Panel on Climate Change [Solomon, S., D. Qin, M. Manning, Z. Chen, M. Marquis, K.B. Averyt, M. Tignor and H.L. Miller (eds.)]. Cambridge University Press, Cambridge, United Kingdom and New York, NY, USA.

Nwilo, P.C. (2016). Minimising the Vulnerabilities of Coastal Cities (Lagos, Cape Town and Cairo) and Communities in Africa through Adaptation to Climate Change Impacts. Presentation.

Nwilo, P.C. (1995). Sea Level Variations and the impacts along the Nigerian Coastal areas. Ph.D Thesis, Environmental Resources Unit, University of Salford, Salford, UK.

Nwilo, P.C. and A. Onuoha (1993). Environmental impacts of human activities on the coastal areas of Nigeria. In: Coastlines of Western Africa (ed. by L. F. Awosika & O. Magoon). American Society of Engineers.

Obiefuna, J.N., P.C. Nwilo, A.O. Atagbaza and C.J. Okolie (2013). Land cover dynamics associated with the spatial changes in the wetlands of Lagos/Lekki Lagoon system of Lagos, Nigeria, Journal of Coastal Research, 29(3), 671–679.

Obiefuna, J.N. (2015). Environmental challenges facing urban development on Lekki Peninsula barrier island, Lagos, Nigeria. An Unpublished PhD dissertation, University of Lagos, Akoka, Lagos, December, 2015. 247p.

Obiefuna, J.N., A. Omojola, O. Adeaga and N. Uduma-Olugu (2017). Groins or Not: Some environmental challenges to urban development on a Lagos coastal barrier island of Lekki Peninsula. Journal of Construction Business and Management, 1(1), 14-28.

Orupabo, S. (1990). Observation on Beach Stability: A case study on the Victoria Island Beach. PhD Thesis Department of Surveying, University of Lagos, Nigeria.

Pidwirny, M. (2006). Fundamentals of Physical Geography. Chapter 10: Introduction to the Lithosphere: Erosion and deposition. University of British Columbia, Okanagan.

Smith, A.M., A.A. Mather, S.C. Bundy, J.A.G. Cooper, L.A. Guastella, P.J. Ramsay and A. Theron (2010). Contrasting styles of swell-driven coastal erosion: examples from KwaZulu-Natal, South Africa. Geol. Mag., 1-14. DOI:10.1017/S0016756810000361

van Bentum, K.M. (2012). The Lagos Coast: Investigation of the long-term morphological impact of the Eko Atlantic City project. M.Sc. Thesis, Delft University of Technology.

van Rijn, L.C. (2011). Coastal erosion and control. Ocean and Coastal Management, 54(12), 867–887. https://doi.org/10.1016/j.ocecoaman.2011.05.004

Watson, D., and M. Adams (2011). Design for Flooding: Architecture, Landscape, and Urban Design for Resilience to Flooding and Climate Change. New Jersey: John Wiley & Sons, Inc.

Williams, W.W (1960). Coastal Changes. Greenwood press, Westport, Connecticut, 220.

WIOMSA (2010). Shoreline Change in Tanzania and Kenya: Assessment Procedures and Mitigation Strategies for Management. WIOMSA Manuals No. 00 Zanzibar.

Zhang, K., B.C. Douglas and S.P. Leatherman (2004). Global warming and Coastal Erosion. Climatic Change, 64, 41–58.

Zollini, S., M. Alicandro, M. Cuevas-González, V. Baiocchi, D. Dominici and P.M. Buscema (2019). Shoreline Extraction Based on an Active Connection Matrix (ACM) Image Enhancement Strategy. Journal of Marine Science and Engineering, 8(1), 9. doi:10.3390/jmse801000

INDIAN SOCIETY OF GEOMATICS: AWARDS

National Geomatics Award for Excellence

This award has been instituted to recognize outstanding and conspicuously important contribution in promoting geomatics technology and applications at the country level. The contributions should have made major impact on the use of this technology for national development.
Areas of contribution considered for the award are:

1. Geographical Information System
2. Global Positioning System
3. Photogrammetry
4. Digital Cartography
5. Applications of Geomatics

The award shall consist of Rs. 50,000/- in cash, a medal and citation.

Eligibility

Any citizen of India, engaged in activities related to geomatics technology and its applications is eligible for this award. The prize is awarded on the basis of work primarily done in India.

The age limit for awardees is 45 years or above as on June 30 of the year of award.

Selection

A duly constituted Award Committee will evaluate all nominations received. The committee shall consist of eminent experts in the field of geo-spatial technology, to be identified by the Executive Council, ISG. The committee shall forward selected name/s to ISG – EC for approval and announcement. Apart from those persons, whose nominations have been received, the Committee may consider any person or persons who, in their opinion, have made outstanding contributions to development of geo-spatial technology and applications.

The award can be withheld in any year if, in the opinion of the committee, no candidate is found suitable in that particular year.

Presentation of the Award

The award shall be presented during the Annual Convention of ISG. Local Hospitality shall be taken care by ISG & Air fare (low cost) may be reimbursed if awardees request for it.

How to make Nomination

The nominations can be proposed by Head of a major research institute/ centre; Vice-Chancellor of a university; Secretary of Government Scientific Departments; President of a National Academy, President, Indian Society of Geomatics / Indian Society of Remote Sensing / Indian National Cartographic Association / ISG fellow or two life members of the society with more than 10 year old membership.

A candidate once nominated would be considered for a total period of two years. Nomination should be sent in the prescribed format to Secretary, ISG.

The last date for receiving nominations shall be September 30 or otherwise extended.

Journal of Geomatics Vol 14, No. 1, April 2020

Format for nomination of Geomatics Award for Excellence

1. Name of the Nominee
2. Postal Address
3. Academic Background (Bachelor degree onwards)
4. Field of Specialisation
5. Important positions held (in chronological order)
6. Professional Experience including foreign assignments.
7. Important Awards / Honours
8. Important Publications/Patents: (A set of ten most important publications to be enclosed with this form)
9. Contributions of Nominee based on which the nomination is sent (in 1000 words, also provide a statement in 50 words which may be used for citation.):
10. Other Relevant Information:

Proposer:

Signature
Name
Address
Phone/ Fax
E-mail
Life Membership No. (in case of ISG Member):

Place & Date

Endorsed by (in case nomination is by 2 ISG Life members)

Signature
Name
Address
Phone/ Fax
E-mail
Life Membership No. (in case of ISG Member):

Place & Date
(The proposer should give a brief citation of the nominee's work)

National Geomatics Award

National Geomatics Award to be given each year: a) for original and significant contribution in Geomatics technology, b) for innovative applications in the field of Geomatics. Each award comprises a medal, a citation and a sum of Rs 25,000/- The guidelines for these awards are available on ISG website.

ISG Chapter Award for Best Performance

The best chapter award will be given to an active chapter of Indian Society of Geomatics, which has made significant contribution to further the mandate and goal of the society. The award consists of a citation and medal

President's Appreciation Medal for Contribution to the ISG

This award will be given to a member of the society, who has made noteworthy contribution to the growth of the ISG (its main body or any chapter). The Award consists of a Medal and a Citation.

Prof. Kakani Nageswara Rao Endowment Young Achiever Award

Indian Society of Geomatics instituted a new award from year 2013 named "Prof. Kakani Nageswara Rao Endowment Young Achiever Award", to encourage young researchers/scientists/academicians pursuing research in the field of geospatial technology/applications. The award carries a cash prize of Rs. 10,000/- along with a citation.

NATIONAL GEOMATICS AWARD

Indian Society of Geomatics has instituted two National Geomatics Awards to be given each year for (a) Original and significant contribution in Geomatics technology, (b) Innovative application(s) in the field of Geomatics. Each award comprises a medal, a citation and a sum of Rs. 25,000/-.

The guidelines for the award are as under

Areas of contribution considered for the award (both technology and applications)

1. Geographical Information System
2. Global Positioning System
3. Photogrammetry
4. Digital Cartography
5. Remote Sensing

Eligibility

Any citizen of India engaged in scientific work in any of the above-mentioned areas of research is eligible for the award.

The awards are to be given for the work largely carried out in India.

- First award will be given for original contribution in the field of Geomatics technology supported by publications in a refereed journal of repute.
- Second award will be given for carrying out innovative application(s). Supported by publications in rear reviewed Journals of repute.
- The contribution for the first award should have been accepted by peers through citation of the work.
- Work based on the applications of existing technologies will not be considered for the first award.
- The work should have made impact on the overall development of Geomatics.

How to Send Nomination

Nominations should be sent in the prescribed format, completed in all aspects to the Secretary, Indian Society of Geomatics, Space Applications Centre Campus, Ahmedabad 380 015 by August 31 of the year of award.

Selection Process

An expert committee, consisting of at least three members, constituted by the Executive Council of the Indian Society of Geomatics, will scrutinize the nominations and recommend the awardees' names to the Executive Council. The Council will decide on the award based on the recommendations.

FORMAT FOR AWARD NOMINATION

1. Name of the Candidate:
2. Present Position:
3. Positions held earlier (chronological order):
4. Academic qualifications (Bachelor's degree onwards):
5. Names of at least three Indian Scientists/Technologist in the area as possible referees *:
6. Brief write up on the work (500 words) for which award is claimed:
7. Publication(s) on the above work (reprint(s) to be enclosed):
8. List of other publications of the candidate:
9. Citation of the work for which award is claimed:
10. Impact of the work (for which award is claimed) on the development in the field of Geomatics (500 words):
11. Whether the work has already won any award? If so, give details:

The Applications in the above format (five copies) should be submitted (by Registered Post or Speed Post) to

The Secretary, Indian Society of Geomatics,
Space Applications Centre Campus,
Ahmedabad-380015

so as to reach by September 30 of the year of award

*ISG is, however, not bound to accept these names and can refer the nomination to other experts/peers

INDIAN SOCIETY OF GEOMATICS: FELLOWS

Shri Pramod P. Kale, Pune
Dr George Joseph, Ahmedabad
Dr A.K.S. Gopalan, Hyderabad
Dr Prithvish Nag, Varanasi
Dr Baldev Sahai, Ahmedabad
Shri A.R. Dasgupta, Ahmedabad
Dr R.R. Navalgund, Bengaluru
Shri Rajesh Mathur, New Delhi
Dr Ajai, Ahmedabad
Prof P. Venkatachalam, Mumbai
Dr Shailesh Nayak
Prof I.V. Murli Krishna
Prof SM Ramasamy, Tiruchirapalli
Dr Ashok Kaushal, Pune
Shri A.S. Kiran Kumar, Bengaluru
Prof. P.K. Verma, Bhopal
Maj. Gen. Siva Kumar, Hyderabad

INDIAN SOCIETY OF GEOMATICS: PATRON MEMBERS

P-1 Director, Space Applications Centre (ISRO), Jodhpur Tekra Satellite Road, Ahmedabad - 380 015
P-2 Settlement Commissioner, The Settlement Commissioner & Director of Land Records-Gujarat, Block No. 13, Floor 2, Old Sachivalay, Sector-10, Gandhinagar – 382 010
P-3 Commissioner, Mumbai Metropolitan Region Development Authority, Bandra-Kurla Complex, Bandra East, Mumbai - 400 051
P-4 Commissioner, land Records & Settlements Office, MP, Gwalior - 474 007
P-5 Director General, Centre for Development of Advanced Computing (C-DAC), Pune University Campus, Ganesh Khind, Pune - 411 007
P-6 Chairman, Indian Space Research Organization (ISRO), ISRO H.Q., Antariksha Bhavan, New BEL Road,Bengaluru 560 231
P-7 Director General, Forest Survey of India, Kaulagarh Road, P.O. I.P.E., Dehra Dun – 248 195
P-8 Commissioner, Vadodara Municipal Corporation, M.S. University, Vadodara - 390 002
P-9 Director, Centre for Environmental Planning and Technology (CEPT), Navarangpura, Ahmedabad - 380 009
P-10 Managing Director, ESRI INDIA, NIIT GIS Ltd., 8, Balaji Estate, Sudarshan Munjal Marg, Kalkaji, New Delhi - 110 019
P-11 Director, Gujarat Water Supply and Sewerage Board (GWSSB), Jalseva Bhavan, Sector – 10A, Gandhinagar - 382 010
P-12 Director, National Atlas & Thematic Mapping Organization (NATMO), Salt Lake, Kolkata - 700 064
P-13 Director of Operations, GIS Services, Genesys International Corporation Ltd., 73-A, SDF-III, SEEPZ, Andheri (E), Mumbai - 400 096
P-14 Managing Director, Speck Systems Limited, B-49, Electronics Complex, Kushiaguda, Hyderabad - 500 062
P-15 Director, Institute of Remote Sensing (IRS), Anna University, Sardar Patel Road, Chennai - 600 025
P-16 Managing Director, Tri-Geo Image Systems Ltd., 813 Nagarjuna Hills, PunjaGutta, Hyderabad - 500 082
P-17 Managing Director, Scanpoint Graphics Ltd., B/h Town Hall, Ashram Road, Ahmedabad - 380 006
P-18 Secretary General, Institute for Sustainable Development Research Studies (ISDRS), 7, Manav Ashram Colony, Goplapura Mod, Tonk Road, Jaipur - 302 018
P-19 Commandant, Defense institute for GeoSpatial Information & Training (DIGIT), Nr. Army HQs Camp, Rao Tula Ram Marg, Cantt., New Delhi - 110 010
P-20 Vice President, New Rolta India Ltd., Rolta Bhavan, 22nd Street, MIDC-Marol, Andheri East, Mumbai - 400 093
P-21 Director, National Remote Sensing Centre (NRSC), Deptt. of Space, Govt. of India, Balanagar, Hyderabad - 500 037
P-22 Managing Director, ERDAS India Ltd., Plot No. 7, Type-I, IE Kukatpalli, Hyderabad - 500 072
P-23 Senior Manager, Larsen & Toubro Limited, Library and Documentation Centre ECC Constr. Gp., P.B. No. 979, Mount Poonamallee Road, Manapakkam, Chennai - 600 089.
P-24 Director, North Eastern Space Applications Centre (NE-SAC), Department of Space, Umiam, Meghalaya 793 103
P-25 Progamme Coordinator, GSDG, Centre for Development of Advanced Computing (C-DAC), Pune University Campus, Pune – 411 007
P-26 Chief Executive, Jishnu Ocean Technologies, PL-6A, Bldg. No. 6/15, Sector – 1, Khanda Colony, New Panvel (W), Navi Mumbai – 410 206
P-27 Director General, A.P. State Remote Sensing Applications Centre (APSRAC), 8th Floor, "B" Block, Swarnajayanthi Complex, Ameerpet, Hyderabad- 500 038
P-28 Director, Advanced Data Processing Res. Institute (ADRIN), 203, Akbar Road, Tarbund, Manovikas Nagar P.O., Secunderabad –500 009
P-29 Managing Director, LEICA Geosystems Geospatial Imaging Pvt. (I) Ltd., 3, Enkay Square, 448a Udyog Vihar, Phase-5, Gurgoan- 122 016
P-30 Director, Defense Terrain Research Limited (DTRL), Ministry of Defense, Govt. of India, Defense Research & Development Organisation, Metacafe House, New Delhi – 110 054
P-31 Chairman, OGC India Forum, E/701, Gokul Residency, Thakur Village, Kandivali (E), Mumbai – 400 101
P-32 Managing Director, ML Infomap Pvt. Ltd., 124-A, Katwaria Sarai, New Delhi – 110 016
P-33 Director, Rolta India Limited, Rolta Tower, "A", Rolta Technology Park, MIDC, Andheri (E), Mumbai – 400 093
P-34 Director, State Remote Sensing Applications Centre, Aizawl – 796 012, Mizoram

Journal of Geomatics Vol 14, No. 1, April 2020

Instructions for Authors

The journal covers all aspects of Geomatics – geodata acquisition, pre-processing, processing, analysis and publishing. Broadly this implies inclusion of areas like GIS, GPS, Photogrammetry, Cartography, Remote Sensing, Surveying, Spatial Data Infrastructure and Technology including hardware, software, algorithm, model and applications. It endeavors to provide an international forum for rapid publication of developments in the field – both in technology and applications.

A manuscript for publication must be based on original research work done by the author(s). It should not have been published in part or full in any type of publication nor should it be under consideration for publication in any periodical. Unsolicited review papers will not be published.

The Editorial Board or the Indian Society of Geomatics is not responsible for the opinions expressed by the authors.

Language

The language of the Journal will be English (Indian). However, manuscripts in English (US) and English (British) are also acceptable from authors from countries located outside India.

Manuscript Format

Each paper should have a title, name(s) of author(s), and affiliation of each of the authors with complete mailing address, e-mail address, an abstract, four to six keywords, and the text. The text should include introduction/background, research method, results, discussion, followed by acknowledgements and references. The main text should be divided in sections. Section headings should be concise and numbered in sequence, using a decimal system for subsections. Figures, images and their captions should be inserted at appropriate points of the text. Figures, images and tables should fit in two column format of the journal. If absolutely necessary, figures, images and tables can spread across the two columns. Figures and images, however, should not exceed half a page in height. A title should be provided for each Table, Image and Figure. All figures and images should be in 600 dpi resolution and sized as per column/margin width. Authors must ensure that diagrams/figures should not lose easy readability upon reduction to column size. The SI (metric) units and international quantities should be used throughout the paper. In case measurements are given in any other system, equivalent measurements in SI (metric) units should be indicated in brackets.

Use MS Word with English (UK/US) or English (Indian) dictionary. The page size should be A4 paper, with 2 cm margin on all sides. Title, authors and affiliation should be centred. Abstract should be justified across margins. The manuscript text should be in two columns of 8.2 cm each with a gutter of 6mm between them. Use only Times New Roman fonts. Title should be 12 points bold. Authors and affiliation should be 9 points. All other text including headings should be 10 points. Heading numbering scheme should be decimal e.g. 1, 1.1, 1.2.3, etc. Headings should be in bold.

Normally length of a published paper should be about 6-10 pages in A4 size including figures. Use of illustrations in colour should be restricted and resorted to only where it is absolutely necessary and not for enhancing the look of the paper. If the number of colour illustrations exceeds five, authors' institution may be asked to reimburse the extra cost involved, which at current rates is about Rs. 2500 per coloured figure/diagram/plate/illustration.

Submission of Manuscript

Submissions should be in electronic form via email. The manuscript may be sent by email to drajai1953@gmail.com. In exceptional cases hard copy submission in camera ready form may be allowed with the prior permission of the Chief Editor. Submission in any other form will be returned to the author. To speed up the review process, authors are advised to provide a list of three probable reviewers with their institutional address and e-mail IDs.

Guidelines for Citing References

Names of all cited publications should be given in full. No abbreviations should be used. Following procedure is to be adopted.

Journal Publications

Bahuguna, I.M. and A.V. Kulkarni (2005). Application of digital elevation model and orthoimages derived from IRS-1C Pan stereo data in monitoring variations in glacial dimensions, Journal of the Indian Society of Remote Sensing, 33(1), 107- 112. (to be referred to in the text as Bahuguna and Kulkarni (2005) or if more than two sets of authors are to be referred to, as (Bahuguna and Kulkarni, 2005; Jain et al., 1994)) When more than two authors are to be referred to, use Jain et al. (1994). However, in References, all authors are to be mentioned.

Publication in a Book

Misra, V.N. (1984). Climate, a factor in the rise and fall of the Indus Civilization – Evidence from Rajasthan and Beyond in Frontiers of the Indus Civilization (B.B. Lal and S.P. Gupta: Chief Editors) Books and Books, New Delhi, pp. 461-489

Papers Published in Seminar/ Symposium Proceedings

Jain, A., A.R. Shirish, M. Das, K. Das, M.C. Porwal, and P.S. Roy (1994). Remote Sensing and Geographic Information System – An approach for the assessment of biotic interference in the forest ecosystem. Proceedings. 15th Asian Conference on Remote Sensing, Bangalore, November 17-23, 1994, pp. 65-72.

Books

Possehl, Gregory L. (1999). Indus Age: The beginnings. Oxford and IBH Publishing Corporation, New Delhi.

Reviewing

Each paper will be reviewed by three peers. Papers forwarded by members of the Editorial or Advisory Boards along with their comments would get processed faster and may be reviewed by two referees only.

Sample format for Authors is available in downloadable form at ISG website: www.isgindia.org/JOG/Sample_format.doc

Copyright

The copyright of the paper selected for publication will rest with the Indian Society of Geomatics. Corresponding author shall be required to sign a copyright assignment form, on behalf of all authors, once the paper is selected for publication. Authors are, however, at liberty to use this material elsewhere after obtaining permission from the Indian Society of Geomatics.

If the authors have used any copyright material in their manuscript, it is understood that they have obtained permission from the owner of the copyright material and they should convey the same along with the manuscript to the Chief Editor.

Certificate of Original Work

The authors will also provide a certificate that the paper is an original work, not published or being considered for publication elsewhere.

In the event the certificate turns out to be false, the Journal shall ban the author(s) from publishing in the Journal for a period of five years and inform the same to all other related publications.

Reprints

Authors will be allowed to download the (PDF) of their paper from ISG Website www.isgindia.org, No hard copy reprints will be provided.

Journal of Geomatics

Advertisement Rates

	1 Issue	4 Issues
Back Cover Page in colour	**Rs. 25,000**	**Rs. 80,000**
Inside Cover Page in colour	**Rs. 20,000**	**Rs. 64,000**
Full Page inside in colour	**Rs. 15,000**	**Rs. 48,000**
Full Page inside in B/W	**Rs. 10,000**	**Rs. 32,000**

Advertisement Details

Mechanical Details
Double Spread/Center Spread (42 x 29.7) cm
Full page bleed (21 x 29.7) cm
Full page non-bleed (19 x 27.7) cm

Art Requirements

Negatives: Art must be right reading, emulsion, down. Film must be supplied in one piece per color, each identified by color. Camera-ready art is accepted for black & White adds; however, film is preferred. Electronic Files are also accepted.

Electronic File Requirements: All material must be received before ad close dates.

Software: Adobe illustrator 9.0 (saved as EPS). Adobe Photoshop CS (saved as EPS or TIFF). Please convert higher versions down. If you can only supply an IBM format, the file must be in viewable EPS or TIFF format with fonts embedded as that format.

Colour Ads: Colour separations must be provided, right reading, emulsion down. Please note that files using RGB or Pantone colours (PMS) must be converted to CMYK before we receive files.

To,
The Secretary, Indian Society of Geomatics
6202, Space Applications Centre (ISRO)
AHMEDABAD – 380 015. INDIA

Sir,

I want to become a Member/ Life Member/ Sustaining Member/ Patron Member/ Foreign Member/ Student Member of the Indian Society of Geomatics, Ahmedabad for the year _____. Membership fee of Rs. _____ /- is being sent to you by Cash/ DD/ Cheque. (In case of DD/ Cheque No._____dated_____drawn on Bank

_____ . **I agree to abide by the Constitution of the Society.**

Date:

Place: **Signature**

- Name: Mr/Ms/Mrs/Dr_____
- Address: _____

_____PIN: _____

Phone: _____ Fax: _____Email:

_____ • Date of Birth

_____

•Qualifications_____

- Specialisation: _____
- Designation: _____ Organisation. _____
- Membership in other Societies: _____
- Mailing Address: _____

_____PIN: _____

Proposed by:
(Member's Name and No)
Signature of Proposer

For Office Use: A/P/L Member No.		Receipt No.		Date:	

Indian Society of Geomatics (ISG), Room No. 6202 Space Applications Centre (ISRO), Ahmedabad-380015, Gujarat. Url: www.isgindia.org Phone: +91-79 26916202
Email: secretary@isgindia.org or sasharma@sac.isro.gov.in Fax +91-79-26916287

MEMBERSHIP FEES

Sr. No.	Membership Category	Life/Patron Membership fees ₹ Indian	Life/Patron Membership fees US $ Foreign	Annual Subscription ₹ Indian
1.	Annual Member	10	---	300
2.	Life Member a) Admitted below 45 years of age	2500	250	
	b) Admitted after 45 years of age	2000	200	
3.	Sustaining Member	---	---	2000
4.	Patron Member	50000	3000	---
5.	Student Member	10	---	100

MEMBERSHIP GUIDELINES

- Subscription for Life Membership is also accepted in two equal instalments payable within duration of three months, if so desired by the applicant. In such a case, please specify that payment will be in instalments and also the probable date for the second instalment (within three months of the first instalment).
- A Member of the Society should countersign application of membership as proposer.
- Subscription in DD or Cheque should be made out in the name of **'Indian Society of Geomatics'** and payable at Ahmedabad.
- Direct deposit in ISG A/Cs must include bank fee RS. 25/- for cash payment.
- Financial year of the Society is from April 1 to March 31.
- For further details, contact Secretary, Indian Society of Geomatics at the address given above.
- ISG has chapters already established at the following places. Ahmedabad, Ajmer, Bhagalpur, Bhopal, Chennai, Dehradun, Delhi, Hissar, Hyderabad, Jaipur, Ludhiana, Mangalore, Mumbai, Mysore, Pune, Shillong, Trichi, Srinagar, Vadodara, Vallabh Vidya Nagar, Visakhapatnam and Trivandrum. Applicants for membership have the option to contact Secretary/Chairman of the local chapter for enrolment. Details can be found at the website of the Society: www.isgindia.org.
- Journal of the Society will be sent to Life Members by softcopy only.

Indian Society of Geomatics (ISG), Room No. 6202 Space Applications Centre (ISRO), Ahmedabad-380015, Gujarat. Url: www.isgindia.org Phone: +91-79 26916202
Email: secretary@isgindia.org or sasharma@sac.isro.gov.in Fax +91-79-26916287